

Research & Development
2022

Mechanical Engineering Letters – 2022

Technical-Scientific Journal supported by the Institute of Technology,
Hungarian University of Agriculture and Life Science (MATE), Gödöllő,
published by GATE Nonprofit Ltd.

Editor-in-Chief:
Dr. István SZABÓ

Editor:
Dr. Gábor KALÁCSKA

Executive Editorial Board:

Dr. István BARÓTFI	Dr. László KÁTAI
Dr. János BEKE	Dr. Sándor MOLNÁR
Dr. István FARKAS	Dr. Péter SZENDRŐ
Dr. László FENYVESI	Dr. Zoltán VARGA
Dr. István HUSTI	

International Advisory Board:

Dr. Patrick DE BAETS (B)
Dr. Radu COTETIU (Ro)
Dr. Manuel GÁMEZ (Es)
Dr. Klaus GOTTSCHALK (D)
Dr. Yurii F. LACHUGA (Ru)
Dr. Elmar SCHLICH (D)
Dr. Nicolae UNGUREANU (Ro)

Cover design:
Dr. László ZSIDAI

HU ISSN 2060-3789

All Rights Reserved. No part of this publication may be reproduced, stored in a retrieval system or transmitted in any form or by any means, electronic, mechanical, photocopying, recording, scanning or otherwise without the written permission of GATE Nonprofit Ltd.

Páter K. u. 1., Gödöllő, H-2103 Hungary

Volume 22 (2022)

Contents

Aschenaki T. ALTAYE, Piroska VIG, Istvan FARKAS: Assessing of various cooling mechanisms at photovoltaic systems	4
Ahmed Elawad Eltayeb AHMED, György PILLINGER, Péter KISS: The influence of sandy loam soil moisture content on its load-bearing capacity	15
Szabolcs PÁGER, László FÖLDI, Gábor GÉCZI: Creation and validation of simplified mathematical model for residential building energy analysis in matlab environment	26
Sándor FENYVESI, Gyula Ferenc VASVÁRI, Róbert Zsolt KERESZTES, László ZSIDAI: 3D metalprinting by CMT technology	43
Ahssan M.A. Alshibil, Kornél BESSENYEI, István PATAY: Experimental investigation of proton exchange membrane fuel cells efficiency (PEM)	53
Dániel SZÖLLŐSI, Péter KISS: Soot accumulation in the diesel particulate filter and its effect on the filtration efficiency	61
Ahmad Dughmi, László KÁTAI: Investigate the effects of the generative design method on the multirotor structure	70
Gergő BAGI, János TÓTH: Design and implementation of an object sorting robotic arm	81
János TÓTH: Implementation of an educational PID controller	92
László BENSE, Attila LÁGYMÁNYOSI, István NAGY, István OLDAL, István SZABÓ: Variation of drone rotor operating parameters as a function of pitch angle	100
Norbert BÍRÓ, Péter KISS: Comparing pressure hysteresis of DPF filters	109
Nuha Desi ANGGRAENI, István SERES, István FARKAS: Approaches to the performance evaluation of semi-transparent photovoltaic modules	116

Assessing of various cooling mechanisms at photovoltaic systems

Aschenaki T. ALTAYE¹, Piroska VIG²,
Istvan FARKAS³

¹Doctoral School of Mechanical Engineering,

²Institute of Mathematics and Basic Science,

³Institute of Technology,

Hungarian University of Agriculture and Life Sciences,

Pater K.u.1., Gödöllő, H-2100, Hungary

Abstract

Due to numerous activities, energy is rising swiftly, and a nation's economic growth is influenced by its energy sources. In this study, various cooling mechanisms of photovoltaic systems were reviewed, climatic variables were simulated, and its consequences were discussed. According to a review of the literature, the best cooling mechanisms are recognized as steady state water flow, aluminum fins, and phase change materials. The results of the simulation demonstrated that solar radiation, ambient temperature, and photovoltaic cell temperatures have most important impact on the performance ratio, or the amount of energy generated for the grid. Based on the one-year simulation, 895.74 kWh of energy were produced, and average yearly performance ratio was 80.7% for the selected system and location.

Keywords

photovoltaic system, cooling mechanisms, climatic variables, assessing, simulation.

Introduction

In the world, the need for energy is increased quickly due to various activities. Economic development of any country is driven by its sources of energy. However, with the increased attention being paid to how conventional energy use affects greenhouse gas emissions and other environmental problems. As a result, renewable energy technologies like photovoltaic system are increasingly being advocated for use in the production of electricity. Because PV system provides benefits like being eco-friendly, having little maintenance costs, and having ample and free energy (Yadav, 2015). The PV system converts solar energy into DC power but loads used are mostly AC, therefore, the PV system requires inverter to convert DC into AC and hence, a grid-connected PV system is recommended to be installed in Addis Ababa, Ethiopia.

Ethiopia is a developing nation that has abundant access to renewable energy sources. Hydropower energy is the main source of power for the nation. Even though the nation is endowed with renewable energy, its residents still struggle to obtain enough electricity. As a result, using photovoltaic for grid-connected systems may contribute to solve the energy crisis. Location of the study area is latitude 9.0° N and longitude 38.7° E in Addis Ababa. On average, it has an average temperature close to 15°C . In this setting, any project utilizing photovoltaic power plants can prosper. Therefore, it is the good place to install the PV power plant.

2. Implemented methodologies

The review of cooling methods of photovoltaic system

Below, many photovoltaic cooling techniques were described. Since the efficiency of the photovoltaic system depends on the cell temperature, lowering the cell temperature is an important duty in the system since it ensures system performance.

Despite the development of numerous additional cell types, the original generation of crystalline silicon cells remain the most widely used around the world due to their reliability in terms of long-term efficiency and yields. The significant reliance of the electric efficiency on the operating temperature, which rapidly decreases with intense solar radiation, is a significant negative. In order to improve electrical efficiency, reduce solar cell deterioration, and lengthen the lifespan of these useful solar systems, photovoltaic panel cooling is essential (Hadipour et al., 2021).

Amelia et al. (2016) researched a forced air convection cooling mechanism with the primary goal of examining the performance output of the PV panel with the presence of various numbers of DC fans as a cooling mechanism. They discovered that when the number of DC fans increased, the temperature of the PV panels decreased. However, adding more DC fans will cause a PV panel to use more energy. Therefore, there must be an optimal number of DC fans needed for a given PV panel.

On the other hand, Agyekum et al. (2021) looked at the cooling methods by combining active and passive cooling to increase a PV module's electrical output. The panel was cooled using a heat sink constructed of aluminum fins and an ultrasonic humidifier, as illustrated in Fig. 1. The efficiency of solar system was increased by creating a humid atmosphere at the back of the PV module using an ultrasonic humidifier.

For the purpose of increasing output power, a comparative examination of four different cooling techniques a water sprinkling system, a passive heat sink method, an active air fan method and a closed loop approach was carried out by Khan et al. (2017). Even though both technologies require constant electric power for operation, the active air-cooled fan system and closed loop system are comparatively more efficient than the heat sink-based passive cooling.

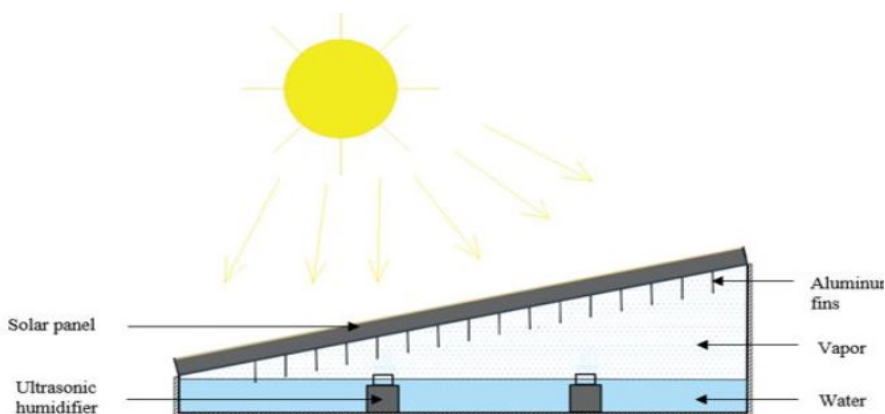


Figure 1. Schematic diagram of the PV-cooling system using ultrasonic humidifier and aluminum fins

Similarly, Bevilacqua et al. (2020) evaluated the long-term performances of three distinct cooling technologies working on the back surface of solar modules. In this study spray cooling and forced ventilation were investigated. From the analysis of the system efficiency, which included the spray cooling system's ability to ensure conversion efficiency better than the panel nominal number, further supported the findings.

Another similar research was done by Hadipour et al. (2021) on a pulsed-spray water cooling system for photovoltaic panels in order to increase the effectiveness of these solar systems and reduce water usage while cooling those. However, continuous flow water cooling rather than a pulsed spray water cooling system was able to achieve the PV panel's maximal electrical power output. Nevertheless, since the objective of the study was to use less water for cooling, the pulsed-spray water cooling mechanism is superior in this aspect.

In order to improve overall performance of the photovoltaic system, a fin-based passive cooling system has been developed, and fin-integrated photovoltaic modules have undergone a comprehensive evaluation. The study's findings examined by Raina et al. (2022) suggest that a passive cooling system like this one is quite successful at reducing the long-term effects of high module temperature on its performance and reliability, although a design like fin-based passive cooling system might not be practical in colder climates.

Nasef et al. (2019) examined different cooling mechanisms. Under this study steady water flow cooling, aluminum fin cooling and phase change material cooling systems were investigated.

Steady water flow cooling mechanism: this cooling method uses a constant water flow, which uses more water to cool the solar system. Despite requiring a lot of water, it is more effective in two reasons. The first is to reduce the temperature of the solar cell, as other mechanisms also do. The second and most crucial factor is that the system produce hot water too, for use at home or in other locations.

Aluminum fin cooling mechanism: fins are heat exchangers that transmit the heat produced by solar cells to the heat storage, PCM. Higher PV performance is the outcome, and it is a good cooling technique.

Phase change material cooling mechanism: PCMs offer a good potential for PV cooling in addition to storing energy from the fins and water flowing through the photovoltaic system. Only locations with consistent high levels of annual solar irradiance and minimal inter-seasonal climate variability will find PCM-based photovoltaic systems to be economically viable. Fig. 2 shows the direct and indirect PCM usage method for a solar module.

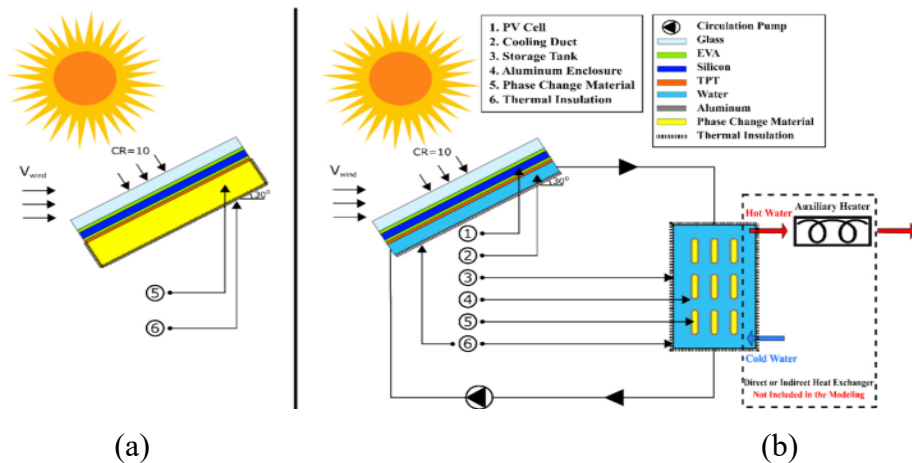


Figure 2. Schematic diagram for a) direct contact PCM b) indirect PCM water loop integrated system

After analysis of the worked literatures in this study, combined steady water flow, aluminum fins and phase change material (PCM) has the higher improvement of photovoltaic panel efficiency.

2.2. Simulation of grid connected photovoltaic system using PVsyst software

This clarifies how factors like solar input might impact a photovoltaic system's performance. Utilizing metrological data from Addis Ababa Ethiopia, the software generates solar data. Based on the available metrological data, the efficiency and performance of photovoltaic systems was evaluated. Finally, analysis of input and output factors, including temperature, solar irradiance, voltage and current, was done. The simulation and results were then reported using the PVsyst software for the chosen type of solar system. On the basis of the findings, a discussion and conclusion will be held.

PVsyst is a tool for designing and simulating solar systems. It was designed by researchers, engineers, and architects for usage. It provides a user-friendly method for project development (Soualmia and Chenni, 2017). This simulation was

examined under the following conditions: 2 modules were used, 3 m² module area was utilized and one inverter was used, type of module was 290 Wp 27V Si-mono CS6K-290MB-FB made in 2018, Canada. Fig. 3 shows the operation diagram of a grid-connected PV system.

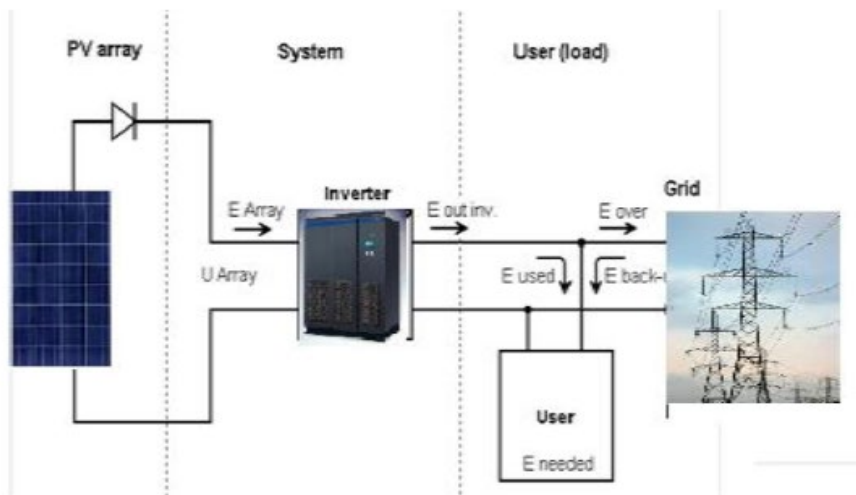


Figure 3. Schematic diagram of the grid connected photovoltaic system

3. Results and discussion

Table 1. and Fig. 4. demonstrate some of the solar data that are the key inputs for a professional energy yield assessment at a specific location. At the chosen areas, analysis based on weather records, including ambient temperature, wind velocity and solar radiation, was completed.

Table 1. Monthly meteorological values

	Jan.	Feb.	Mar.	Apr.	May	June	July	Aug.	Sep.	Oct.	Nov.	Dec.	Year	Unit
Hor. global	5.57	5.66	5.81	5.44	5.24	4.81	3.97	3.95	4.69	5.68	6.09	5.67	5.21	kWh/m ² .day
Hor. diffuse	1.84	1.96	2.37	2.54	2.37	2.72	2.59	2.68	2.61	1.90	1.74	1.51	2.24	kWh/m ² .day
Extra terrest.	9.03	9.73	10.29	10.51	10.36	10.19	10.22	10.38	10.33	9.89	9.20	8.87	9.91	kWh/m ² .day
Clearness Index	0.617	0.581	0.565	0.518	0.505	0.473	0.389	0.381	0.454	0.574	0.662	0.646	0.526	
Ambient tempr.	16.2	17.2	17.9	17.6	17.5	18.5	17.1	15.6	16.1	16.0	16.8	15.5	15.7	°C
Wind velocity	2.4	2.4	2.5	2.4	2.3	2.3	2.3	2.2	2.0	2.0	2.1	2.3	2.3	m/s

Fig. 5 illustrates how the current and voltage change at according to the solar radiation at 25 °C cell temperature. It is evident from the results that voltage and

current increase as sun radiation does. The maximum power, which is 250 W, is created at 25 °C and 1000 W/m². So can get the conclusion that solar radiation is the primary factor influencing how photovoltaic systems generate electric power. The relationship between the power and voltage was depicted in Fig. 6.

Solar paths at Bole.ST, (Lat. 9.0100° N, long. 38.3600° E, alt. 2354 m) - Legal Time

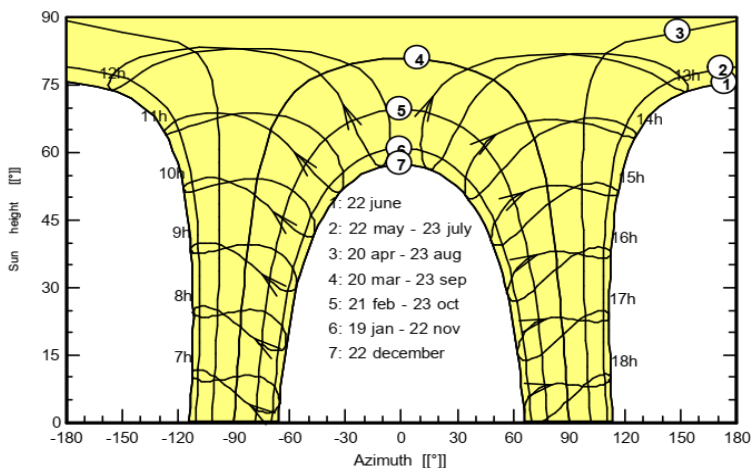


Figure 4. Solar horizon

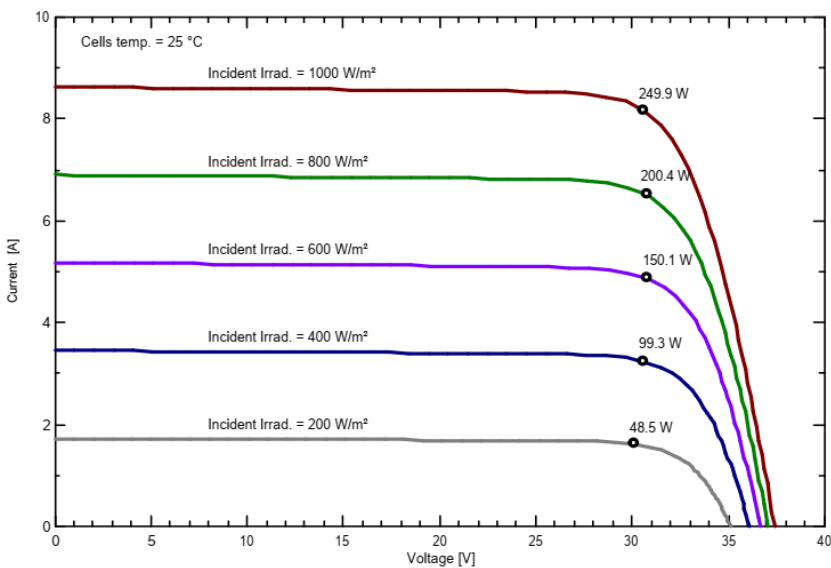


Figure 5. The characteristics of irradiation effect on voltage and current

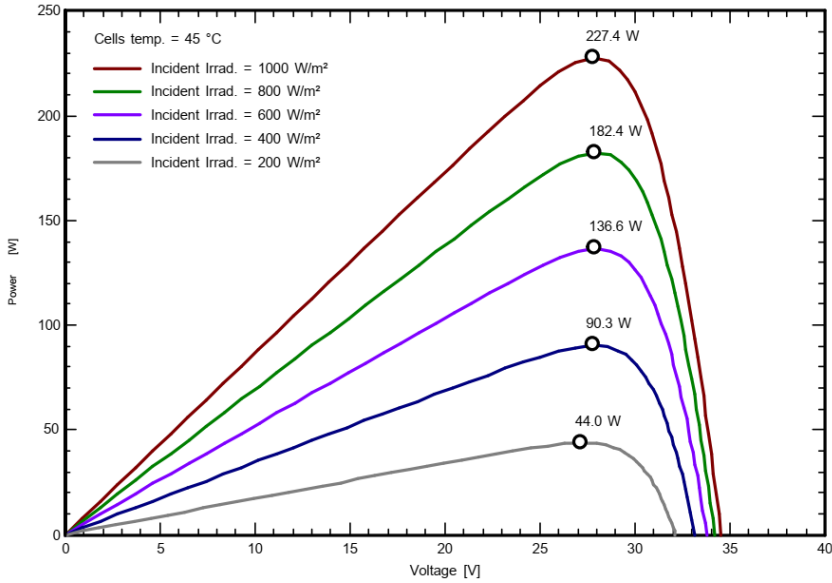


Figure 6. The characteristics of irradiation effect on power and voltage

The findings clearly show that voltage and power rise in conjunction with solar radiation. At 45 °C and 1000 W/m^2 , the maximum power of 227 W is generated. However, because the cell temperature is higher in this case than shown in Fig. 5, there is less power generation. These shows, as cell temperature increases, the power production and efficiency of a photovoltaic system decreases.

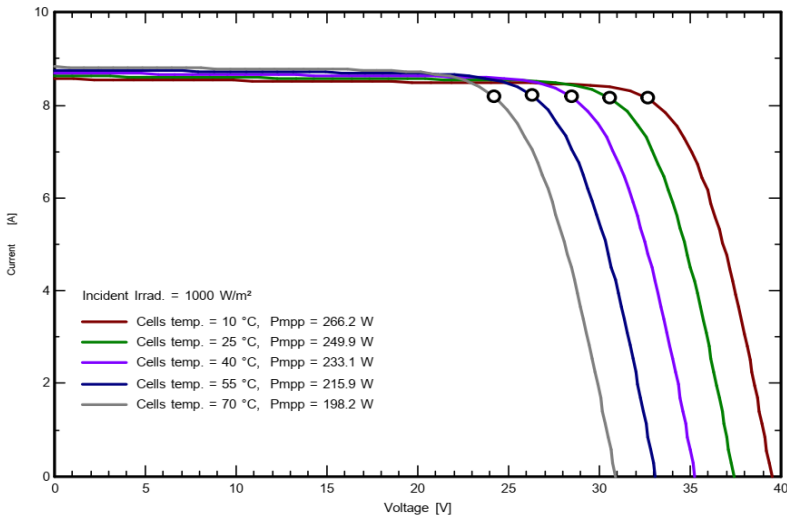


Figure 7. The cell temperature effect on current-voltage function

The change of current and voltage caused by changing cell temperature was also shown in Fig. 7. As shown here, the power in the maximum power point (MPP) decreases as cell temperature increases. As a result, cells are operating at lower temperatures while producing more electricity. To acquire the design power, multiple cooling mechanisms for solar systems must be taken into account.

Normalized productions such as collection losses, system losses and produced useful energy per installed kWp/day were evaluated from the simulation and the power production in Ethiopian summer season (July, June and August) was less as seen in Fig. 8a. These normalized productions are defined by the IEC norms (Kumar et al., 2017) and are standardized variables for assessing the PV system performance. Whereas the performance ratio is 80.7% in which the system is working at good condition (Fig. 8b).

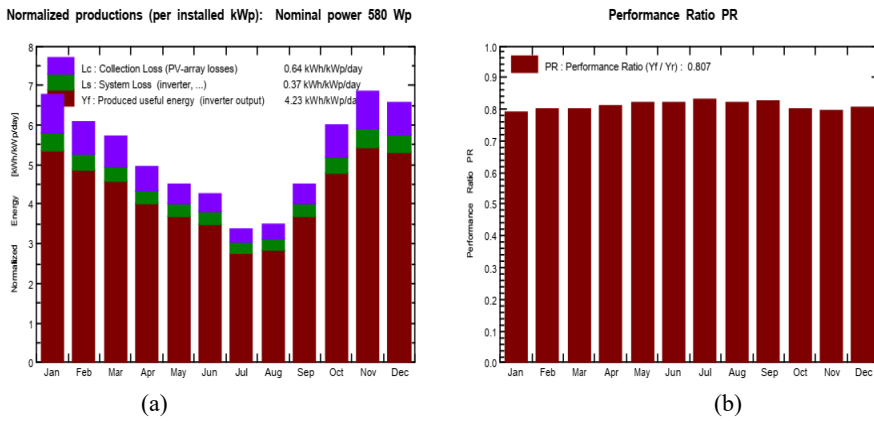


Figure 8. (a) Normalized energy production per installed kWp (b) Performance Ratio (PR)

Table 2. Balance sheet and main result of simulation

	GlobHor	DiffHor	T_Amb	GlobInc	GlobEff	EArray	E_Grid	PR
	kWh/m ²	kWh/m ²	°C	kWh/m ²	kWh/m ²	kWh	kWh	
January	180.6	58.90	16.70	209.6	206.1	104.4	96.31	0.792
February	156.7	61.60	17.10	169.9	166.8	85.5	78.81	0.800
March	176.7	67.30	17.70	177.7	174.1	89.3	82.26	0.798
April	157.4	78.80	17.60	148.2	144.6	75.8	69.75	0.812
May	156.4	70.70	18.40	139.1	135.3	72.0	66.27	0.821
June	147.1	69.60	17.00	127.7	123.9	66.2	60.68	0.819
July	115.6	72.10	15.50	104.0	101.1	54.9	50.00	0.829
August	116.1	76.00	16.10	107.9	105.1	56.5	51.40	0.821
September	137.1	75.70	15.80	134.6	131.3	70.0	64.33	0.824
October	175.3	70.60	16.70	185.8	182.3	93.5	86.08	0.799
November	179.8	53.50	15.50	205.5	202.5	102.7	94.58	0.793
December	171.8	53.80	15.09	204.0	200.7	103.2	95.27	0.805
Year	1870.6	808.60	16.60	1913.9	1873.9	974.0	895.74	0.807

Legends: GlobHor Horizontal global irradiation
 DiffHor Horizontal diffuse irradiation
 T_Amb Ambient Temperature
 GlobInc Global incident in coll. plane
 GlobEff Effective Global, corr. for IAM and shadings
 EArray Effective energy at the output of the array
 E_Grid Energy injected into grid
 PR Performance Ratio

The simulation results including the main data concerning to the photovoltaic system are summarized in the Table 2.

Based on the study site, there is a significant concentration of solar radiation from the middle of October until the end of the spring season. As a consequence, 895.74 kWh of energy was produced in the year along with the performance ratio of 80.7%. Solar radiation, the ambient temperature, and the effective energy at the array's output are all additionally simulated for the location.

Finally, in addition to optimization variable like climatic condition, applying the aforementioned mechanism (steady water flow cooling mechanism, phase change material cooling mechanism, aluminium fin cooling mechanism) for cooling photovoltaic systems will provide more electrical energy, lengthen the life of the system and produce thermal energy.

Conclusions

The following conclusions can be derived from the discussion of cooling mechanisms and the climate simulation presented above:

- From literature reviewed steady water flow cooling mechanism, phase change material cooling mechanism and aluminum fin cooling mechanisms are recommended as the best to optimize the performance PV-system by minimizing cell temperature.
- From simulation analysis it was seen that 896 kWh of energy was created a year and the performance ratio was 80.7%.
- Simulation findings clearly show that voltage and power rise in conjunction with solar radiation but inversely proportional to cell temperatures.
- Normalized productions such as collection losses, system losses and produced useful energy per installed kWp/day were evaluated from the simulation.
- From the simulation's loss diagram, it was determined that the horizontal global irradiation for the entire year was 1871 kWh/m², the effective irradiation on collectors was 1874 kWh/m², 3 m² collector, the PV conversion efficiency at STC was 17.67%, the nominal energy of the array (at STC efficiency) was 1089 kWh, the energy that was available at inverter output, and the energy that was injected into the grid was 896 kWh.
- The results of the simulation are consistent with the data in the literature, supporting the performance-enhancing effect of cooling the solar cell. In practice, the PV/T collector is a reasonable example of this method.

Acknowledgements

This work was supported by the Stipendium Hungaricum Programme and by the Mechanical Engineering Doctoral School, Hungarian University of Agriculture and Life Sciences, Gödöllő, Hungary.

References

- [1] Agyekum, E.B., Praveenkumar, S., Alwan, N.T., Velkin, V.I., Shcheklein, S.E., Yaqoob, S.J., 2021. Experimental investigation of the effect of a combination of active and passive cooling mechanism on the thermal characteristics and efficiency of solar PV module. *Inventions* 6. <https://doi.org/10.3390/inventions6040063>
- [2] Amelia, A.R., Irwan, Y.M., Irwanto, M., Leow, W.Z., Gomesh, N., Safwati, I., Anuar, M.A.M., 2016. Cooling on Photovoltaic Panel Using Forced Air Convection Induced by DC Fan. *Int. J. Electr. Comput. Eng. IJECE* 6, 526. <https://doi.org/10.11591/ijece.v6i2.9118>.
- [3] Bevilacqua, P., Bruno, R., Arcuri, N., 2020. Comparing the performances of different cooling strategies to increase photovoltaic electric performance in different meteorological conditions. *Energy* 195. <https://doi.org/10.1016/j.energy.2020.116950>.
- [4] Hadipour, A., Rajabi Zargarabadi, M., Rashidi, S., 2021. An efficient pulsed-spray water cooling system for photovoltaic panels: Experimental study and cost analysis. *Renew. Energy* 164, 867–875. <https://doi.org/10.1016/j.renene.2020.09.021>.
- [5] Khan, M.A., Ko, B., Nyari, E.A., Park, S.E., Kim, H.J., 2017. Performance evaluation of photovoltaic solar system with different cooling methods and a Bi-reflector PV system (BRPVS): An experimental study and comparative analysis. *Energies* 10. <https://doi.org/10.3390/en10060826>.
- [6] Kumar, N.M., Kumar, M.R., Rejoice, P.R., Mathew, M., 2017. Performance analysis of 100 kWp grid connected Si-poly photovoltaic system using PVsyst simulation tool, in: *Energy Procedia*. Elsevier Ltd, pp. 180–189. <https://doi.org/10.1016/j.egypro.2017.05.121>
- [7] Nasef, H.A., Nada, S.A., Hassan, H., 2019. Integrative passive and active cooling system using PCM and nanofluid for thermal regulation of concentrated photovoltaic solar cells. *Energy Convers. Manag.* 199. <https://doi.org/10.1016/j.enconman.2019.112065>.
- [8] Raina, G., Sinha, S., Saini, G., Sharma, S., Malik, P., Thakur, N.S., 2022. Assessment of photovoltaic power generation using fin augmented passive cooling technique for different climates. *Sustain. Energy Technol. Assess.* 52. <https://doi.org/10.1016/j.seta.2022.102095>.
- [9] Soualmia, A., Chenni, R., 2017. Modeling and simulation of 15 MW grid-connected photovoltaic system using PVsyst software, in: *Proceedings of 2016 International Renewable and Sustainable Energy Conference, IRSEC 2016*. Institute of Electrical and Electronics Engineers Inc., pp. 702–705. <https://doi.org/10.1109/IRSEC.2016.7984069>

- [10] Yadav, P., Kumar, N., Chandel, S.S., 2015. Simulation and performance analysis of a 1 kWp photovoltaic system using PVsyst, in: 4th IEEE Sponsored International Conference on Computation of Power, Energy, Information and Communication, ICCPEIC 2015. Institute of Electrical and Electronics Engineers Inc., pp. 358–363.
<https://doi.org/10.1109/ICCEPIC.2015.7259481>

The influence of sandy loam soil moisture content on its load-bearing capacity

Ahmed Elawad Eltayeb AHMED¹, György PILLINGER²,
Péter KISS²

¹ Doctoral School of Mechanical Engineering, MATE, Gödöllő

² Department of Vehicle Technology, Institute of Technology, MATE, Gödöllő

Abstract

Soil's load-bearing capacity is its ability to sustain loads applied to the land above. It is mostly determined by the kind of soil, its shear strength, and its density. The purpose of this article was to study the effect of the load-bearing capacity (pressure-sinkage relationship) on the sandy loam soil based on its moisture content level. The measurements were performed with a Bevameter technique at the laboratory of the Hungarian University of Agriculture and Life Sciences (Szent Istvan Campus). A brief introduction will define Terramechanics studies and their importance when dealing with machine-terrain interaction. The axial load acting on the terrain will lead to the sinkage of the machine, thus considering this load will help in studying the load-bearing capacity of the soil and ending up with results that are beneficial to Terramechanics studies, so improvement in the machine design or choosing the suitable machine for specific terrain. The techniques and measurements used to find soil's load-bearing capacity will be explained (Bevameter test, moisture analyzer).

Keywords

load-bearing capacity; Bevameter technique; moisture content; sandy loam soil; soil pressure-sinkage; terrain properties; vehicle-terrain interaction

1. Introduction

The soil is a very difficult material to work with in terms of mechanical properties. The fundamental issue is the wide range of material properties that might cause it to be elastic, plastic, non-homogeneous, anisotropic, compressible, expanding, or collapsing. To effectively construct a foundation, it is vital to understand the properties of the supporting soil and mathematically define its behaviour.

Off-road vehicles are utilized in a variety of industries across the globe, including agriculture, construction, cross-country transit, and military activities. Throughout history, men have made significant efforts in agriculture, logging, building, mining, exploration, recreation, and military operations to study locomotion across unprepared terrain.

Over the years, several approaches to investigating off-road vehicle mobility have been developed, including empirical techniques, computational methods, and parametric analytic methods. (Wong, 2010).

The forces and moments between the machine and the ground determine the vehicle's performance (Taheri, et al., 2014). As a result, the terrain-soil interaction during operation determines the vehicle's mobility and dynamic performance (Shibly & Iagnemma, 2005).

Terrain-vehicle machines provide guiding principles to understand better the soil-vehicle interaction. Most frequent problems faced during soil-machine interaction are encountered in the categories of excessive soil compaction, excessive wheel or track sinkage due to ground pressure, physical characteristics of both soil and vehicle, excessive wheel or track slippage and insufficient traction resulting from internal soil shear or surface friction failure. (Yong et al., 1984).

Terrain's mechanical properties are divided into two directions: the normal load-bearing capacity; pressure-sinkage relationship equations) and the tangential (shear load; shear-slippage relationship equations). (Ding et al., 2014).

When a normal load is applied by the wheel on the terrain will compact the soil (reduction of soil pores volume), thus the wheel sinks till the soil produces resistance load opposing the sinkage (is the load bearing capacity). The soil resistance to the wheel's normal load is directly affected by the two soil parameters: cohesiveness (bonding of soil particles) and angle of internal friction (resistance of movement between soil particles), thus the soil resistance is influenced by the soil density, shear strength, and the load coming from the vehicle. (Meirion-Griffith & Spenko, 2014).

The forces and moments acting at the interaction level are proportional to operating factors such as slip ratio, slip angle, normal load, and tire inflation pressure. The pressure (stresses) at the contact part cause geometrical and mechanical changes in the tire and the terrain as changes in the tire belt deformation, soil sinkage, soil deformation, erosion, and particle movement. Mechanical changes in the tire and the terrain occur upon interaction (bulk density, compaction, water content). The deformable terrains in off-road scenarios increase the complexity of modelling the cases at the contact zone (Gallrein & Bäcker, 2007). For simplifying this interaction majority of terramechanics models make certain prior assumptions. These simplifications depend on the model's applicability and necessitate computational and experimental resources. (Gipser, 2007).

2. The structure and the strength of the soil

The soil is divided into two main types: cohesive and a frictional type; In general, soils are a combination of both friction and cohesive (Inns & Kilgour, 1978). Cohesive forces depend on soil moisture suction rather than soil moisture content (Earl, 1996). Friction is the resistance between the soil particles when sliding over each other (Increases with the increase in the number of particles contacts per unit

volume) (Dumbleton & West, 1970). The increase in soil bulk density will increase soil friction (Godwin et al., 1991).

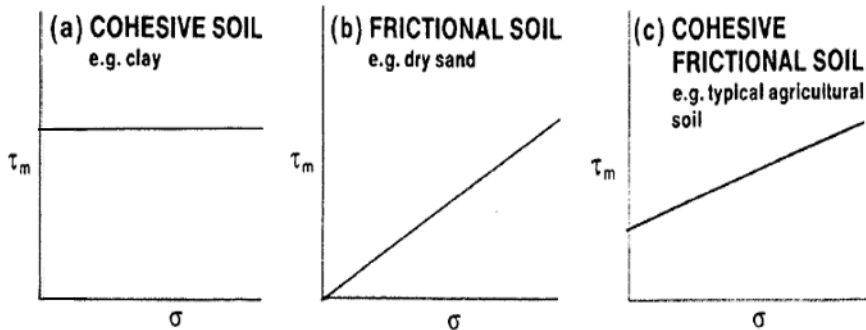


Figure 1. The strength of different soil types (Inns & Kilgour, 1978), τ_m is the shear strength, σ is the normal stress applied on the sheared surface.

Freitag reported that it is important to consider the tractive performance of the three different soil classes (cohesive, frictional, and cohesive-frictional) (Freitag, 1965). The Mohr-Coulomb diagrams of the three soil classes are shown in Figure 1.

a- Pure cohesive soil possesses only a cohesive (non-frictional) strength component; the water-saturated clay is an example.

b- Pure frictional soil has only a frictional (zero cohesion) strength component; dry sand is an example of this kind.

c- Cohesive-frictional soil class and contains both cohesive and frictional strength components; the saturated clays, loams, and sands are examples of this soil class (Ahmed, A. E. E. et al., 2021).

Distribution of the Applied Load Stresses in the Terrain

The terrain under the vehicle is modelled as either an elastic medium or as a rigid, perfectly plastic material (Wong, 2010). The elastic behaviour of a material is its tendency to return to its original geometry, but when the material enters the plastic region then it is permanently deformed and will not return to its initial geometry when removing the exerted load (Ahmed, A. E. E. et al., 2021). The two regions are shown in the stress-strain diagram shown in Figure 2.

The elasticity theory leads to the development of most theoretical investigations dealing with dense soil (for the limitation of need exceeding load bearing capacity the plastic theory reflects the soil failure) (Taghavifar & Mardani, 2017).

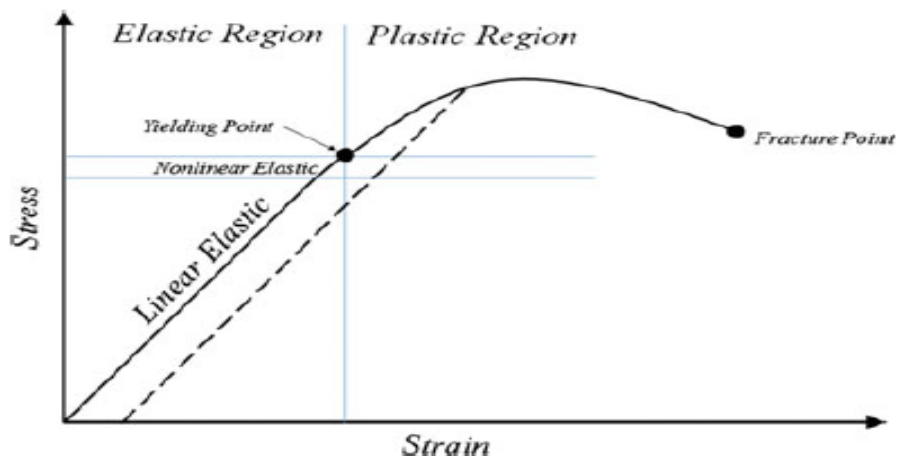


Figure 2. Soil Stress-Strain curve showing the elastic and plastic regions (Taghavifar & Mardani, 2017).

3. Moisture content

Moisture is a component present in the soil structure, and that is based on the soil's three phase-system (minerals, moisture, and air). The moisture affects the characteristics of the soil such as consistency, compatibility, cracking, swelling, shrinkage, and density. Shear strength and bearing capacity are both influenced by the physical state of the soil. The moisture content and void ratio are factors that affect soil's mechanical properties by changing cohesion and the internal friction angle. Low moisture content increases soil friction, while high moisture content decreases soil friction. Cohesion decreases when moisture content increases in loam soils and increases as moisture content increases in sandy and clay soils (Komandi, 1992). The physical composition of the soil, wetness (water content), density, and the initial compression condition all affect soil deformation caused by vehicle passage. The soil becomes more compact as the moisture levels increase (Pillinger et al., 2018).

Determining the water content in the soil is important in agriculture, mechanical, geotechnical, hydrological, and environmental engineering since moisture has an impact on the soil's characteristics (Susha et al., 2014).

4. Materials and method

Soil type and parameters

The soil as in Figure 3 has been obtained from a field belonging to the Hungarian University of Agriculture and Life Sciences (Szent Istvan Campus) and it has the following parameters as illustrated in Table 1 after sieving the soil to remove the ashes and the big particles.



Figure 3. Sample of sandy loam soil.

Table 1. Soil composition.

Soil type	Sandy loam
Sand	2 - 0.05 mm (90.50 %)
Silt	0.05 - 0.002 mm (3.20 %)
Clay	< 0.002 mm (6.30 %)

Soil moisture test

The moisture analyzer instrument (HE53 230 V) as shown in Figure 4 utilized to measure the moisture content level of the soil samples. The working principle is by drying the soil sample using heating plates. Upon drying the sample completely, it subtracts the initial mass of the soil from the remaining mass, divides the difference by the initial mass, and multiplies it by 100. The technical specifications of the moisture analyzer instrument are listed in Table 2.



Figure 4. The moisture analyzer instrument (HE53 230 V).

Table 2. Specifications of the moisture analyzer (HE53 230 V) instrument.

Model	HE53 230 V
Min. Recommended Moisture Range (% MC)	1
Readability MC	0.01 %
Drying Programs	Standard, fast
Test & adjust	Temperature (100 °C/160 °C) Weight
Drying Temperature	50 °C – 160 °C
Temperature Increments	1 °C
Display Mode	% MC, % DC, % ATRO MC, % ATRO DC, g
Voltage	230 V

Bevamer test

A Bevamer test was carried out at the Hungarian University of Agriculture and Life Sciences laboratory. The Bevamer used is shown in Figure 5 and of a pressing plate diameter of 20 cm. The load (normal load of increasing value) was applied using hydraulic force to press down the sandy loam soil; loads were measured using a load cell and provided to the computer (Catman 4.5 software Figure 7) through equipment called Spider 8 as in Figure 6. Upon the plate sinking the longitudinal deformation was also recorded using a displacement sensor and provided to the computer through the data logger.

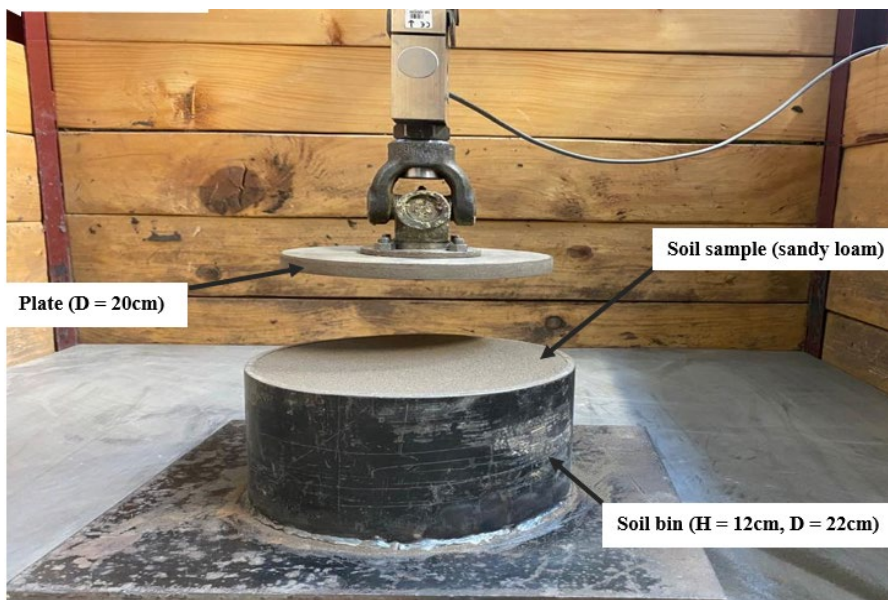


Figure 5. Shows the main structure of the Bevamer: soil bin (height = 12 cm, inner diameter = 22 cm), Plate size (diameter = 20 cm) and the soil sample.



Figure 6. The data logger (Spider 8).

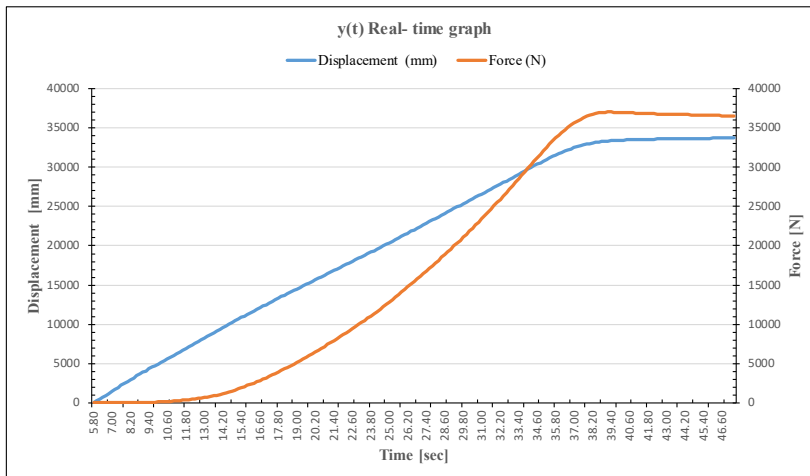


Figure 7. data recorded by Catman 4.5 software and then converted by excel (force and displacement as a function of time).

5. Results and discussion

Four samples of sandy loam soil were examined as listed in Table 3. each of the samples has a different moisture content (MC [%]). the soil bin dimensions were (height $H_1 = 12$ cm, and diameter $D = 22$ cm), the Bevameter plate size ($D = 20$ cm), the soil height after the procedure (H_2) and before the procedure is equal to the soil bin height, the sample weight (mass [kg]). Measuring the mass of the soil helps with calculating the density before (ρ_1) and after (ρ_2) the procedure from equation 1 and the density ratio ($\Delta\rho$) from equation 2. ($H/D =$ bin height/plate diameter).

$$\rho_{1,2} = \frac{m}{\pi \cdot r^2 \cdot H_{1,2}} \tag{1}$$

$$\Delta\rho = \frac{\rho_2 - \rho_1}{\rho_1} \tag{2}$$

Table 3. Specification of Bevameter test for five samples

Sample no.	H/D	MC [%]	Mass [kg]	Height [cm]	Density [g/cm ³]	Density ratio [-]
1	0.60	0.93	4.92	H ₁ = 12, H ₂ = 9.9	ρ ₁ = 1.31, ρ ₂ = 1.58	0.21
2	0.60	2.91	4.78	H ₁ = 12, H ₂ = 8.8	ρ ₁ = 1.27, ρ ₂ = 1.73	0.36
3	0.60	4.70	4.23	H ₁ = 12, H ₂ = 7.4	ρ ₁ = 1.12, ρ ₂ = 1.82	0.63
4	0.60	6.23	3.77	H ₁ = 12, H ₂ = 6.3	ρ ₁ = 1.00, ρ ₂ = 1.90	0.90

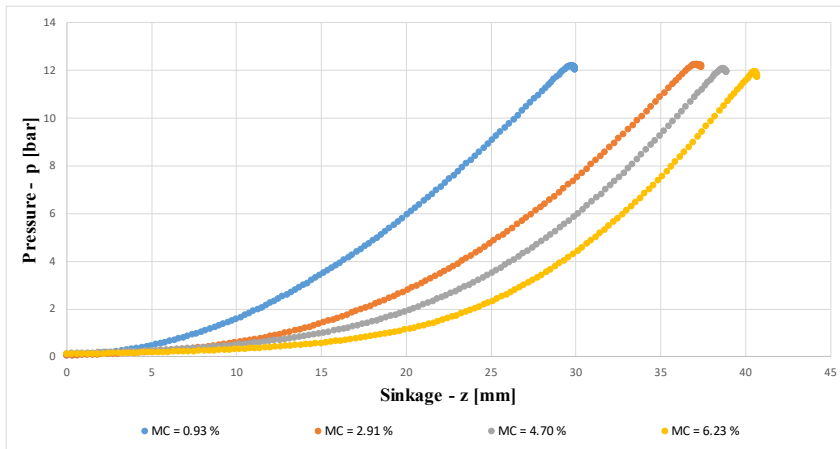


Figure 8. The Pressure – sinkage relationship at different moisture content levels for the tested soil.

Based on our experimental test made on sandy loam soil (Figure 8), appeared that with the increase in the amount of moisture content level in the soil, the sinkage of the Bevameter plate increased upon applying the same applied surface pressure under the load plate (force divided by the plate area). So, we can deduce that the soil's bearing capacity decreases with the moisture content increase (inversely proportional relationship).

In Figures 9, and 10 an exponential with the correlation coefficient, R² = 0.9632 and 0.9657 respectively, proves the inverse proportional pressure–sinkage relationship.

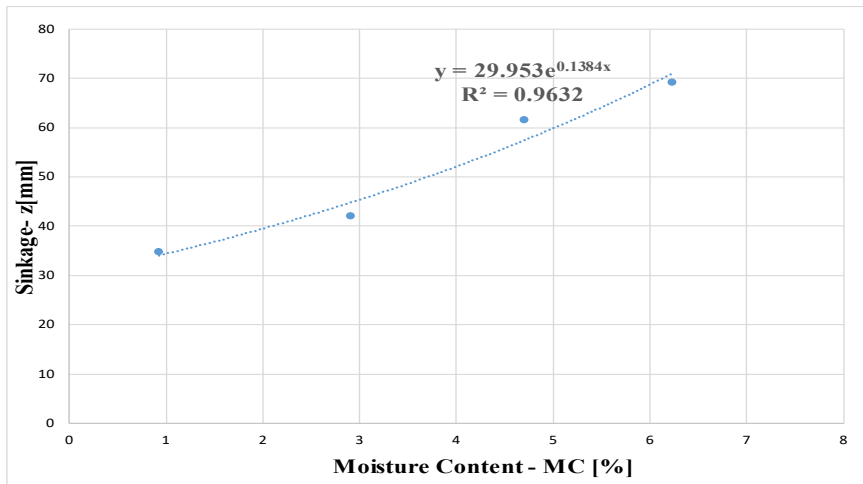


Figure 9. The sinkage - moisture content relationship for the sandy loam soil.

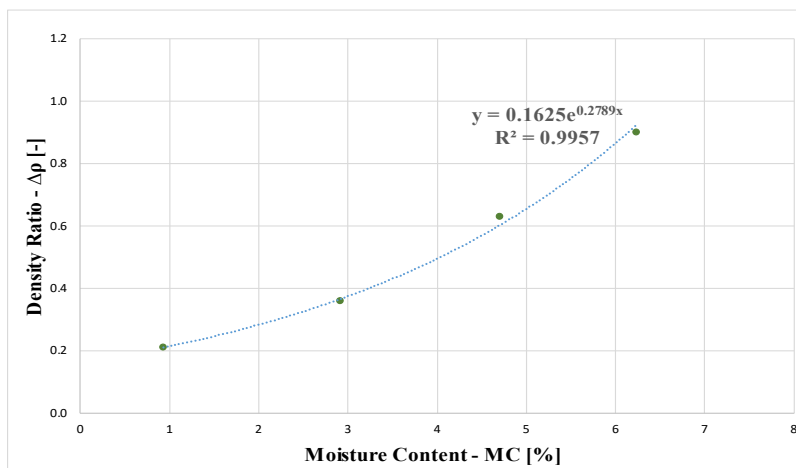


Figure 10. The density ratio - moisture content relationship in case of tested soil.

Conclusions

- Many fields (agricultural, military...) require enhancements in the vehicles used and if not enhancing, choosing the suitable vehicle for the specified mission might help accomplish it. The load-bearing capacity will help in this enhancement by measuring the normal interaction between the vehicle and the terrain. The Bevameter technique has facilitated measuring the resulting load-bearing capacity between the vehicle and the terrain.

- Furthermore, the Bevameter technique helps in measuring the normal displacement upon having normal load pressing on the terrain having at the same time the displacement being measured with the sinkage, so the resulting curve will help in studying the bearing capacity of the terrain.
- Finally, based on our experimental test made on sandy loam soil, it appears that with the increase in the moisture content level in the soil, the sinkage of the Bevameter plate increased upon applying the same load. So, we can deduce that the soil's bearing capacity decreases with the moisture content increase (directly proportional relationship). This deduction is recognized when a vehicle moving on wet soil (of the used type), that the increase in the amount of water in soil (wet soil) leads to the sinkage of the vehicle.

Acknowledgements

This work was supported by the Mechanical Engineering Doctoral School at the Hungarian University of Agriculture and Life Sciences (MATE), Gödöllő, Hungary. We would also want to express our gratitude to The Stipendium Hungaricum foundation for financing our PhD program.

References

- [1] Ahmed, A. E. E.; El Hariri, A.; Kiss, P. (2021) Soil strength and load bearing capacity measurement techniques. *HAE 2021*, 40, pp. 16-27. ISSN 0864-7410. <https://doi.org/10.17676/HAE.2021.40.16>.
- [2] Ding, L. et al. (2014) 'New perspective on characterizing the pressure-sinkage relationship of terrains for estimating interaction mechanics', *Journal of Terramechanics*. *ISTVS*, 52(1), pp. 57–76. doi: 10.1016/j.jterra.2014.03.001.
- [3] Dumbleton, M. J., & West, G. (1970). the suction and strength of reinvloulded soils. Berkshire.
- [4] Earl, R. (1996). Prediction of Trafficability and Workability using Tensiometers. *Journal of Agricultural Engineering Research*, 63(1), 27–33. <https://doi.org/10.1006/jaer.1996.0004>.
- [5] Freitag D.R., (1965), Wheels on soft soils, an analysis of existing data. Technical Report No. 3-670 USAE Waterways Experiment Station.
- [6] Gallrein, A., & Bäcker, M. (2007). CD tire: a tire model for comfort and durability applications. *Vehicle System Dynamics*, 45 (sup1), 69–77. <https://doi.org/10.1080/00423110801931771>.
- [7] Gipser, M. (2007). FTire – The tire simulation model for all applications related to vehicle dynamics. *Vehicle System Dynamics*, 45 (sup1), 139–151. <https://doi.org/10.1080/00423110801899960>.

- [8] Godwin, R. J., Warner, N. L., & Smith, D. L. O. (1991). The development of a dynamic drop-cone device for the assessment of soil strength and the effects of machinery traffic. *Journal of Agricultural Engineering Research*, 48(C), 123–131. [https://doi.org/10.1016/0021-8634\(91\)80009-4](https://doi.org/10.1016/0021-8634(91)80009-4).
- [9] Griffith, G. M., & Spenko, M. (2014). Simulation and experimental validation of a modified terramechanics model for small-wheeled vehicles. *International Journal of Vehicle Design*, 64(2/3/4), 153. doi:10.1504/ijvd.2014.058499.
- [10] Inns, F. M., & Kilgour, J. (1978). *Agricultural tyres*. London: Dunlop. Retrieved from http://books.google.co.uk/books/about/Agricultural_tyres.html?id=JB8NAQAAMAAJ&pgis=1.
- [11] Komandi, G. (1992). On the mechanical properties of soil as they affect traction, *Journal of Terramechanics*, Vol. 29, no. 4/5, pp. 373-380.
- [12] Pillinger, G., Kiss, P., Géczy, A., Hudoba, Z. (2018). Determination of soil density by cone index data, *Journal of Terramechanics* 77, 69–74.
- [13] Shibly, H., & Iagnemma, K. (2005). An equivalent soil mechanics formulation for rigid wheels in deformable terrain, with application to planetary exploration rovers, 42, 1–13. <https://doi.org/10.1016/j.jterra.2004.05.002>.
- [14] Susha Lekshmi S.U., D.N. Singh, Maryam Shojaei Baghini, (2014) A critical review of soil moisture measurement, *Measurement*, Vol 54, 2014, Pages 92-105, <https://doi.org/10.1016/j.measurement.2014.04.007>.
- [15] Taghavifar, H., & Mardani, A. (2017). *Off-road Vehicle Dynamics*, Vol. 70. Switzerland: Springer International Publishing. <https://doi.org/10.1007/978-3-319-42520-7>.
- [16] Taheri, S., Sandu, C., & Taheri, S. (2014). Finite Element Modeling of Tire Transient Characteristics in Dynamic Maneuvers. *SAE International Journal of Passenger Cars - Mechanical Systems*, 7 (1), 2014-01–0858. <https://doi.org/10.4271/2014-01-0858>.
- [17] Terzaghi, K. (1951) *Theoretical soil mechanics*. sixth. New York: John Wiley and Sons.
- [18] Wong, J. Y. (2010). *Terramechanics and Off-Road Vehicle Engineering (Second)*. Oxford, UK: Elsevier Ltd. <https://doi.org/10.1016/C2009-0-00403-6>.
- [19] Yong, R. N., Fattah, E. A., & Skiadas, N. (1984). *Vehicle Traction Mechanics*. Amsterdam: Elsevier Science.

Creation and validation of simplified mathematical model for residential building energy analysis in matlab environment

Szabolcs PÁGER¹, László FÖLDI², Gábor GÉCZI³

¹Doctoral School of Mechanical Engineering, MATE, Gödöllő

²Department of Mechatronics, Institute of Technology, MATE, Gödöllő

³Department of Environmental Analysis and Environmental Technology, Institute of Technology, MATE, Gödöllő

Abstract

The aim of this paper is to create a simplified building energy model that can predict the building's heating energy demand by taking into account the external temperature and solar radiation. The calculation requirements of our originally created model required too many resources, which is why it became necessary to simplify it. The Model was validated with measurement results. Its potential application is energy optimization and comparison of different control methods. To determine the heating energy demand, this model created in the Matlab environment takes into account: the different physical properties of the building, building location, weather, heat gains and heating system. The model was built on the basis of an existing family house, the measurement results cover a period of one year. The results calculated with Matlab were then validated with consumption data measured on the building's gas meter. The model offers the possibility to carry out calculations based on specific measurement data and on the basis of simulated data.

The main advantage of this model is that it is simple to build and requires fewer resources to perform calculations, the results can be easily generalized, and thus can be applied to other buildings as well.

Keywords

Energy Efficiency, sustainable development, environmental protection, simulation

1. Introduction

40% of the world's energy consumption is used for the energy demand of buildings and facilities (Harish, V.S.K.V. and A. Kumar, 2016). Also in Hungary, heating and cooling energy use in residential buildings accounts for 16%, while hot water generation accounts for 4% (see Fig. 1), (International Energy Agency, 2018). Our basic goal is to reduce the energy consumption of this building stock. By

optimizing energy upgrades and heating system regulation. With the characteristics of the Hungarian building stock, current literature can be found with ~100 m² buildings, which have the largest share (Csoknyai, 2022). The subject of our research was the creation of a mathematical model in which calculations and optimizations can be performed by entering data specific to a given building or building type. A white-box model seemed to be the solution for the development of the model, where after specifying the various parameters of the building, we performed our tests by modeling real physical processes.

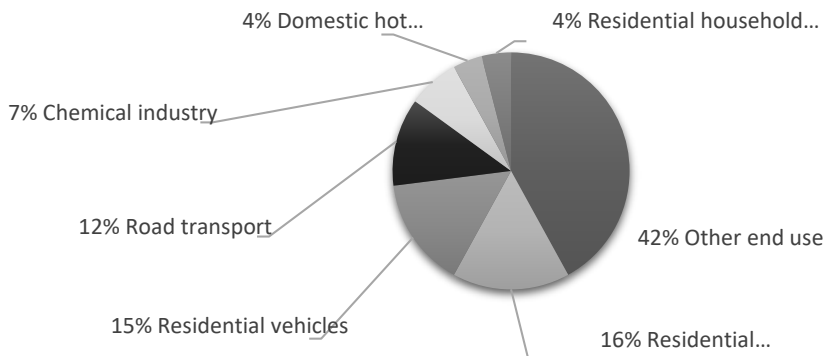


Figure 1. The six largest CO₂-emitting end uses in Hungary in 2017 (International Energy Agency, 2018)

The used software in engineering practice is suitable for determining the energetic classification of individual buildings. Optimizing and developing new processes requires a holistic approach. Modeling is needed to better understand and analyze the behavior of buildings. And for measurements to create and validate the appropriate models (Farkas, 1999).

As the reduction of energy consumption and environmental pollution came to the fore, and computer capacities and software made it possible, simulation software that could be applied to buildings also appeared, for example, Energy Plus, Transys, Blast, Therm, or the Hungarian-developed Winwatt (Harish, V.S.K.V. and A. Kumar, 2016), (Harmathy et al., 2015), (Coakley et al., 2014), (Crawley et al., 2001), (Bhandari et al., 2012), (Witte et al., 2001). With simulation procedures, we can perform the optimization based on different aspects.

Software created by different developers works with different approaches and methods. From white-box models to gray-box and black-box solutions. For research purposes, the modeling and simulation procedures where we can freely shape and expand the elements included in the model are most applicable. By reviewing the specific literature, we can observe research focusing on residential buildings or office buildings and shopping centers (Harmathy et al., 2015),

(Coakley et al., 2014), (Jain et al., 2021), (Meng Q. and M. Mourshed, 2012) (Kominek, 2014). In our area of research, scientific research has been carried out for the planning and optimization of single-family residential buildings (Mourshed, 2012), (Vadiee et al., 2020), (Kassai, 2019).

During the creation of the models, the subject of the investigation must be broken down into its elements, the processes taking place must be understood, and they must be described in mathematical form. When designing the appropriate structure, one approach is the method of energy balances, where the equilibrium temperatures are determined, which are constantly changing depending on the external weather parameters and the heat production inside the building (Meng Q. and M. Mourshed, 2012), (Mourshed, 2012), (Kassai, 2019), (Tóth et al., 2019), (Janprom et al., 2020). In the case of buildings, the built-in materials, structures, building engineering systems, and technical solutions determine the characteristics of the examined building, so we use these parameters in the model creation.

A similar conclusion was reached (Perera et al., 2016), where the simplified model was used in Matlab and Modelica environments. (Sturzenegger et al., 2014) It describes a Model Predictive Building Control solution, also using the Matlab environment. (Karmacharya et al., 2012) In his Matlab model, he used its electrical equivalents to describe the processes. It can be said unanimously that the use of simplified models during the simulation is appropriate and sufficient.

During the research, we ran into the problem that running the detailed mathematical model reached the limit of the computing capacity of the computer at our disposal. Therefore, it became necessary to simplify our validated model. This improved its transparency and the safety of running simulations. We simplified the description of physical processes. We can still use our model with a suitable $R^2=0.9962$. Our measurements run continuously, so the data are also available for the validation of the simplified model. The simulation environment is still Matlab Simulink™, in which the behavior of the building should be suitable for examining weather data and the behavior of the heating system.

In this article, we will present the simplification and validation of the model. The previously validated model was described in detail in the article (Páger et al., 2022). The new model has already been supplemented with a heating system. Thus, in the course of further research, we will deal with its optimization.

2. Experimental

representation of a simplified model

We built it on the white-box basis of the previously used Simulink model, where the individual energy processes were solved with mathematical equations. A detailed presentation of the reference building can be found in the article (Páger et al., 2022). The implementation of this is shown in the figures (see Fig. 2), (see Fig. 3).

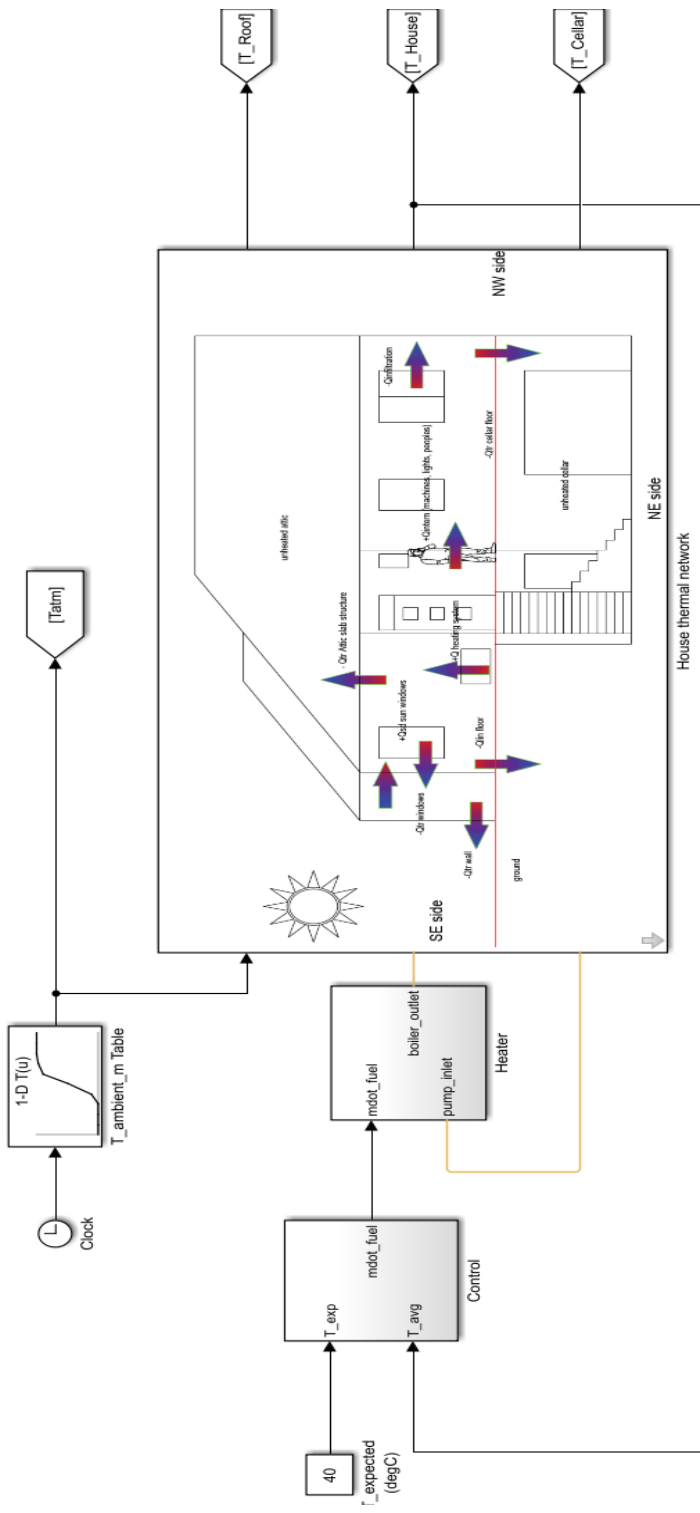


Figure 2. Complex Simulink™ model of the reference building

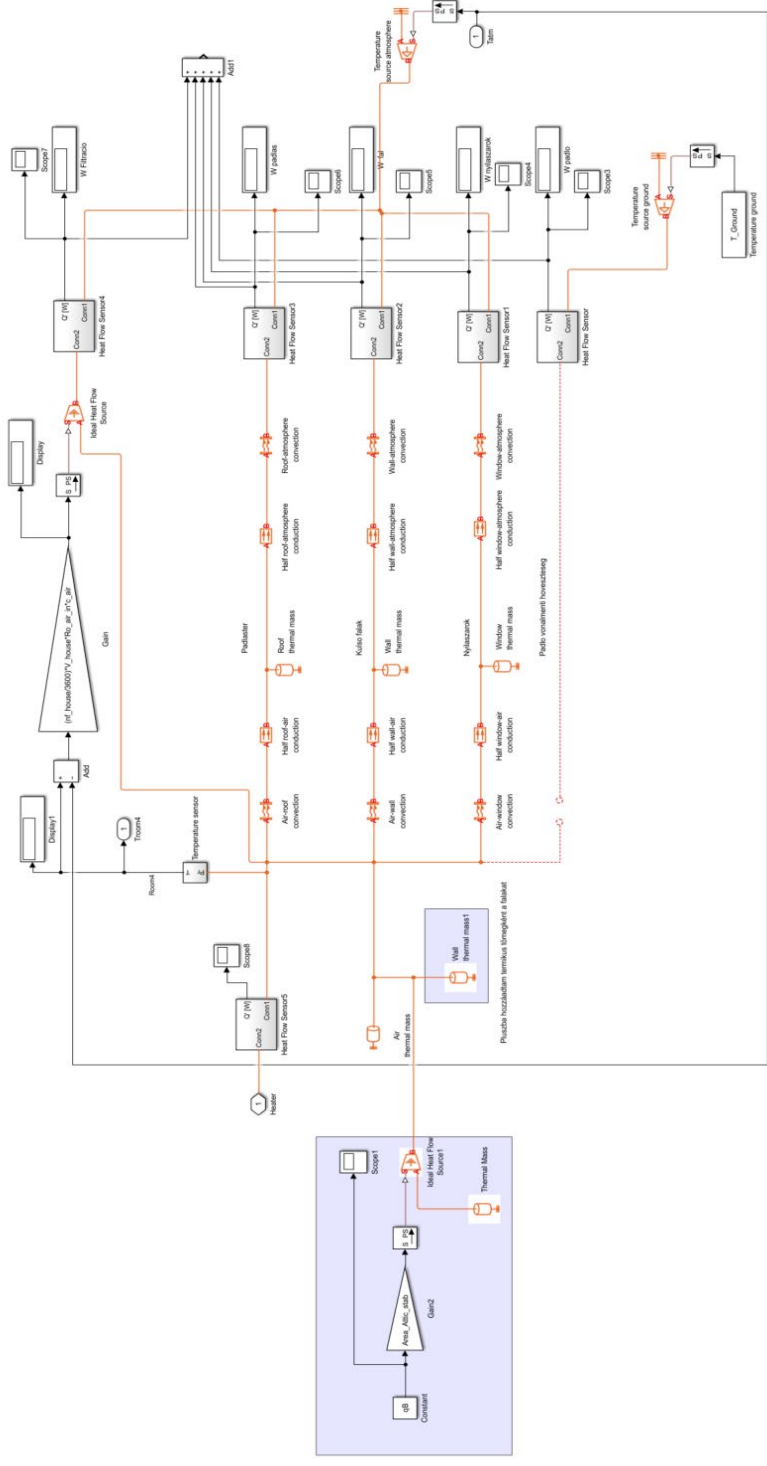


Figure 3. A composite model of the living space of the reference building

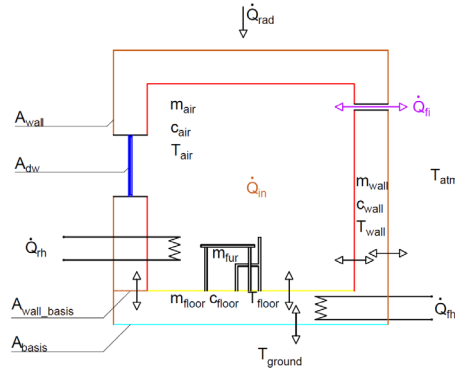


Figure 4. Scheme of the simplified model

It can be seen from the figures that a complex model was created, which, however, ran into computational limitations considering the practical modeling goals. Based on these, we decided to simplify the model. Instead of complicating all bounding elements and bounding spaces, we defined resulting values. Thus, the building could be simplified based on its most characteristic physical parameters. (Floor area, ceiling height, floor perimeter, boundary surfaces, geolocation). Figures (see Fig. 4) shows the scheme of the simplified model. The color markings used in the drawing are the same as the colors used in the model, thus facilitating the identification of individual structures.

The names of the symbols used in the figure (see Fig. 4) are included in the differential equations used in the thermal engineering modelling of the reference building. Thermal engineering modelling of the reference building Simplified differential equations describing the thermal behaviour of the residential building: Differential equation describing the internal temperature of the residential building Eq. 1.

$$\begin{aligned}
 (m_{air} \cdot c_{air} + m_{water_{rh}} \cdot c_{water} + m_{fur} \cdot c_{fur}) \cdot \frac{dT_{air}}{dt} = & \\
 P_{rh} + n f_{house} \cdot V_{house} \cdot \rho_{air} \cdot c_{air} + & \\
 q_B \cdot A_{floor} + A_{wall} \cdot k_{air_{wall}} \cdot (T_{wall} - T_{air}) + A_{floor} \cdot k_{floor_{air}} \cdot & \\
 \cdot (T_{floor} - T_{air}) + A_{dw} \cdot k_{dw_{atm}} \cdot (T_{atm} - T_{air}) &
 \end{aligned} \quad (1)$$

Differential equation describing the temperature of the boundary surfaces of the residential building Eq. 2.

$$\begin{aligned}
 (m_{wall} \cdot c_{wall}) \cdot \frac{dT_{wall}}{dt} = Q_{rad} - A_{wall} \cdot k_{air_{wall}} \cdot & \\
 \cdot (T_{wall} - T_{air}) + L_{wall} \cdot FI \cdot (T_{floor} - T_{wall}) + & \\
 + A_{wall} \cdot k_{wall_{atm}} \cdot (T_{atm} - T_{wall}) &
 \end{aligned} \quad (2)$$

Differential equation describing the temperature of the floor of a residential building Eq. 3.

$$\begin{aligned} & (m_{floor} \cdot c_{floor} + m_{water} \cdot c_{water}) \cdot \frac{dT_{floor}}{dt} = \\ & P_{fh} - A_{floor} \cdot k_{floor_air} \cdot (T_{floor} - T_{air}) - L_{wall} \cdot FI \cdot \\ & (T_{floor} - T_{wall}) + A_{floor} \cdot k_{floor_ground} \cdot (T_{ground} - T_{floor}) \end{aligned} \quad (3)$$

Notation	Designation	Unit
T_{air}	Air temperature	°C
T_{floor}	floor temperature	°C
m_{air}	air mass	kg
m_{wall}	wall mass	kg
m_{water_fh}	mass of floor heating water	kg
c_{air}	air specific heat	J/kg*K
c_{fur}	the average specific heat of the equipment	J/kg*K
P_{rh}	radiator heating performance	W
nf_{house}	filtration factor	l/h
ρ_{air}	air density	kg/m ³
A_{floor}	floor heating surface	m ²
A_{wall}	wall surface	m ²
k_{air_wall}	heat transfer factor air - wall	W/m ² *K
k_{wall_atm}	heat transfer factor environment - wall	W/m ² *K
k_{dw_atm}	heat transfer factor doors and windows - environment	W/m ² *K
FI	linear heat transfer between the walls and the ground	W/m
T_{atm}	Ambient temperature	°C
T_{wall}	wall temperature	°C
m_{fur}	mass of equipment	kg
m_{water_rh}	the mass of radiator heating water	kg
c_{water}	specific heat of water	J/kg*K
c_{wall}	specific heat of the wall	J/kg*K
P_{fh}	floor heating performance	W
V_{house}	House air volume	m ³
q_B	Internal heat source	W/m ²
A_{dw}	surface of windows and doors	m ²
L_{wall}	wall length	m
k_{floor_air}	heat transfer factor air - floor	W/m ² *K
k_{floor_ground}	heat transfer factor floor - ground	W/m ² *K
Q_{rad}	emission	W/m ²

Expansion of the model with the heating system

For the design of the heating system, we carried out the dimensioning of the realized system with the help of building engineering sizing software. Adapted to the research goals, in this case too we made the necessary simplifications in terms of the operation and optimization of the model. The diagram (see Fig. 6) shows the design of the building's entire heating system. We used IMIHecos version 5.10.07 software for sizing.

In the case of the heating system, after the simplifications were made, the simplifications and mergers corresponding to the figure (see Fig. 7) were carried out. We summarized the mass flows and heating capacities of the radiator circuits, as well as the surfaces and mass flows of the floor heating circuits. We scaled down the heating flow and return temperatures as well.

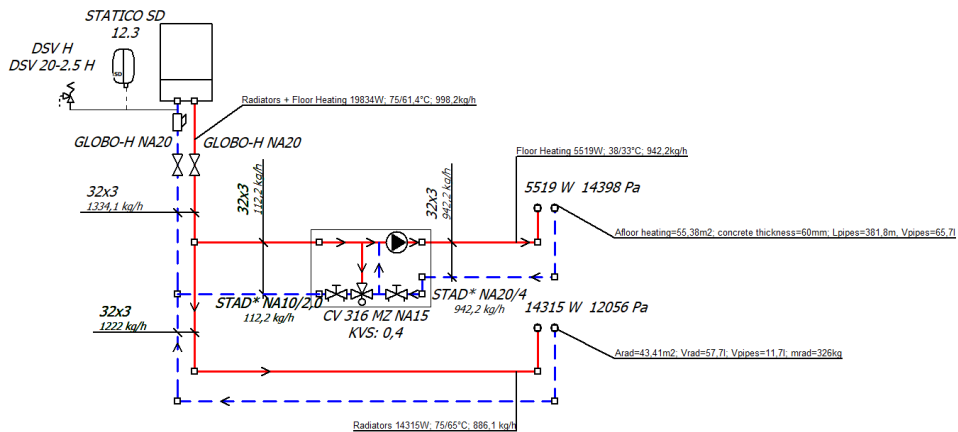


Figure 7. The heating system of the Reference Building after the simplifications

During the design of the model, we took into account the surfaces and water content of the radiators. Also, the water content and layer thickness of the underfloor heating system. Based on these, the model with the heating system was completed.

3. Results and discussion

Identification of the thermal engineering model of a reference building based on measurement results

In the case of the reference building, we have internal and external temperature and solar gain data at 1-hour intervals. The building's heating energy consumption is known with monthly readings based on the gas meter. Based on the use of the building, we distinguish between winter and summer conditions. Winter condition During the heating period, the building is used in a controlled manner and with a

shorter supply of fresh air. While in summer it is typically used with more ventilation. Based on this, we carried out the identification. The examined period is the period from 01.01.2021 to 31.12.2021. The measurements were performed with T-type Cu-CuNi thermocouples, which were fixed and stored in 2 ALMEMO 2590-4S (Alhborn Messtechnik, Germany).

Identification of model parameters in summer and winter conditions

In summer condition

We identify the model by comparing the completed model and the measurement results. We are looking for the value of q_B , internal specific heat production, and n filtration. One of the steps in creating the model is the determination of these two parameters, where the difference between the measured and calculated values is the smallest. This was the minimum search of the objective function established by the method of least squares. Eq. 4

$$J(q_B, n) = \int_0^t (T_{house_m} - T_{house_sz})^2 \cdot dt \Rightarrow \min \quad (4)$$

where

- q_B Specific internal heat gain, W/m²
- n Filtration, 1/h
- T_{house_m} Internal measured temperature of living space, °C
- T_{house_sz} Calculated interior temperature of living space, °C
- t time, s

To determine the value of the parameters, the built-in function of Matlab Simulink™ `fminsearch` was used to find the minimum of the objective function based on a specified starting value. The figure (see Fig. 8) shows the block diagram of the objective function.

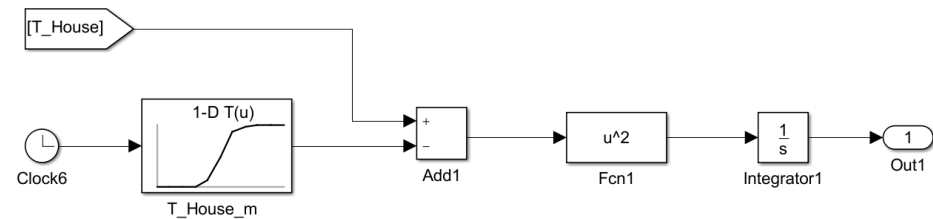


Figure 8. Realization of the objective function

In summer conditions $q_b=4.9687$ W/m², $n= 1.7166$ l/h values were obtained.

In the winter state, we also performed the identification of the parameters, where $q_b=4.9687$ W/m², $n= 0,6807$ l/h values were given. The obtained values correspond to the values used in engineering practice.

Presentation of the control method of the reference building

There is an on/off room thermostat in the building. During operation, the set temperature setpoint was 20.5°C. The control hysteresis is 1°C. We also incorporated this control method into our model. The figure (see Fig. 9) shows the elements of the room thermostat in the model.

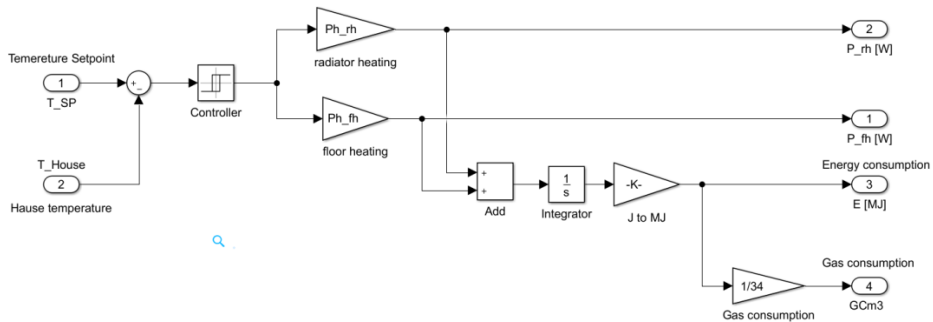


Figure 9. Model of the room thermostat

3.4 Model validation based on measured external and internal temperature, solar radiation, and gas consumption data

After identifying the parameters of the model, we also performed its validation. We determined all the measured data by calculation. Based on these, the measured and calculated gas consumption $R^2=0.9962$ was obtained.

(see Fig. 10) shows the temperatures measured and calculated based on the identified parameters of the summer state.

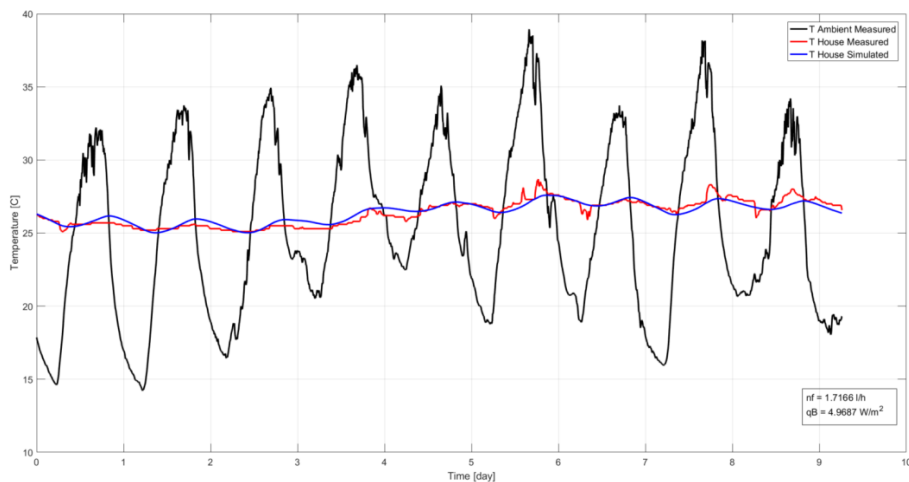


Figure 10. Temperature values measured and calculated for the period 01.01.2021 - 31.12.2021

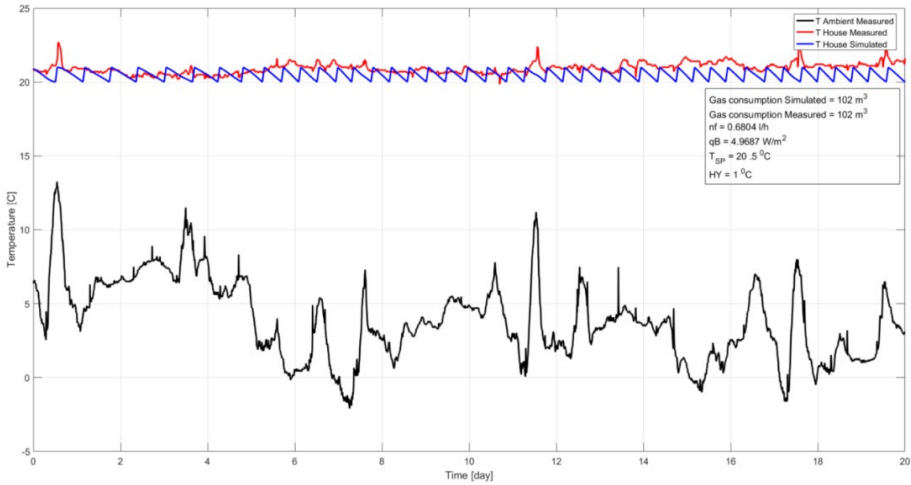


Figure 11. Temperature measured and calculated values for the period 01.01.2021 - 31.12.2021

The figure (see Fig. 11) shows the measured and calculated temperature data.

Results

We have successfully simplified the model included in our objective. The original complex model was too complicated for our later investigations, so it became necessary to simplify it. The simplified model is suitable for examining the energy savings that can be achieved with different control methods. To compare heating systems.

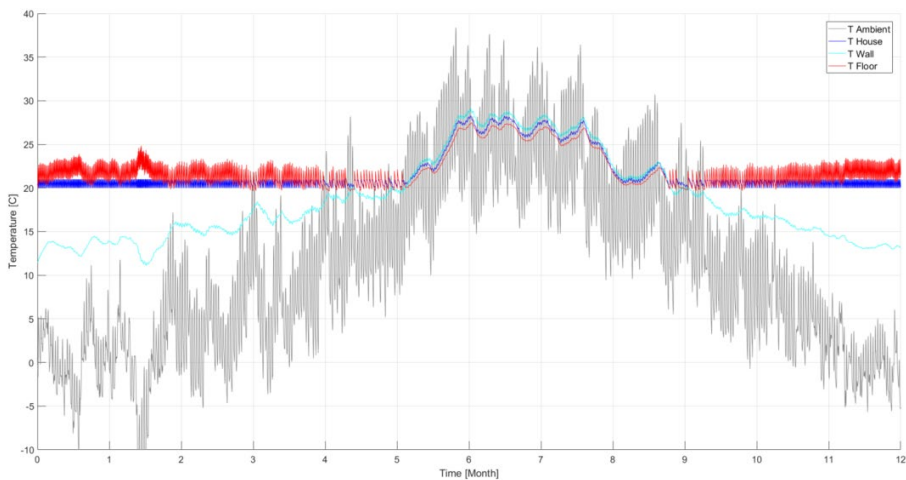


Figure 12. Measured and calculated values of temperature

We managed to create a model environment suitable for fast simulation that still works on the white-box principle. We performed the model based on the temperature data measured in the apartment building and its surroundings, the identification of two parameters in summer and winter, and the model was validated based on the radiation and temperature data downloaded to the given geographical coordinate, as well as the gas consumption.

The figure (see Fig. 12) shows the change in temperature values over the course of one year. The beginning and end of the heating period, as well as the heating limit temperature, can be easily determined from the figure.

The figure (see Fig. 13) shows the gas consumption data calculated by the model and measured. The heating periods can also be seen in this figure.

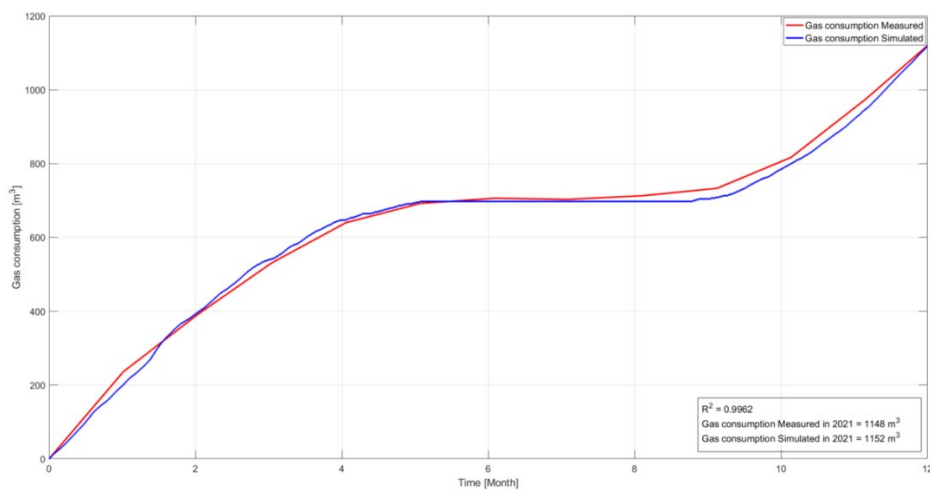


Figure 13. Measured and calculated gas consumption period 01.01.2021-31.12.2021

Based on the identified parameters, the model $R=0.9981$; A value of $R^2=0.9962$ was obtained, which we considered being sufficiently accurate.

Its main application is to provide a modeling environment for our further research, where we can compare energy-saving solutions.

Conclusions

In this paper, the simplification and validation of a reference-building model were presented. The purpose of creating the model was to simplify the calculation procedures. With this model, we have the opportunity to examine the energy efficiency of these buildings, carry out simulations of modernizations, and compare different control methods. Since the model is based on the white-box principle, it can easily be applied to other buildings as well. Using the model, we will have the opportunity to examine the effect of individual interventions on CO₂

emissions and energy savings through simulations. Modernizing these buildings and making the new buildings as modern as possible is our common interest. In this way, the operating costs and CO₂ emissions of our buildings can be reduced, even with a higher level of comfort. Modeling and simulation, as well as optimization, provide a solution for this.

References

- [1] Bhandari M., S. Shrestha, J. New (2012) Evaluation of weather datasets for building energy simulation, *Energy and Buildings* 49 p. 109-118
<https://doi.org/10.1016/j.enbuild.2012.01.033>
- [2] Coakley D., P. Raftery, K. Marcus (2014) A review of methods to match building energy simulation models to measured data, *Renewable and Sustainable Energy Reviews* 37, p. 123-141
<https://doi.org/10.1016/j.rser.2014.05.007>
- [3] Crawley D. B., et al. (2001), EnergyPlus: creating a new-generation building energy simulation program, *Energy and Buildings* 33 p. 319-331
[https://doi.org/10.1016/S0378-7788\(00\)00114-6](https://doi.org/10.1016/S0378-7788(00)00114-6)
- [4] Csoknyai Tamás (2022), A magyarországi lakóépület állomány energetikai elemzése épülettipológián alapuló modellezéssel, *Magyar Épületgépészet* 71: 6 pp. 3-10. , 8 p.
- [5] Farkas I.(1999), Számítógépes szimuláció, *Egyetemi Jegyzet* 48-54
- [6] Harish, V.S.K.V., A. Kumar (2016), A review of modeling and simulation of building energy systems, *Renewable and Sustainable Energy Reviews* 56, p. 1272-1292 <https://doi.org/10.1016/j.rser.2015.12.040>
- [7] Harmathy N. L., R. J. Folic, Z. Magyar (2015), Energy Performance Modelling and Heat Recovery Unit Efficiency Assessment of an Office Building, *Thermal Science* 19 (3) p. 865-880
<https://doi.org/10.2298/TSCI140311102H>
- [8] International Energy Agency (2018), A hat legnagyobb CO₂ kibocsátó végfelhasználás Magyarországon 2017-ben
- [9] Jain N., E. Burman, D. Mumovic, M. Davies (2021) Managing energy performance in buildings from design to operation using modelling and calibration, *Building Services Engineering Research and Technology* 42, ISSN 0143-6244 p. 517-531 <https://doi.org/10.1177/01436244211008317>
- [10] Janprom K., W. Permpoonsinsup, S. Wangnipparnto (2020) 17. Intelligent Tuning of PID Using Metaheuristic Optimization for Temperature and Relative Humidity Control of Comfortable Rooms, *Journal of Control Science and Engineering*) <https://doi.org/10.1155/2020/2596549>
- [11] Karmacharya S., G. Putrus, C. Underwood, K. Mahmkamov (2012), Thermal modelling of the building and its HVAC system using Matlab/Simulink, 2nd International Symposium on Environment-Friendly Energies and Application 202-206

- [12] Kassai M. (2019), Családi ház energetikai vizsgálata dinamikus szimulációval, Magyar Épületgépészet 68 (4) 13-18
- [13] Kominek P. (2014), Heat Supply Optimization, Advanced Materials Research 1041 p. 139-145
<https://doi.org/10.4028/www.scientific.net/AMR.1041.139>
- [14] Meng Q., M. Mourshed (2012), Degree-day based non-domestic building energy analytics and modelling should use building and type specific base temperatures. Energy and Buildings 155, ISSN 0378-7788 p. 260-268.
<http://dx.doi.org/10.1016/j.enbuild.2017.09.034>
- [15] Mourshed M. (2012) Relationship between annual mean temperature and degree-days, Energy and Buildings 54, ISSN 0378-7788 p. 418-425.
<https://doi.org/10.1016/j.enbuild.2012.07.024>
- [16] Páger Sz. L. Földi, G. Géczi (2022), Matematikai modell fejlesztése és validálása lakóépületek energiaigényét befolyásoló hidraulikai kapcsolások vizsgálatára, Magyar Energetika 29: 3 pp. 14-21. , 8 p.
- [17] Perera, D.W.U., D. Winkler, M. Skeie (2016), Multi-floor building heating models in MATLAB and Modelica environments, Applied Energy 176, pp 46-57 <https://doi.org/10.1016/j.apenergy.2016.02.143>
- [18] Sturzenegger D., D. Gyalistras, V. Semeraro, M.Morari, R. S. Smith (2014) BRCM Matlab Toolbox: Model generation for model predictive building control
- [19] Conference Paper in Proceedings of the American Control Conference DOI: 10.1109/ACC.2014.6858967
- [20] Tóth J., V. Erdélyi, L. Jánosi, I. Farkas (2019) Termikus napenergia-hasznosító rendszer kismintamodelljének identifikációja, Magyar Energetika 26, ISSN: 1216-8599 18-23.
- [21] Vadiée A., A. Doodoo A. E. Jalilzadehazhari (2020), Heat supply comparison in a single-family house with radiator and floor heating systems. Buildings 10(1) ISSN: 2075-5309 <https://doi.org/10.3390/buildings10010005>
- [22] Witte M. J., R. H. Henninger, J. Glazer, D. B. Crawley (2001), Testing and validation of a new building energy simulation program, Building Simulation Seventh International IBPSA Conference p. 353-359
http://www.ibpsa.org/proceedings/bs2001/bs01_0353_360.pdf

3D metalprinting by CMT technology

Sándor FENYVESI¹, Gyula Ferenc VASVÁRI¹,
Róbert Zsolt KERESZTES², László ZSIDAI²

¹Department of Mechanical Engineering, Faculty of Engineering
and Information Technology, University of Pécs,

²Department of Materials Science and Engineering Processes,
Institute of Technology, MATE Gödöllő

Abstract

Nowadays, there is a growing struggle for more time and cost-efficient production. Therefore, manufacturing technologies have evolved rapidly, including additive technologies. New approaches to component manufacturing and repair technologies are needed to reduce weight and storage capacity.

In this article we will focus mainly on the technology of DED (Direct Energy Deposition). We present the different technical options and their characteristics. Especially will be paid to the additive application of CMT technology. Using a 3D printed part, we will demonstrate the surface roughness that can be expected when using WAAM-CMT technology.

In the following, we will point out that, alongside additive technologies, it is usually unavoidable to complement manufacturing with subtractive technologies.

Keywords

Direct Energy Deposition, 3D print, additive manufacturing, WAAM-CMT technology

1. Introduction

Additive manufacturing (AM) is a material-additive technology that includes a wide range of manufacturing processes. These methods are used to build up a product layer by layer, producing three-dimensional objects, i.e. 3D printed (Julián Israel Aguilar-Duque et al., 2020).

Within the additive manufacturing system, three sub-processes can be distinguished. The first is the process of designing and developing the part, which requires special CAD software such as SolidWorks, SolidEdge, etc. In this stage, the engineer can design not only the shape of the part, but also its strength and mechanical properties.

The second stage is to prepare the parts to be printed using a pre-processing software (slicer), such as Cura or other slicing software. Slicing software is usually used to import STL (preferred for stereolithography), IGES or AMF (optimized parts and lattice structures) files. Then, layers are defined on the model, according

to the printing technology and the required part properties, and other additional elements (e.g. supports, skirts) are created if necessary. Based on the G-code generated by the program, the AM machine can start the production.

The third stage is linked to production. It is necessary to choose the printing technology taking into account the strength characteristics, shape, size of the part and other properties.

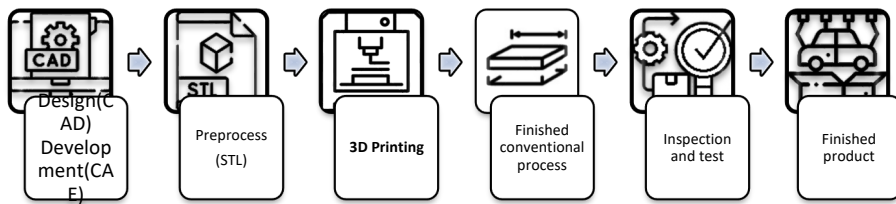


Figure 1. Process of the additive technology

Classification of metal AM

Binder Jetting	Powder Bed and inkjet 3D printing (3DP)
Powder Bed Fusion	Direct Metal Laser Sintering (DMLS) Selectiv Laser Sintering (SLS) Selectiv Laser Melting (SLM) Electron Beam Melting (EBM)
Sheet Lamination	Ultrasonic Consolidation (UC)
DirectEnergy Deposition	Electron Beam Freeform Fabrication (EBF) Wire-laser AM (WLAM) Wire-Arc AM (WAAM)

Figure 2. Classification of metal AM

Additive manufacturing, or metal 3D printing as we know it in popular parlance, has developed at a very rapid pace in recent times. Previously, the focus was on machining, where prefabricated parts were produced in larger sizes, using cutting technology (e.g. turning, milling) to achieve the final shape, size and surface roughness. This adds considerable time and cost to the part production process, and often limits the shape and complexity of the parts (Stephen Mellor et al., 2014). Nowadays, additive manufacturing is feasible with many of the materials

used in industry, including the engineering alloys of steel, aluminium and titanium. Further experiments are also being carried out to investigate micro and macro material structure changes in these technologies.

There are seven categories available for the production of metal parts, including four additive processes, such as binder jetting, power bead fusion, sheet lamination, and direct energy deposition (Johnnie Liew Zhong Li et al., 2019). These categories and their classes are shown in Figure 2.

In the rest of this article, we focus on the Direct Energy Deposition class. Nowadays, the technologies included on class are developing very dynamically, due to cost efficiency and productivity.

2. Technologies and methods

Material

The 3D metal printing offers a range of materials. Because of the favourable properties of the material and its wide range of applications, we will use AlMg4.5Mn0.7-et (EN AW-5083) as a basic material. It is a medium-strength material, very resistant to chemicals and non-hardenable. It has excellent polishability and very good corrosion resistance. The weldability of the material is adequate and the welding seams have almost the same corrosion resistance as the base material. Poor machinability in soft condition, fair in hard condition. Resistant to corrosion and seawater, suitable for medium-use constructions. Used in the food and chemical industries, as well as in construction for exterior and interior architectural elements, and also in the automotive and shipbuilding industries (Abir Bouhamed et al., 2021).

Table 1. Properties of EN AW-5083 material

Material number (DIN EN 573)	Short symbol (DIN EN 573)	Tensile strength Rm [MPa]	Proof stress Rp0,2 [MPa]	Surface finish
EN AW-5083	AlMg4,5Mn	>275	>125	mill-finish

EBF

The Electron Beam Fabrication (EBF) is a layer by layer process that uses CNC (Computer Numerical Control) technique to produce metallic parts with complex geometry. EBF is a direct metal deposition process in which metallic raw material, typically in the form of wire, is fed into a liquid weld pool which is generated by an electron beam focused on substrate plate. The electron beam-wire feeder unit traverses the toolpath recorded in the G-code, thus building up the layers. Parts produced by this method are made directly from computer-aided design files, without moulds or cutting tools.

The electron beam can also be used for secondary processing, such as surface melting or hole drilling. The production of the electron beam and the coupling of

the electron beam to the raw material makes the EBF process extremely energy efficient. Virtually 100% of the raw material is captured in the finished deposit. The EBF process can rapidly process all weldable alloys, including highly reflective materials such as aluminium and copper. Using multiple wire feeders, functionally graded parts can be produced (Robert A. Hafley et al., 2007).

Direct energy deposition includes another class of metal AM techniques that use solid wire instead of powder. Electron beam fabrication (EBF) is one of the main techniques in this class. EBF was developed by Lockheed Martin (Bethesda, MD) in 1999 and commercialized in 2002. This technology has been extensively studied and further developed at NASA Langley Research Center (Hampton, VA) for the fabrication of structures from aerospace materials such as aluminium, titanium, nickel alloys, titanium aluminides, metal matrix composites and high-strength steels. The EBF technique works in a similar way to LENS, except that an electron beam is used as the heat source. The EBF process is operated in a vacuum environment (14kPa or lower) and a metal wire dispensing system is incorporated to push the welding wire into the molten pool. The electron beam can be very precisely controlled and deflected and is very effectively coupled with highly reflective materials. The efficiency of this process is close to 100% in wire consumption and 95% in energy consumption. The EBF system schematic is shown in Figure 3..

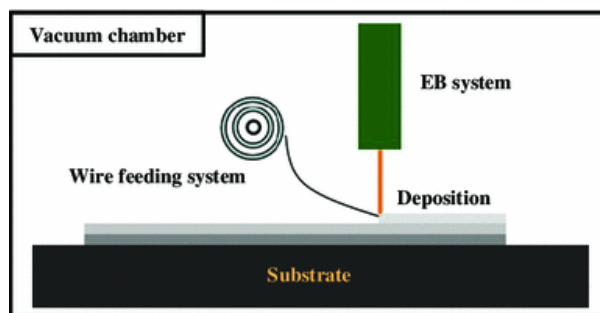


Figure 3. Schematic representation of EBF system (Zhai et al., 2014)

WLAM

Wire and laser additive manufacturing (WLAM) is an AM process for the production of free-form metal parts using additive as metal wire and a laser energy source. To operate the WLAM system, a laser as energy source, an automatic wire feed system, a computer numerical control worktable and some additional equipment (e.g. shielding gas, preheater, cooling system) are required. A robotic system may be suitable instead of a computer numerical control workbench to produce the correct shape. The WLAM system illustration is shown in Figure 4.

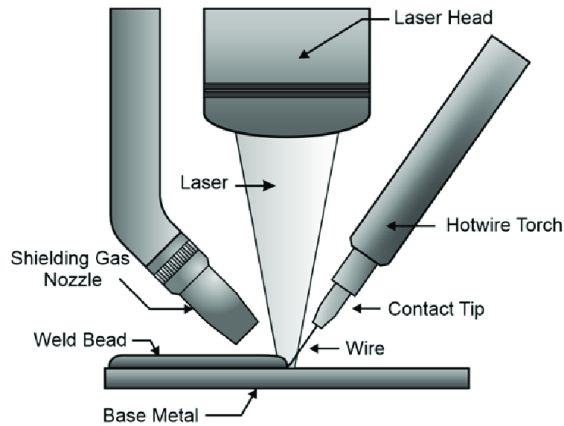


Figure 4. Illustration of the WLAM (Alexander Arbogast et al., 2020)

The WLAM process can produce a wide range of metal and alloy parts. By moving the laser head and wire feeder unit or by moving the bed appropriately, the weld pool can be moved to form a layer on the substrate plate after solidification (Heralic Almir, 2012).

WAAM

Wire arc additive manufacturing (WAAM) is the process of manufacturing a product by melting the welding wire in an electric arc and welding it layer by layer. Technically, it is an overlay welding process with a CNC machine. Figure 5. shows the schematic of WAAM.

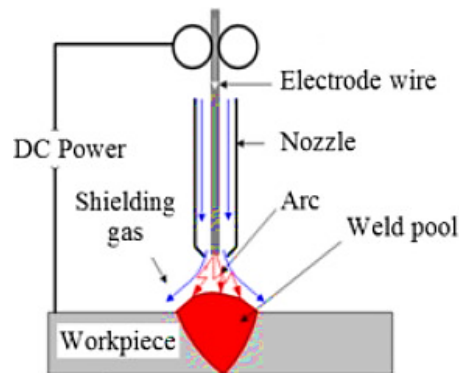


Figure 5. Illustration of WAAM (Çam Gürel, 2022)

CMT technology

During the CMT (Cold Metal Transfer) process the wire electrode is in contact with the molten pool, the servo motor of the "robacter drive" welding gun turns under digital

process control, causing the wire to retract and mechanically facilitating the transfer of the metal droplet. During the metal transfer, the current is reduced to almost zero and spatter formation is avoided. As soon as the transfer is complete, the arc is re-ignited and the wire is fed forward again by the return of the set welding current.

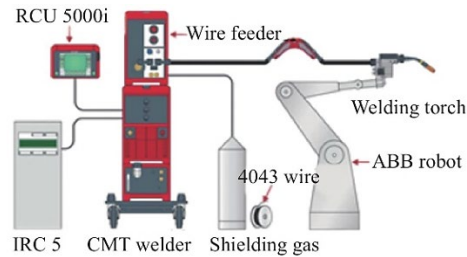


Figure 6. Illustration of CMT based WAAM (Zhi-qiang Liu et al., 2020)

When using CMT technology, cycle times can be adjusted depending on variables, welding characteristics. During the wire feed, progression and regression operations are carried out at an average rate of 63 times per second, alternating hot and cold processes (Furukawa K., 2006).

In the CMT process, the metal droplet transfer is carried out by wire regression, technically without affecting the current. When the arc is ignited, the wire moves forward and short-circuits in contact with the weld pool, and the current drops to near zero as the wire is removed. The arc heat input is designed to return immediately to the cooling state and the hot and cold processes alternate automatically, causing the current to drop suddenly and the welding heat input to drop significantly (Furukawa K., 2006).

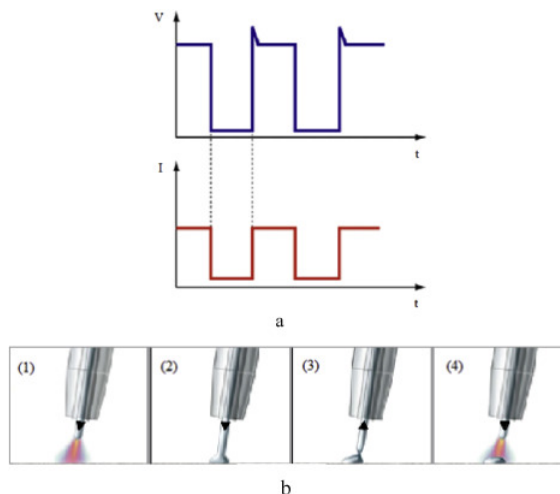


Figure 7. (a) Voltage and current change during CMT process; (b) CMT metal transfer sequence (J. Martikainen et al., 2013)

3. Roughness measurement

The characteristics of the surface quality are determined by the shape variations, roughness and waviness of the machined surface and the different properties of the sub-surface layer.

One of the best known surface texture parameter is Ra (average roughness). Measures the deviation of the part surface from a mean height. It is the arithmetic mean of protrusions and indentations, independent of the sign, of equal pitch over a given length. Roughness parameters are included in the ISO 4287:1997 standard.

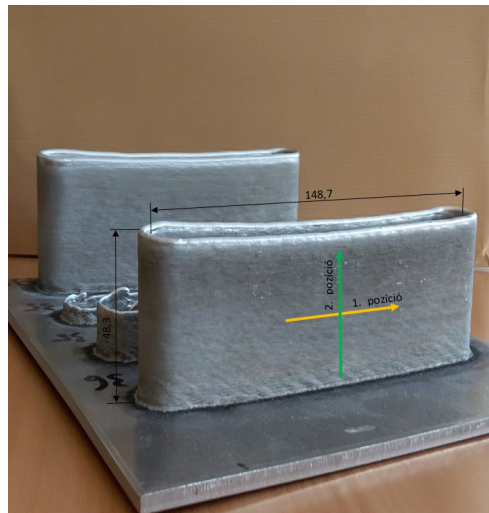


Figure 8. Sample printed Vasvári et al. marked the directions for measuring surface roughness

To measure the surface roughness of the samples, a Mitutoyo SJ-201 surface roughness tester was used. Measurements were taken at several locations and in several directions. The surface roughness direction was measured on surfaces parallel to the print and perpendicular to the print line, as shown in Figure 8.

4. Results

Dimensions (Part)

AM can be used to produce parts of different sizes and material qualities. Buildings, bridges, turbine blades, medical devices can be printed (C. Buchanan et al., 2019), (Ange Lu et al., 2020), (David E. Cooper et al., 2012), (Zhai et al., 2014). Many technologies have been developed for metal 3D printing, but choosing the optimal process is crucial as Li et al. (Johnnie Liew Zhong Li et al., 2019). Obviously, the many different geometries can be created by different

processes at various speeds. Furthermore, the optimum size and speed of production must also be considered (Iván Taberero et al., 2018).

Roughness of 3D printed part

For parts printed by Vasvári et al., the average roughness varies between Ra 12 and 14. The influence of AM technology parameters on roughness has not yet been investigated in their research. However, they have investigated the effect of changing the welding parameters on the mechanical properties of the material (Gyula Ferenc Vasvári et al., 2021).

Table 2. Values of the roughnesses

	1. direction	2. direction
Roughness [μm]	5,18	14,74

Surface roughness is not only important from a mechanical point of view. Bacterial adhesion is much less on a smooth surface. Compared to a surface with Ra205 roughness, Ra1 has only 2% of bacterial adhesion, according to a study by Ange Lu et al. (Ange Lu et al., 2020).

Crowninshield et al.'s article shows that implants with a larger surface roughness have greater fixation strength, and implants with a smaller surface roughness wear less bone tissue. Apparently, Ra 3.5 μm is the limit that no longer significantly increased implant-bone adhesion (Roy D. Crowninshield et al., 1998).

Effects of varying parameters

WAAM-CMT metal printing has several variables, such as arc current and arc voltage, wire feed rate, welding speed and shielding gas flow rate. These parameters have a major impact on the heat input rate, strength properties and surface quality of the part. Su et al. (Chuanchu Su et al., 2019) show the close relationship between welding speed, grain size and welded layers. The latter variable also affects the surface roughness characteristics. Feng et al. (Yuehai Feng et al., 2018) also pointed out the effects of changing parameters, with the difference that they used a double-wire feeder.

Martina et al. have optimised the calculation of wall width, layer height and the most appropriate process parameters for a proprietary machine (F. Martina et al., 2012). Cooper et al. in their paper point out the surface roughness of surfaces in different locations using DMLS, but they also reported a large variance, but still were able to predict significant material and material savings (David E. Cooper et al., 2012).

Summary

The introduction of AM alongside the traditional manufacturing structure can present challenges in terms of human resource skills, manufacturing processes and material handling. Guidelines have already been established for the design of 3D printed parts, which will greatly contribute to the economical creation of parts. Various experiments have been carried out on different materials (e.g., aluminium, titanium, steel alloys) to optimise different values, but these have mostly concerned changes in the material structure and strength properties. The roughness expected from this application is finer than that produced by the technologies currently used. Although this requires post-machining, it can also significantly reduce the amount of material, lead times and therefore costs.

There is scope for further improvements in the mechanical properties of printed parts and the repeatability of their dimensions.

Acknowledgements

The authors express their gratitude to Tamás Zsebe and Dávid Csonka for their help in the production of the sample printed shown in Figure 8.

References

- [1] Abir Bouhamed, Jamel Mars, Hanen Jrad, Mondher Wali and Fakhreddine Dammak (2021), “Experimental and numerical methodology to characterize 5083-aluminium behavior considering non-associated plasticity model coupled with isotropic ductile damage.” *International Journal of Solids and Structures* 229.
- [2] Alexander Arbogast, Sougata Roy, Andrzej Nycz, Mark W. Noakes, Christopher Masuo, and Sudarsanam Suresh Babu (2020), “Investigating the Linear Thermal Expansion of Additively Manufactured Multi-Material Joining between Invar and Steel.” *Materials* 13, no. 5683.
- [3] Ange Lu, Yan Gao, Tan Jin, Xichun Luo, Quanren Zeng and Zhentao Shang (2020), “Effects of surface roughness and texture on the bacterial adhesion on the bearing surface of bio-ceramic joint implants: An in vitro study.” *Ceramics International* 46, no. 5, 6550-6559.
- [4] C. Buchanan and L. Gardner(2019), “Metal 3D printing in construction: A review of methods, research, applications, opportunities and challenges.” *Engineering Structures* 180: 332-348.
- [5] Çam Gürel (2022), “Prospects of producing aluminum parts by wire arc additive manufacturing (WAAM).” *Materials Today: Proceedings* 62, no. 1, 77-85.
- [6] Chuanchu Su, Xizhang Chen, Chuang Gao and Yangfan Wang (2019), “Effect of heat input on microstructure and mechanical properties of Al-Mg alloys

- fabricated by WAAM.” *Applied Surface Science* 486, no. <https://doi.org/10.1016/j.apsusc.2019.04.255>: 431-440.
- [7] David E. Cooper, Mark Stanford, Kevin A.Kibble and Gregory J.Gibbons (2012), “Additive Manufacturing for product improvement at Red Bull Technology.” *Materials & Design* 41, 226-230.
- [8] Dirk Herzog, Vanessa Seyda, Eric Wycisk and Claus Emmelmann (2016), “Additive manufacturing of metals.” *Acta Materialia* 117, 371-392.
- [9] F. Martina, J. Mehnen, S.W. Williams, P. Colegrove and F. Wang (2012), “Investigation of the benefits of plasma deposition for the additive layer manufacture of Ti–6Al–4V.” *Journal of Materials Processing Technology* 212, no. 06, 1377-1386.
- [10] Furukawa K. (2006), “New CMT arc welding process – welding of steel to aluminium dissimilar metals and welding of superthin aluminium sheets.” *Welding International* 20, no. 6, 440–445.
- [11] Gyula Ferenc Vasvári, Dávid Csonka, Tamás Zsebe, Ádám Schiffer, Ivan Samardžić, Roland Told, Attila Péntek and Péter Maróti (2021), “CMT Additive Manufacturing Parameters Defining Aluminium Alloy Object Geometry and Mechanical Properties.” *Materials* 14, no. <https://doi.org/10.3390/ma14061545>.
- [12] Heralic Almir, Monitoring and control of robotized laser metalwire deposition. Chalmers University of Technology, 2012.
- [13] Iván Tabernero, Amagoia Paskual, Pedro Álvarez, Alfredo S uárez (2018), “Study on Arc Welding Processes for High Deposition Rate Additive Manufacturing.” *Procedia CIRP* 68, 358-362.
- [14] Johnnie Liew Zhong Li, Mohd Rizal Alkahari†, Nor Ana Binti Rosli, Rafidah Hasan, Mohd Nizam Sudin, and Faiz Redza Ramli (2019), “Review of Wire Arc Additive Manufacturing for 3D Metal Printing.” *International Journal of Automation Technology* 13, 346-353.
- [15] Julián Israel Aguilar-Duque, Jorge Luis García-Alcaraz and Juan Luis Hernández-Arellan (2020), “Geometric considerations for the 3D printing of components using fused filament fabrication.” *The International Journal of Advanced Manufacturing Technology* 109, 171–186.
- [16] J. Martikainen, P. Kah and R. Suoranta (2013), “Advanced gas metal arc welding processes.” *The International Journal of Advanced Manufacturing Technology* 67, 655–674.
- [17] Robert A. Hafley, Karen M. B. Taminger and R. Keith Bird (2007), “Electron Beam Freeform Fabrication in the Space Environment.” *AIAA Aerospace Sciences Meeting and Exhibit* 1154.
- [18] Roy D. Crowninshield, Jack D. Jennings, Michel L. Laurent and William J. Maloney (1998), “Cemented Femoral Componeint Surface Finish Mechanics.” *CLINICAL ORTHOPAEDICS AND RELATED RESEARCH* 355, 90-102.
- [19] S. Selvia, A. Vishvakshana and E. Rajasekar(2018), “Cold metal transfer (CMT) technology - An overview.” *Defence Technology* 14, 28-44.

- [20] Simon Ford and Mélanie Despeisse (2016), “Additive manufacturing and sustainability: an exploratory study of the advantages and challenges.” *Journal of Cleaner Production* 137, 1573-1587.
- [21] Stephen Mellor, Liang Hao and David Zhang (2014), “Additive manufacturing: A framework for implementation.” *Int. J. Production Economics* 149, 194-201.
- [22] Yuehai Feng, Bin Zhan, Jie He and Kehong Wang (2018), “The double-wire feed and plasma arc additive manufacturing process for deposition in Cr-Ni stainless steel.” *Journal of Materials Processing Technology* 259, no. <https://doi.org/10.1016/j.jmatprotec.2018.04.040>, 206-215.
- [23] Zhai and Yuwei (2014), MICROSTRUCTURE EVOLUTION, STATIC AND DYNAMIC PROPERTIES, AND DAMAGE MECHANISMS IN Ti-6Al-4V FABRICATED BY ADDITIVE MANUFACTURING. WORCESTER POLYTECHNIC INSTITUTE.
- [24] Zhi-qiang Liu, Pei-lei Zhang , Shao-wei Li, Di Wu and Zhi-shui Yu (2020), “Wire and arc additive manufacturing of 4043 Al alloy using a cold metal transfer method.” *International Journal of Minerals, Metallurgy and Materials* 27, no. 6, 783-791.

Experimental investigation of proton exchange membrane fuel cells efficiency (PEM)

Ahssan M.A. ALSHIBIL^{1,2}, Kornél BESSENYEI¹, István PATAY¹

¹Institute of Technology, MATE, Gödöllő

²Department of Mechanical Engineering, College of Engineering,
University of Kufa, Iraq

Abstract

Experimental investigation supports the technical developer's improvements in fuel cell technology, which is essential because it does not use fossil fuels, FCs uses hydrogen extracted from water as a fuel. It's not needed for any mechanical moving parts, has low environmental effects, available fuel, and low noise pollution, so the fuel cells are useful technology. This paper focuses on fuel cells technology, and the main objectives of this work can be summarized as follows, to introduce fuel cell technology generally, give a theoretical description of fuel cells, to introduce the different types of fuel cells, test a typical PEM type of fuel cell and introducing the results and how efficiency increase. All the analyses in the test device were better at constant airspeed; in this manner, the efficiency will be better in similar circumstances.

Keywords

proton exchange membrane, fuel cells, electrical efficiency

1. Introduction

Energy is a big name extents in various forms like chemical, mechanical, thermal, solar, nuclear, electrical, optical, and renewable energy. Each of these types has distinct applications. Though the energy cannot be created or destroyed, one form can be transformed into another using effective modern techniques.

Electrical energy is the most important requirement for many of the techniques and facilities to conduct our lives. There are many successful methodologies to generate electric energy, which mainly depend on energy conversion from some other form into electrical energy, and the fuel cell (FC) is one of the predominant technologies to produce electricity. (EG&G Technical Services 2004)

But, in general, the fuel cells generate electric energy directly from some chemical reactions, which does not require any moving mechanical devices but in the presence of electrodes. The generated electricity has a higher frequency and lower environmental effect compared to those of the conventional methodologies. A fuel cell uses common fuels or hydrogen (H₂) or (H₂-rich) as a reductant in addition

to the ambient air O_2 as an oxidant inside the cell. Chemical reactions occur in the cell electrodes between the H_2 , and O_2 in the presence of other chemical ingredients to produce the DC electricity (Li and Sabir 2005).

Typically, a fuel cell does not require any dynamic mechanical components, possesses almost zero emission-based environmental effects, has a diversity of selecting a range of fuels to be used, and has less noise pollution. That is why fuel cells are helpful for clean energy production (Gamalath, Peiris, 2012).

Fuel cells have preserved a history of evolution since the early 19th century. Extensive research on fuel cells has been observed after about 150 years, i.e. in the later half of the twentieth century, with the introduction of a proton exchange membrane fuel cell by General Electric in the year 1950 (Barbir 2012). The research on fuel cell evolution excelled in later decades and is currently available as a commercial and residential energy-producing source. The chronological history of fuel cell-related invention and their evolution are briefly reviewed in the following sub-sections (Colleen Spiegel 2007).

The first unmistakable presentation of the fuel cell principle was performed by William Grove, a lawyer as well as a scientist, in 1839 by using hydrogen and oxygen (EG&G Technical Services 2004).

Among the successful demonstrations of the research works performed by various companies, the introduction of the PEM fuel cell power-driven bus by the Ballard power system and that of a passenger car by the Energy Partners, a successor of Perry Energy Systems, in 1993 are notable (Barbir 2012).

This paper focuses on fuel cells technology, and the main objectives of this work can be summarized as follows, to introduce fuel cell technology generally, give a theoretical description of fuel cells, to introduce the different types of fuel cells, test a typical PEM type of fuel cell and introducing the results and how efficiency increase.

2. Materials and methods

Polymer electrolyte membrane fuel cells (PEMFCs).

Due to their excellent proton conduction capacity, the electrolytes used in this fuel cell are the ion exchange membranes. Hence, the polymer electrolytes, also known as proton exchange membrane (PEM), used in the fuel cell render high-power density along with compacting the cell volume, reducing the overall expenditure and lowering the weight (Giorgi, Leccese, 2013). Thus, a general PEM fuel cell is composed of the anode (negatively charged), cathode (positively charged), and membrane-based electrolytes, as shown in Fig. 1.

Test laboratory device

The device is a laboratory device made by Heliocentris, energy solutions company. The name of this device is Hy-Expert Instructor fuel cell system includes essential components necessary to perform experiments. The components of the laboratory device are shown in Figs. 2-3. (Heliocentris 2005):

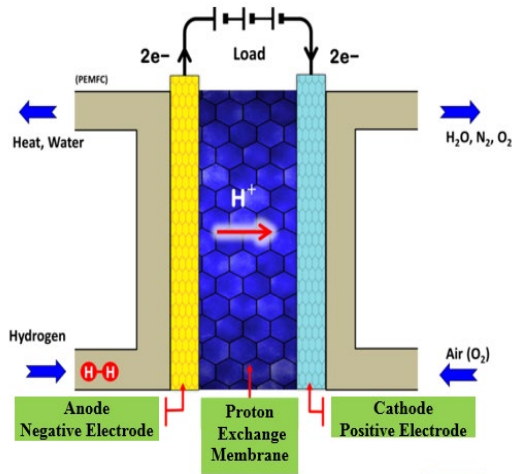


Figure 1. The polymer electrolyte fuel cell (PEMFC) (Colleen Spiegel 2007)

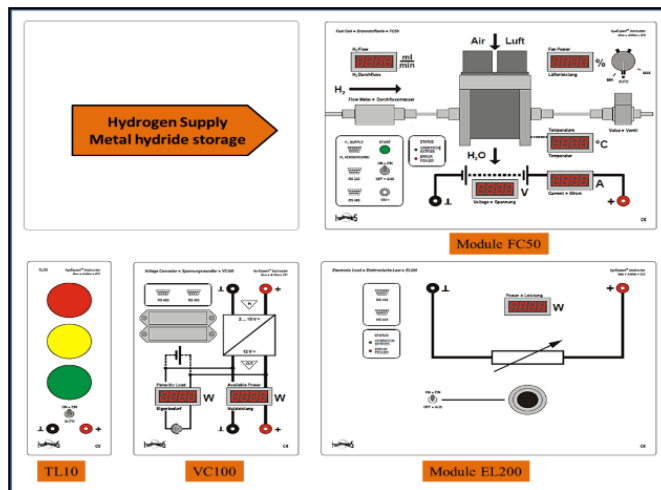


Figure 2. Hy- Expert™ Instructor fuel cell system

At first, the laboratory was prepared to suit the design conditions of the test device providing adequate laboratory area; the place should be provided with fresh air and apply the safety measures necessary to conduct experiments. The second thing is installed all main five parts that have been explained in the previous section; the most important parts are (FC50) and (EL200), where all experiments in this chapter have been done using these two parts of Hy- Expert™ Instructor fuel cell system (Heliocentris 2005). The main steps in the laboratory are:

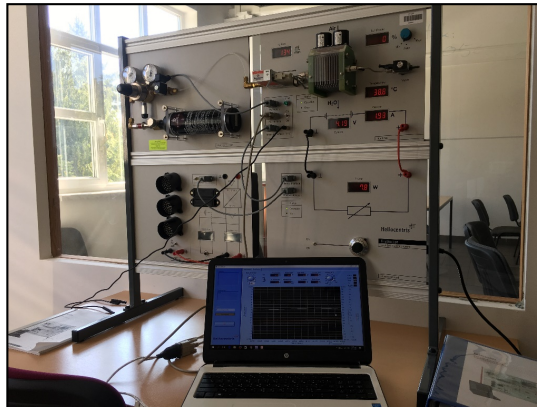


Figure 3. Hy- Expert™ Instructor fuel cell system

1. Turn on module FC50 without load (i.e., Without running EL200) and wait 10 to 30 second till the H₂ pass through the pipes.

2. Heating-up the system (i.e., Cells stack) till the operation temperature of fuel cells, which is (40 °C) because it's an adequate degree to take the results from the test device. To do this, turn on the electrical load (EL200) by increasing the variable load using a potentiometer then the temperature will increase gradually from approximately (19.5 °C). The device will turn off automatically if the temperature reaches 50 °C.

3. After reaching (40 °C) the operating temperature of PEM fuel cells, set the load in EL200 to zero.

4. Increase the load step by step using a potentiometer in EL200 and take a result.

3. Results and discussion

This chapter presents the results that are obtained from the test device and discusses these results. The graphics here are painted in MATLAB programs.

As explained in the previous section, the steps were repeated in three cases depending on the fan's speed of FC50 and the result taken when:

Fans speed set "AUTO". The fan speed is set automatically according to the stack power output so that adequate cooling is always ensured.

Fans speed set "0 %".

Fans speed set "5%" with a constant flow of air.

Depending on the results obtained it can be painted the voltage-current relation and depict the characteristic curve; Fig.4. illustrates the Voltage-Current curve.

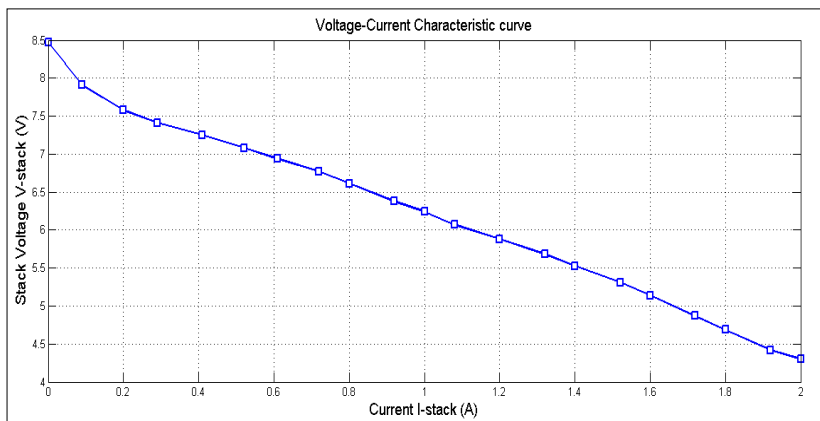


Figure 4. Voltage-Current Characteristic curve

Voltage drop amid the present increments and bend of the fuel cell demonstrates an exponential connection between 0 A and 0.61 A. As the current rises, the current and voltage relationship becomes linear.

The Power-Current curve can be drawn depending on experimental results. Fig.5 illustrates the (P-I) curve.

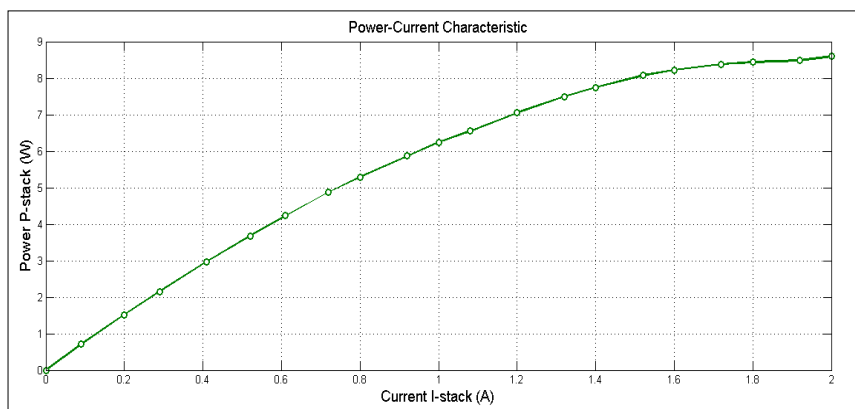


Figure 5. Power-Current Characteristic

Fig.6 illustrates the relationship between the hydrogen flow rate and stack current of fuel cells.

With elevation and current, the hydrogen demand of the fuel cell increases in the same proportionality; Fig. 5. shows the linear process of the measured curve. The efficiency of the fuel cell stack at an AUTO setting of the fan. By analyzing the power efficiency characteristic, you will gain important knowledge about sizing a fuel cell. Fig. 6. illustrates the Efficiency-Power comparison.

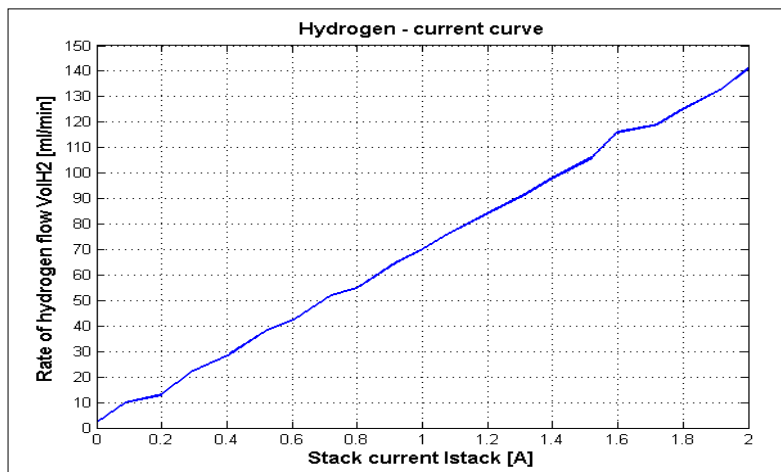


Figure 6. Hydrogen flow rate- current curve

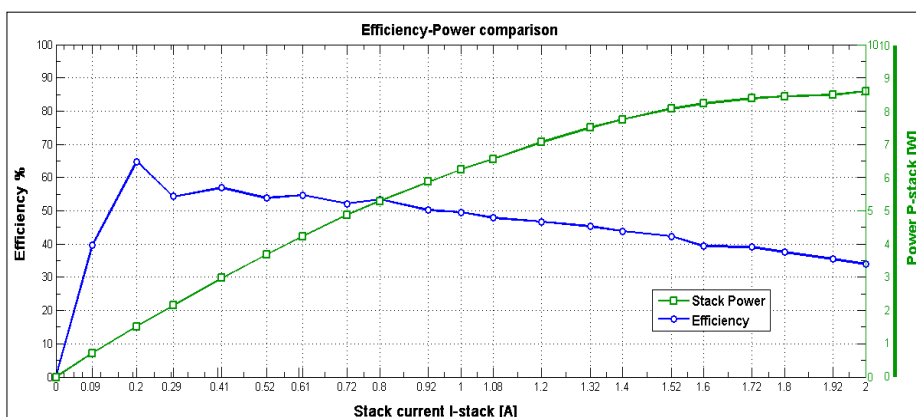


Figure 6. Efficiency-Power comparison

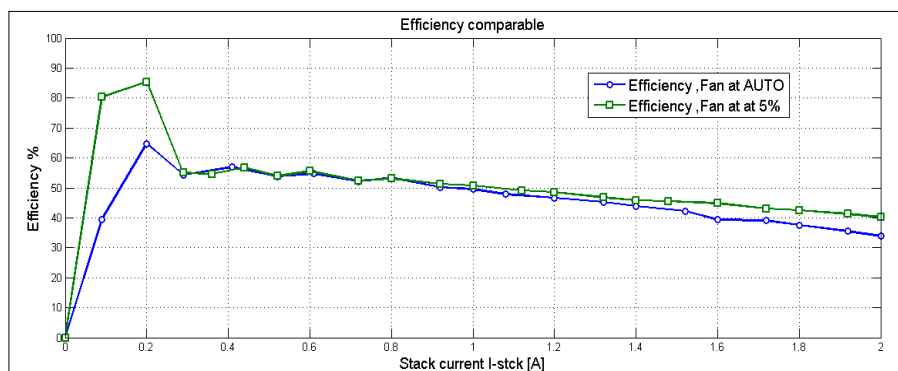


Figure 8. Efficiency comparable at AUTO and 5%

The power stack conveyed by the stack ascends over the whole range, while the stack efficiency is most noteworthy at low currents. The efficiency bends back off after 0.2. The stack current, and the power bend emerges in light of the corresponding connection between power and current.

The efficiency is better when the airflow speed is constant, even at the end of this process. Fig.8. illustrates the comparable faces.

Conclusions

Proceeding with this research of testing a typical PEM-type fuel cell and introducing the results and how can increase its efficiency. After conducting tests on this type of fuel cell and using MATLAB to draw the characteristic curves. With increasing the request of load, fuel cell voltage starts downward because of the inverse relationship between voltage and current as indicated by Ohm's Law but the power increase because of increased current.

Amid working experiments on the test device was found the airflow in a constant rate was superior to "AUTO" – in the auto setting, the fan was in high ventilation-To create the electricity, the membrane must be in a wet situation, this indicates the fuel cells deliver water in the typical way that is critical for the electrochemical reactions which are responsible for delivering electricity, if the airflow is fast subsequently the system will be dry then influenced on the fuel cell interactions, then the voltage and power of the system will be lower.

The efficiency rises steeply from the zero point, rapidly drawing nearer the cut-off estimation of 0.2A stack current. The power conveyed by the stack ascends over the whole range while the stack efficiency is maximized at low currents. The ideal efficiency of a fuel cell happens in the low-load range. However, the ideal conveyed power happens in the highest or greatest current range, subsequently relying upon the application you need to pick whether the energy unit will work with the greatest efficiency or with maximum power. With ideal efficiency, the supplied fuel is ideally changed over into electricity. However, the fuel cell has a higher, most extreme power than might be utilized. Subsequently, bigger weight and volume result, and more noteworthy costs. Such efficiency concerns are significant just for stationary applications, for which weight and size are not important and which work for quite a while with consistent load, e.g., energy production in a power station. Besides, the fuel cell, relying upon all the analyses in the test device, was better at constant airspeed; in this manner, the efficiency will be better in a similar circumstance.

Acknowledgements

This work was supported by the Stipendium Hungaricum, Hungarian university of agriculture and life sciences, Gödöllő, Hungary.

References

- [1] Barbir F. (2012): PEM fuel cells: theory and practice, 2nd ed. Elsevier Inc., Academic Press.
- [2] Colleen Spiegel (2007): Designing and Building Fuel Cells. McGraw-Hill Higher Education.
- [3] EG&G Technical Services I. (2004): Fuel Cell Handbook, 7th ed, U.S. Department of Energy National Energy Technology Laboratory.
- [4] Gamalath K.A.I.L.W., Peiris B.M.P. (2012): Theoretical Approach to the Physics of Fuel Cells. *Int. Lett. Chem. Phys. Astron.* 2, pp. 15–27.
- [5] Giorgi L., Leccese F. (2013): Fuel Cells: Technologies and Applications. *Open Fuel Cells J.* 6, pp. 1–20.
- [6] Heliocentris, (2005): Experiments guide and components description for the Hy-Expert™ Instructor Fuel Cell System. Heliocentris Energiesysteme.
- [7] Li X., Sabir I., (2005): Review of bipolar plates in PEM fuel cells: Flow-field designs. *Int. J. Hydrogen Energy* 30, pp. 359–371.

Soot accumulation in the diesel particulate filter and its effect on the filtration efficiency

Dániel SZÖLLŐSI^{1,2}, Péter KISS³

¹Exhaust System Evaluation, IBIDEN Hungary Technical Center,
IBIDEN Hungary Kft., Dunavarsány

²Doctoral School of Mechanical Engineering, MATE, Gödöllő

³Department of Vehicle Technology, Institute of Technology, MATE, Gödöllő

Abstract

Despite its many advantages, there are several disadvantages of diesel technology. Like most fossil fuels, diesel fuel has carbon and hydrogen as essential components. At an ideal thermodynamic equilibrium, only carbon dioxide (CO₂) and water vapor (H₂O) would be formed in the diesel engine. However, due to this air-fuel ratio, combustion temperature, ignition timing, turbulences in the combustion chamber, etc., significantly more harmful substances are formed. The most significant of these are carbon monoxide (CO), hydrocarbon (HC), nitrogen oxide (NO_x) and particulate matter (PM) emissions, as well as sulphur dioxide (SO₂) (Figure 1.) (Prasad and Bella 2010).

Keywords

filtration efficiency, diesel particulate filter, smoke meter, filter smoke number (FSN)

1. Introduction

Diesel engine emission

CO is the result of imperfect combustion, in diesel engines with a large excess of air, its formation is minimal. It is a colorless and odorless gas, binding to hemoglobin - which is responsible for transporting oxygen to the blood - an order of magnitude better than oxygen. Because of this, it causes concentration disorders, slowed reflexes and confusion (Asphyxiation), and ultimately causes death.

HC emissions are due to unburned fuel. It is formed in the lower temperature parts of the combustion chamber, as a result of insufficiently high temperatures. The composition of the exhaust gas hydrocarbon can depend on many engine factors, the emission of which is very diverse, ranging from alkanes, alkenes to various aromatic compounds. It contributes to an increase in the concentration of ground-level ozone, which can cause long-term mental problems in children.

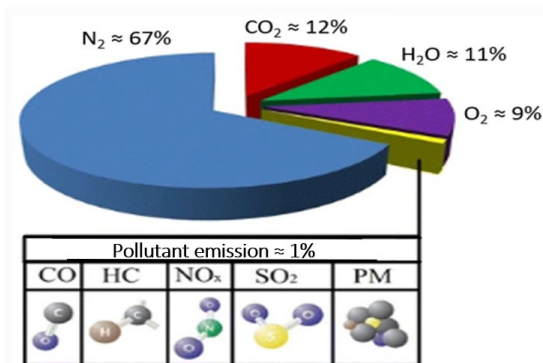


Figure 1. Raw emission of the diesel engine (Kair and Majewski 2006)

As a result of combustion, particulate matter (PM) from diesel engines is also significant. They are formed by agglomeration of various particles:

- carbon,
- partially burnt fuel,
- partially burnt lubricating oil,
- ash from fuel and lubricating oil,
- sulphates,
- water,
- metal particles (Agarwal 2007).

Thanks to the many components, the particles are very complex. The materials listed above are usually adsorbed onto a central carbon core to create agglomerates typically 15-40 nm in size, approximately 90% of which are smaller than 1 μm (Burtscher 2005). If we want to express it in particles, the diesel engine emits 10¹⁴ particles, which is 3 orders of magnitude higher than the particle emission of a gasoline engine. These harmful emissions can cause lung and respiratory problems and, according to the current state of science, can greatly contribute to the development of cancers (MECA 2007).

Normally, during combustion, nitrogen in the air does not react with oxygen. However, as a result of the inhomogeneous combustion characteristic of diesel engines, with a starting temperature of 1600 °C, nitrogen already reacts with oxygen and creates NO_x emissions.

The two main components of NO_x emissions are the NO and NO₂. The significantly more toxic NO is slowly converted to NO₂ under normal atmospheric conditions. Road traffic causes 40-70% of anthropogenic NO_x emissions, and approximately 85% of that can be attributed to diesel vehicles (Lee et al. 2013). Nitrogen oxides also promote the formation of acid rain and smog.

Several exhaust gas treatment companies have made significant efforts to reduce these atmospheric pollutants. In connection with their results, various cost-effective technologies were born and proved that they can significantly reduce

these harmful emissions, all without having to reduce the performance of the vehicle.

In response to health concerns, more and more stringent emission standards have been introduced for new diesel engines worldwide. Current emission regulations are forcing continuous improvements and a systematic approach, where advanced engine management must be used and combined with various sophisticated exhaust gas aftertreatment technologies.

Emission aftertreatment

Nowdays, there are several well-functioning exhaust gas treatment technologies for diesel engines. The most significant are the following:

PM reduction technologies:

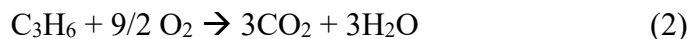
- diesel oxidation catalyst (DOC),
- diesel particulate filter (DPF),
- closed crankcase ventilation (CCV).

NO_x emission control technologies:

- exhaust gas recirculation (EGR),
- selective catalytic reduction (SCR),
- NO_x catalyst (LNC),
- NO_x trap (LNT).

Oxidation catalysts, which were also responsible for the oxidation of hydrocarbons and CO in early gasoline engines, continue to play an important role in diesel engines as well. Although they were originally developed to reduce gas emissions, they have proven their effectiveness in reducing particle emissions as well, which can reach up to 20-50% (total particle weight) (MECA 2007).

The oxidation processes are the followings (Kalló 2000):

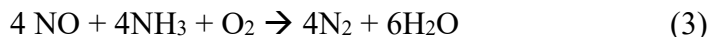


Diesel particulate filters are also a proven technology. They have a honeycomb structure, the cell is always closed on the opposite side. Filtration thus takes place through the pores of the cell walls. The two most common raw materials for the ceramic body of the particle filter are Cordierite (2MgO–2Al₂O₃–5SiO₂) and silicon carbide (SiC). Cordierite filters are significantly cheaper due to their production technology, in addition to their very good particle filtering properties. This is also true for SiC filters, but this technology requires an investment, which is compensated by the fact that it is significantly more robust and can withstand more extreme engine conditions. Today's modern particulate filters, whether Cordierite or SiC, can filter out 99.9% of engine particulate emissions.

Because of its smog and ozone-forming properties, NO_x has become the primary target of efforts to reduce emissions. Exhaust gas recirculation (EGR) was

used to reduce this and can reduce the nitrogen oxide content of the exhaust gas by up to 50%.

It can remove nitrogen oxides even more efficiently during selective catalytic reduction (SCR) with the addition of urea. During this process, in addition to NO_x removal (up to 75-90% efficiency) (Bíró 2020), a significant 80% reduction in hydrocarbon emissions can be achieved and solid particles can also be reduced by an additional 20-30%. The main reactions are the following (MECA 2007, Kalló 2000).



In order to achieve the current emission limit values, car manufacturing companies often use the main technologies listed here in combination. Moreover, together with additional engine control strategies, they develop their own complete emission system.

2. Experimental

Exhaust Particulate matter (PM) measurements

As emission regulations emerged, so did the need for equipment that could measure particulate matter (PM) emitted by engines in a repeatable and comparable way around the world. With the exception of condensed water, all particles fall into the category of "PM", which is maintained at a regulated temperature of 51.7 °C or less on a filter of the same size and material.

The only officially approved measurement method for measuring diesel vehicles is a gravimetric method, where the total weight of PM is measured. A constant volume sampling system must be used, where the size of the system depends on the exhaust gas flow rate. Therefore, a separate system must be built for each engine (an average passenger car may require a system of up to 10 m), which is why it is very space-consuming and cumbersome to use.

Another method (opacity-based smoke meter) uses a light source and measures the light transmittance of the exhaust gas. Here, the clean air and the exhaust gas of the given sample are compared and a % value is obtained as a result.

In Japan, the filter-type smoke measuring device has been adapted as an official method. During the measurement, a certain amount of exhaust gas flows through a filter paper and the degree of contamination is measured. The percentage value is obtained by comparing the light reflectance of an uncontaminated and contaminated paper. This measurement method was used during the execution of the measurement (Ohno 2006).

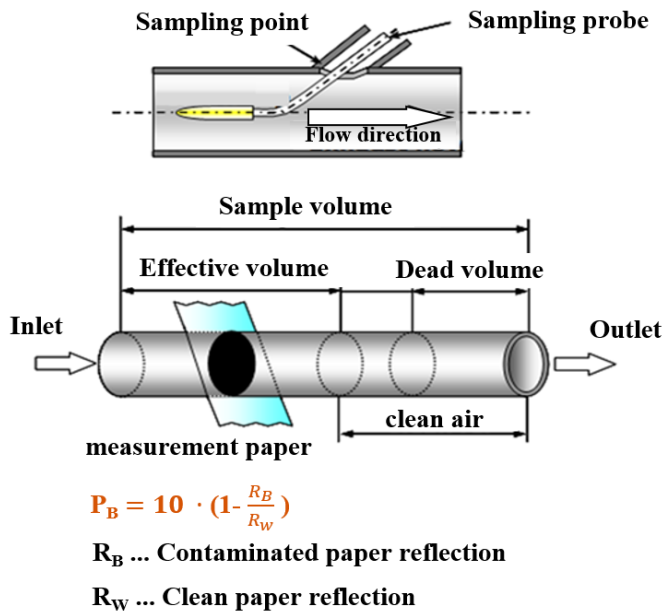


Figure 2. Smoke meter measurement scheme

The filtration efficiency is influenced by many aspects. During its lifetime, the filtration efficiency can increase or decrease, while the efficiency of an unused new DPF is quite low. The latter can be clearly established from Figure 3 (Ohno 2006).

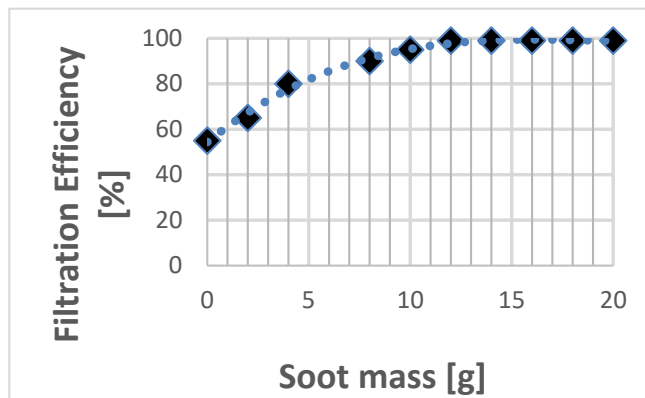


Figure 3. Correlations between soot mass and filtration efficiency

In order to be able to compare the result with other DPF, we remove the remains of carbon containing deposits from the filter. To achieve this, we use high-temperature oxidation, which is carried out in a dewax oven.

Test equipment

The exhaust gas treatment system is tested under laboratory conditions in the engine test cell. The main units located in the room:

- the exhaust gas treatment system, and the diesel engine connected to it,
- DPF filtration efficiency measuring equipment (AVL 415S), two measurement probes installed before and after DPF (Figure 4),
- gas concentration measuring equipment.

The AVL LD (Light Duty) 220 kW brake bench was fitted with a PSA DW10c type, EURO 5 compliant 2.0 HDi engine. The exhaust side equipped with the exhaust gas treatment system widely used by the PSA group for these passenger car engines, including the sample DPF (already dewaxed) to be tested.

The main task of engines equipped with exhaust gas aftertreatment systems is to achieve reliable, reproducible results at the exhaust gas sampling point, despite the high pressure and temperature. Engines emit barely detectable amounts of soot after the diesel particulate filter (DPF) system, which requires very low detection limits and high accuracy for soot measurement equipment.



Figure 4. Smoke Meter (AVL 415S)

The AVL smoke meter determines the smoke number of the DPF (according to ISO 10054) and the soot concentration in mg/m^3 using the method of testing the coloration of the filter paper using an opacimeter. Variable sampling volume and heat conditioning of the exhaust gas ensure extremely high reproducibility and a wide range of applications. The instrument can be used to measure the emissions of large truck engines and small engines installed in passenger cars. The main areas of application are combustion optimization in prototype engines, emission control up to and after the start of series production. In addition, it is also possible to measure the soot concentration in the untreated exhaust gas.

Test method

In order to guarantee the longevity of the motor connected to the brake pad, a gentle/low-load condition was introduced before each test until the motor was at operating temperature.

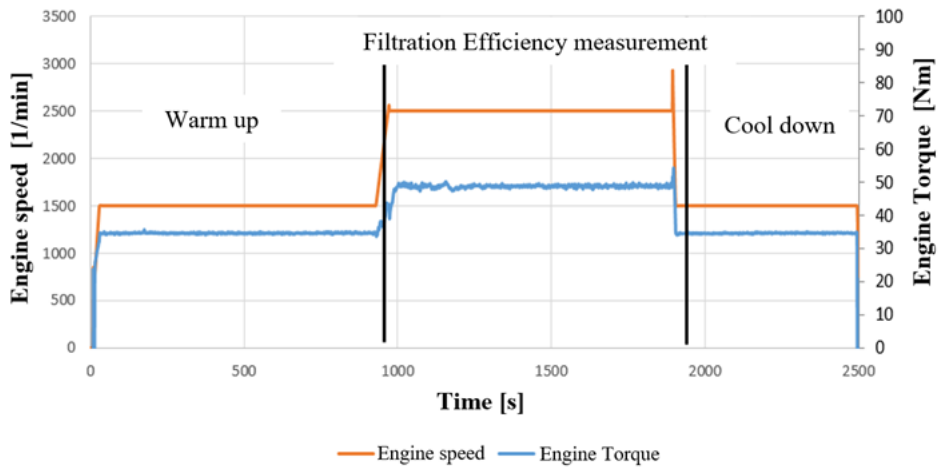


Figure 5. Engine conditions used during the soot filtration efficiency test

Then, considering the characteristics of the given engine, a medium-load stage follows. This condition is designed so that the smoke number (FSN) measured in the untreated exhaust gas is between 0.5 and 2.5, thereby guaranteeing reproducibility. Before starting the measurement, the amount of exhaust gas to be measured must be selected, as well as the measurement probes from which the sampling should take place.

The measurement consists of testing the discoloration of 3 pieces of white sample paper per measurement probe.



Figure 6. Sample paper feeder unit of AVL Smoke measuring equipment

A built-in opacimeter converts the discoloration into the so-called unitless filter smoke number (FSN). From the average of the 3-3 measurements, it determines the FSN taken from the untreated exhaust gas before the DPF and from the cleaned exhaust gas after the DPF.

After the measurement, the cooling cycle of the engine at operating temperature begins (Figure 5).

3. Results and discussion

During the evaluation of the measurement, we compare the ratio of the smoke number of the untreated (1,074 [FSN]) and the cleaned exhaust (0,008 [FSN]) gas after the DPF, and then the final filtration efficiency of the DPF filter can be determined expressed as a percentage. In this case, the diesel particulate filter cleaned the exhaust gas of approximately 99% of the soot particles. During the test, 10 g of soot was deposited.

Conclusions

It can be concluded that even with a new (unused) DPF filter, close to 100% filtration efficiency is available. The advantages of the filtration efficiency test determined on the basis of the smoke number include reproducibility, low time and cost.

In the future, it can be recommended to use soot burning in all cases before performing a soot filtration efficiency test, because as shown in Figure 3 above 10 g of soot deposition, the result approaches 100% regardless of the type of DPF, thereby eliminating the possibility of comparison.

Acknowledgements

Supported by the KDP-2021 Program of the Ministry for Innovation and Technology from the source of the National Research, Development and Innovation Fund.

References

- [1] Jánosi L. and P. Kiss (1988) Belsőégésű motorok nitrogénoxid kibocsátásának követése más motorjellemzőkből, Agrár-Műszaki Bizottság kutatási és fejlesztési tanácskozás Gödöllő, MÉM Műszaki Intézet, 34-36.
- [2] Ohno K. (2006) A Study on Performance of Particulate Filters Using R-SiC Porous Materials for Diesel Vehicles
- [3] Biró N. (2020) Egyedi Adblue befecskendező rendszer tervezése és tesztelése, Master's Thesis, Szent István University
- [4] Manufacturers of Emission Controls Association (MECA) (2007) Emission Control Technologies for Diesel-Powered Vehicles
- [5] Prasad R, VR. Bella (2011) A review on diesel soot emission, its effect and control, Bulletin of Chemical Reaction Engineering & Catalysis vol. 5, 69–86.
- [6] Khair MK. and WA Majewski (2006) Diesel emissions and their control. SAE International
- [7] Agarwal AK. (2007) Biofuels (alcohols and biodiesel) applications as fuels for internal combustion engines. Progress in Energy and Combustion Science vol. 33, 233–271.
- [8] Burtscher H. (2005) Physical characterization of particulate emissions from diesel engines: a review. Journal of Aerosol Science vol. 36, 896–932.
- [9] Lee T, J. Park, S. Kwon, J. Lee, J. Kim (2013) Variability in operation based NO_x emission factors with different test routes and its effects on the real-driving emissions of light diesel vehicles, The Science of the Total Environment, 461–462:377–385.
- [10] Kalló D. (2000) Katalitikus eljárások a környezetvédelemben, University of Veszprém

Investigate the effects of the generative design method on the multirotor structure

Ahmad DUGHMI, László KÁTAI

Institute of Technology, Hungarian University of Agriculture
and Life Sciences MATE,
Gödöllő

Abstract

The generative design method is a new technique used to explore new designs by using software algorithms, to use this should be a space design which means the area where the software will apply its algorithms to create the new designs, this area is created by boundary conditions such as main dimensions, forces, material, manufacturing method, and any other boundary condition could add it to the space design, in this paper will create a traditional design of multirotor structure (frame) then will apply the generative design method on this structure to compare the results of new designs with traditional one.

The aim of this paper study the effect of the method when taking the traditional design as co-design or Genotype (base form) for the generative design method, the method applies as a percentage of the traditional design, first will generate 40% of traditional design then 55% and 80%, so the method will take the traditional design as co-design and then will select some parts of traditional to generate by GDM to explore the new designs, for example in the first case will generate 40% of traditional design and keep 60% of traditional with no changes during the process.

We chose the multirotor structure because it was widely used in the last years and the biggest problem with it is the flight duration which has an inverse relation with weight, so will comparison the traditional design and generated designs in mass, stress, displacement, and factor of safety.

Keywords

Generative design, traditional design, CAD, multirotor

1. Introduction

Multirotor: A multirotor or multi-copter is a rotorcraft with more than two lift-generating rotors, the most common multirotor is a quadcopter, it is a simple multirotor that contains four arms connected to a rigid frame as shown in figure 1 (Mahony, Kumar, and Corke 2012).



Figure 1. Quadcopter developed by the author in MSc thesis.

One of the biggest problems of multirotor is flight duration, which has an inverse relation with weight and positive relation with battery capacities (Lee et al. 2020), so in this paper, a generative design method (GDM) will be introduced to study the effect of it on the multirotor structure and compare with a structure designed by the traditional way.

The most popular multirotor is Quadcopter, Quadcopters are vehicles with four rotors that can fly through the air. Controlling a quadcopter flight is not always simple. The quadcopter is a structurally straightforward but uncontrollable aerial vehicle, and even though its control systems are complicated, they have been researched and developed. Rotating two of the rotors clockwise and the other two counterclockwise is necessary. In recent years, the interest in these vehicles has overtaken that in manned aircraft. Compared to traditional helicopters, quadcopters have many benefits, some of these benefits: are low production costs, the ability to add features according to requirements, and the elimination of the risk of hazardous work environments for pilots, especially in many areas, including dangerous and dangerous areas where people cannot dissolve (Anon n.d.-b; Lee et al. 2020; Oktay and Köse 2019).

The formal definition of **Engineering design** can be found in Accreditation Board for Engineering and Technology (ABET) is the process of developing a system, component, or process to meet specified requirements. It is a decision-making process in which fundamental science, mathematics, and engineering are used to optimize the conversion of resources to accomplish a stated objective. Various realistic constraints must be considered, including economic concerns, safety, reliability, aesthetics, ethics, and social impact (ABET n.d.).

The systematic design process or the traditional method consists of a series of stages guided by a design model and a collection of design methods, which are tools and techniques that can be applied at various stages of the design process (Yousef Haik, Sangarappillai Sivaloganathan, and Tamer Shahin 2018).

The engineering process is not necessarily done in order. However, it is customary for engineers to describe the problem and discuss ideas before developing a prototype test, which is then adjusted and enhanced until the solution fulfills the

engineer's project's requirements. This is known as iteration, a standard working method (Lee and Ostwald 2022).

NASA has illustrated the Engineering Design Process as six steps to reach the design goal: ask, imagine, plan, create, experiment, and improve (NASA n.d.).

The general definition of **Computer-Aided Design (CAD)** is using computer software to assist during the design process, in which CAD involves any design activity such as initial design, development, analysis, or modification (K. Mallikarjuna Rao, K. Lalit Narayan, and MMM SARCAR 2008; Mikell P. Groover and Emory W. Zimmers 1984; Zhuming Bi and Xiaoqin Wang 2020).

Generative Design Method (GDM): The general definition of GDM is a modern technique used to explore a new design by using software algorithms. The GDM used in the early stage of the design process, the space design (boundary conditions) will be given by the designer as the primary dimension, size, force, weight, manufacturing method, a factor of safety,..etc. The design space will be the area for the software to think about how will create the model to get the goals of the design ., in other words, we defined the Generative design as a feature of CAD engineering software in which a designer interacts with artificial intelligence algorithms to produce and analyze hundreds of possible designs for a product concept. The generative design approach establishes the project's objectives and restrictions (Chien and Flemming n.d.; Junk and Burkart 2021; Khan and Awan 2018; Krish 2011).

Figure 2 illustrates the stages or components of the GDM, to apply or use GDM should follow these steps in the order (Krish 2011).

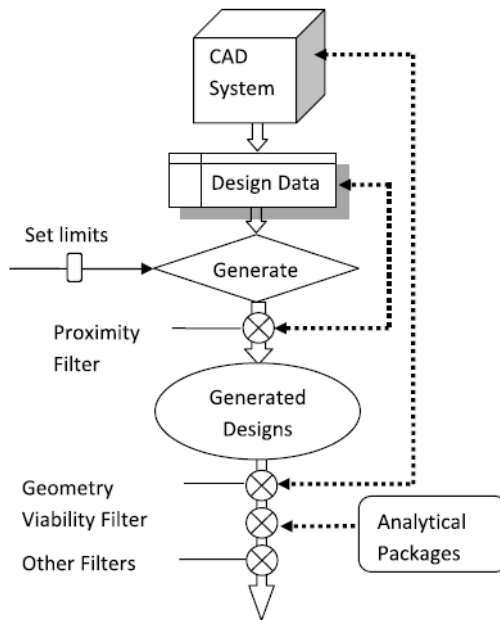


Figure 2. GDM step (Krish 2011)..

The first step is to choose a software support GDM such as Autodesk Fusion 360.

The second step defines the design data which means the boundary conditions to create the space design, each boundary condition set as fixed during the process or with limits, in this stage, the design is called genotype, the space design as you see in figure 3, the designer wants to create a chair, and one of the parameters used to create the design space is the main dimension, by using the main dimension, the system creates the design space which the area plotted with dashed lines, the algorithm will work in this area as you see in the figure by connected points together to create all possible designs (Buonamici et al. 2020).

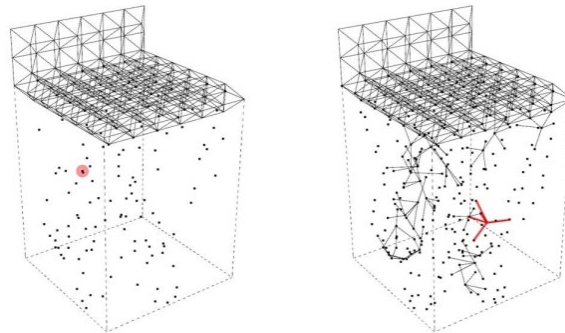


Figure 3. space design example (Buonamici et al. 2020).

In the third step, we will apply the GDM algorithms in the genotype design to explore the new designs in the space design.

In the fourth step after applying the algorithms, we need filters to delete the design which not applicable in the solution space as shown in figure 4, the performance envelope region is bigger than the viable space, which means the design space can provide inappropriate designs, so the filters delete them directly and keeps the designs in the viable space.

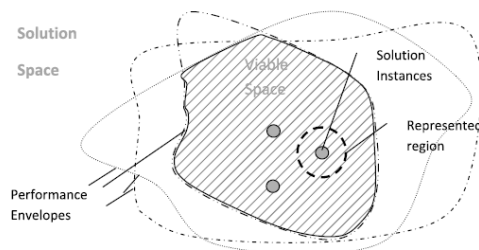


Figure 4. Solution space (Krish 2011).

Each small black circle is called a solution instance, and many are not as shown in the figure, and they can be applied to it with the established goals of the design,

all designs inside the represented region will be integrated from solution instances (Krish 2011).

In the fifth steps or last step, the software will provide the results in hundreds or thousands of designs, so in this stage, we need a filter to sort the results as the design goals, such as we can sort as the minimum mass or maximum stiffness, in this stage the design called the phenotype.

2. Materials and Methods

Boundary conditions:

1. **Main dimensions:** the main dimensions will be the same as the traditional design to generate designs because we will use the traditional design as a co-design or base form for generative design.
2. **Forces:** at the end of each arm will apply a 50N as a motor.
3. **Material:** Aluminum AISI10Mg, in the next table we mention only the important properties of the material which will use to calculate the factor of safety.

Yield strength	240 MPa
Ultimate tensile strength	460 MPa

4. **Min factor of safety** is set to 2 based on the federal aviation regulation set a limit of the factor of safety is 1.5 (Anon n.d.-a)
5. **Manufacturing method:** unrestricted and additive manufacturing method.

Traditional design: we designed the frame using the normal or traditional way of design, the design was created by Fusion 360 as shown in figure 5&6, the design is more complicated than usual because we will use it in the generative design as a co-design, we illustrate it later.

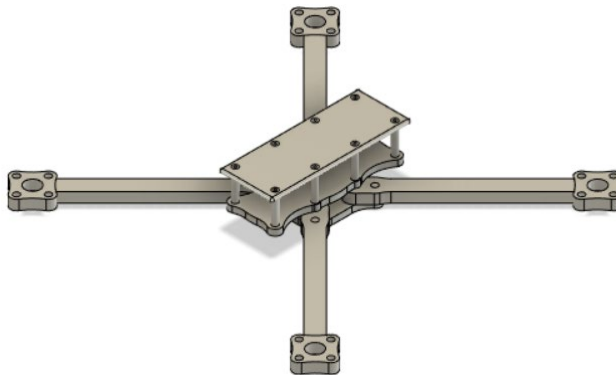


Figure 5. Traditional design.

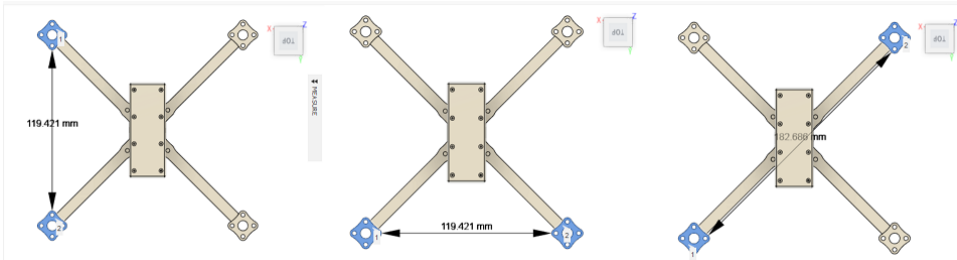


Figure 6. Main dimensions of traditional design.

Generative design

At the generative we will use the same boundary conditions which will use in traditional design during the analysis, as we mentioned in the introduction there are steps that should be followed to apply the GDM, the first step we chose Autodesk Fusion 360 as a CAD system and software support GDM, the second step create space design we will the boundary conditions which mentioned above to create the space design, but the base form of the design will be integrated from the traditional as cases:

Case 1: generating 40% of traditional design as shown in figure 7, in this case, will apply the method on the arms of the frame, the percentage 40% calculated from the mass, which is mean the arms make up 40% of the mass of the whole design, the green parts mean save this geometry during the process, red parts don't add materials in this parts, because of that I created big red parts around the frame to accelerate the process to start as a shape of quadcopter not rectangular then still improving the design to reach the quadcopter, the blue rows mean the forces applied.

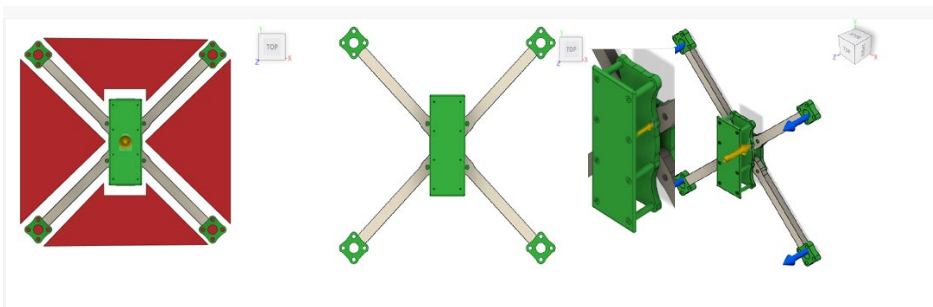


Figure 7. Case 1 generates 40% of traditional design.

Case 2: generating 55% of the traditional design, apply the GDM on the arms and a part of the center as shown in figure 8.

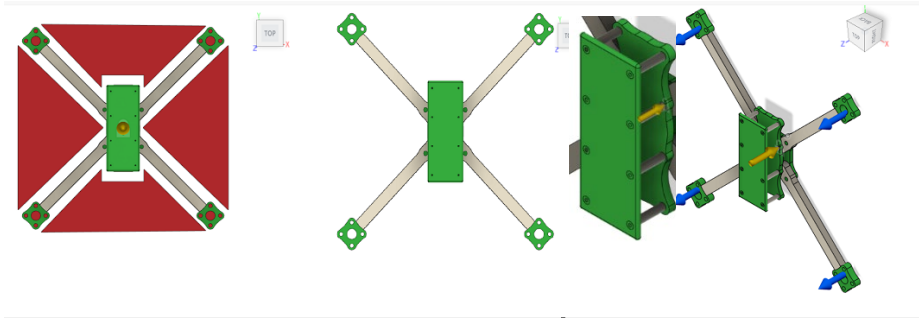


Figure 8. Case 2 generates 55% of traditional design.

Case 3: generating 80% of traditional design, in this case, we will save the geometry for the motor base only and then apply the method to the whole design as shown in figure 9.

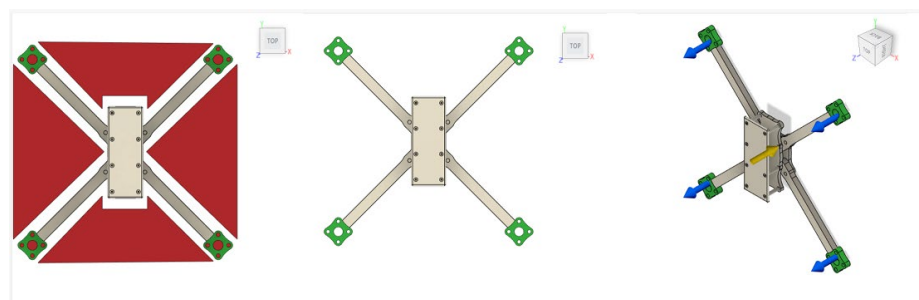


Figure 9. Case 3 generates 80% of traditional design.

The Manufacturing method is a boundary condition, in each case will apply the method with unrestricted the manufacturing method and apply it with additive manufacturing.

The results will be in hundreds of designs so we will apply the mass filter as an objective to our design and then take the lowest mass design for each case to make the comparison with traditional design.

3. Results and Conclusion

1. Traditional design: after applying the boundary condition on the traditional design we got these results in table 1.

Mass	105.557 g
Max Von misses stress	80 MPa
Max Displacement	0.806 mm
Min factor of safety	3.7

2. Generative design:

the results of GDM in hundreds of new designs for each case, this section will introduce the first case with unrestricted manufacturing method results as an example of the results, figure 10 shows selected designs during a change in the process.

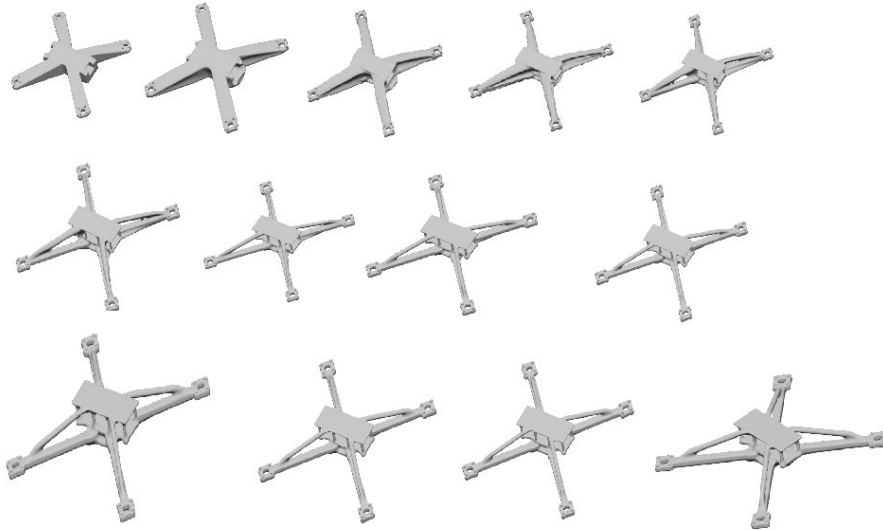


Figure 10. Case 1 unrestricted manufacturing method results.

Due to a large number of results, the software provides the results and sorts them automatically, the design selected for each case will be the lowest design mass among all results, table 2 provides the properties of each lowest design in each case.

Case/ manufacturing method	Mass (g)	Max von mises stress (MPa)	Max displacement (mm)	Min factor of safety
case 1 unrestricted manufacturing	92	8.487	0.041	28.279
case 1 additive manufacturing	92	11.809	0.067	20.323
case 2 unrestricted manufacturing	89	8.773	0.042	27.357
case 2 additive manufacturing	90	11.98	0.069	20.003
case 3 unrestricted manufacturing	32	67.519	0.882	3.5
case 3 additive manufacturing	33	96.963	1.487	2.47

3. Comparison between traditional design and generated designs

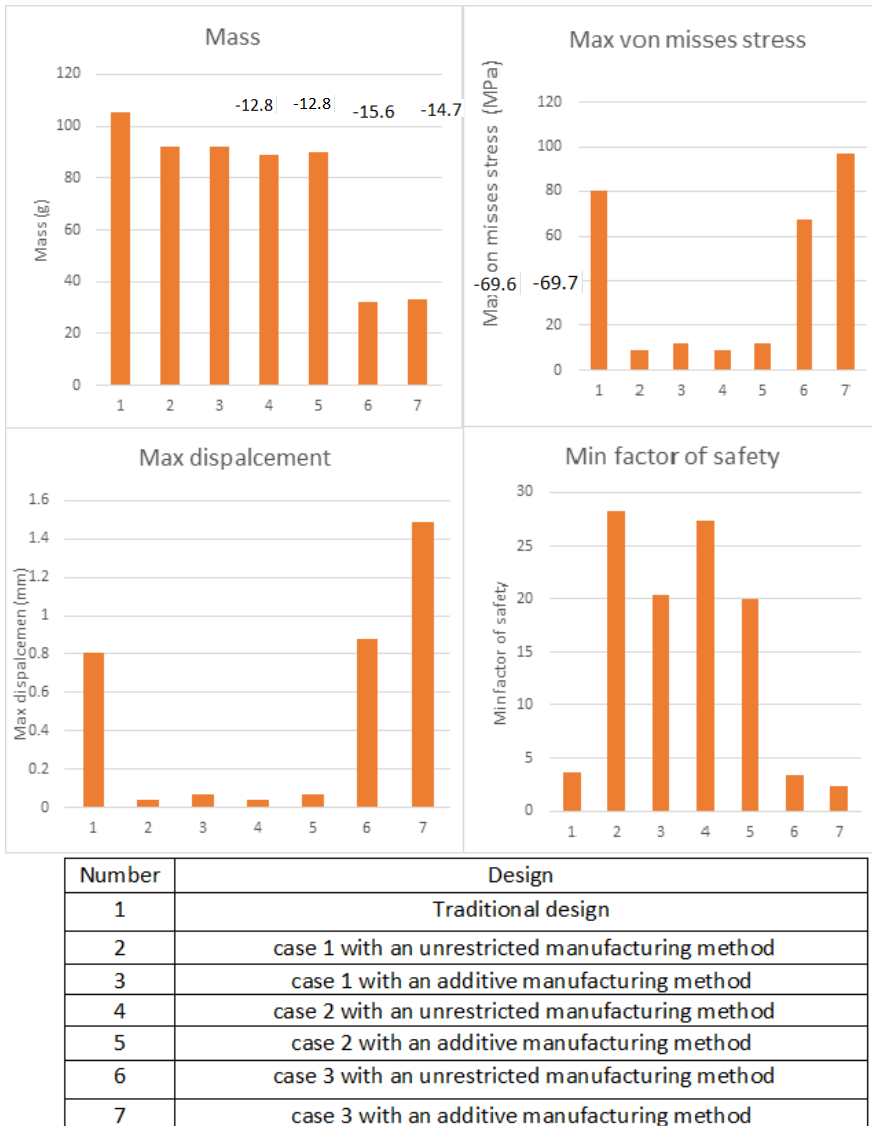


Figure 11. Comparison between traditional design and generated designs.

As it can be seen in the results all generated designs got less mass than traditional design, with the percentage of decrease for each case above the case column, case 3 shows a significant decrease in mass than other cases, so this decrease means reducing the restricted part of the design during the process (increase space design) will get more reduction in mass.

The maximum von mises stress got the highest in case 3 with additive manufacturing, but we can notice a significant decrease in cases 1 and 2 than traditional design, which means the GDM help to reduce the mass of the design and keep or improve the design to be more rigid as cases 1 and 2.

The maximum displacement as shown in the results got the highest in case 3 with additive manufacturing, we can notice a significant decrease in cases 1 and 2 than traditional design.

The minimum factor of safety means the lowest factor of safety found in the design after applying all boundary conditions, here we can notice a significant increase in cases 1 and 2 than in traditional design, in case 3 the result is closer to the traditional design.

In general, the GDM based on its own results can get a design with lower mass than a traditional one and reduce the stress and displacement on it with an increase in the factor of safety.

Acknowledgment

This research was supported by the Stipendium Hungaricum Programme and by the Mechanical Engineering Doctoral School, Hungarian university of agriculture and life science, Gödöllő, Hungary.

References

- [1] ABET. n.d. "Criteria for Accrediting Engineering Programs, 2019 – 2020."
- [2] Anon. n.d.-a. "14 CFR 25.303 (up to Date as of 9-28-2022)."
- [3] Anon. n.d.-b. *Modelling and Control of Quadcopter A?*
- [4] Buonamici, Francesco, Monica Carfagni, Rocco Furferi, Yary Volpe, and Lapo Governi. 2020. "Generative Design: An Explorative Study." *Computer-Aided Design and Applications* 18(1):144–55. doi: 10.14733/cadaps.2021.144-155.
- [5] Chien, Sheng-Fen, and Ulrich Flemming. n.d. *Design Space Navigation in Generative Design Systems*. Vol. 11.
- [6] Junk, Stefan, and Lukas Burkart. 2021. "Comparison of CAD Systems for Generative Design for Use with Additive Manufacturing." Pp. 577–82 in *Procedia CIRP*. Vol. 100. Elsevier B.V.
- [7] K. Mallikarjuna Rao, K. Lalit Narayan, and MMM SARCAR. 2008. *Computer Aided Design and Manufacturing*.
- [8] Khan, Shahroz, and Muhammad Junaid Awan. 2018. "A Generative Design Technique for Exploring Shape Variations." *Advanced Engineering Informatics* 38:712–24. doi: 10.1016/j.aei.2018.10.005.
- [9] Krish, Sivam. 2011. "A Practical Generative Design Method." *CAD Computer Aided Design* 43(1):88–100. doi: 10.1016/j.cad.2010.09.009.

- [10] Lee, Ju Hyun, and Michael J. Ostwald. 2022. “The Relationship between Divergent Thinking and Ideation in the Conceptual Design Process.” *Design Studies* 79. doi: 10.1016/j.destud.2022.101089.
- [11] Lee, Youngheon, Eu Tteum Park, Jinseok Jeong, Hayoung Shi, Jeong Kim, Beom Soo Kang, and Woojin Song. 2020. “Weight Optimization of Hydrogen Storage Vessels for Quadcopter UAV Using Genetic Algorithm.” *International Journal of Hydrogen Energy* 45(58):33939–47. doi: 10.1016/j.ijhydene.2020.09.014.
- [12] Mahony, Robert, Vijay Kumar, and Peter Corke. 2012. “Multirotor Aerial Vehicles: Modeling, Estimation, and Control of Quadrotor.” *IEEE Robotics and Automation Magazine* 19(3):20–32. doi: 10.1109/MRA.2012.2206474.
- [13] Mikell P.Groover, and Emory W.Zimmers. 1984. *CAD/CAM: Computer Aided Design and Manufacturing* .
- [14] NASA. n.d. “Engineering Design Process .”
- [15] Oktay, Tuğrul, and Oğuz Köse. 2019. “Farkli Uçuş Durumlari İçin Quadcopter Dinamik Modeli ve Simulasyonu.” *European Journal of Science and Technology* 132–42. doi: 10.31590/ejosat.507222.
- [16] Yousef Haik, Sangarappillai Sivaloganathan, and Tamer Shahin. 2018. *Engineering Design Process* . third edition.
- [17] Zhuming Bi, and Xiaoqin Wang. 2020. *Computer Aided Design and Manufacturing*.

Design and implementation of an object sorting robotic arm

Gergő BAGI, János TÓTH

Department of Mechatronics, Institute of Technology, MATE, Gödöllő

Abstract

This paper discusses a robotic arm that processes its environment with an optical sensor, which recognizes workpieces based on their color. The process of 3D printing, choosing the electronic components, and developing the operating software are all covered in the article. The robotic arm was produced using 3D printing, while the software was created using Python and the Arduino IDE. The robotic arm and its accessories easily meet such a criteria, that the machine would be able to take the place of human labor for straightforward sorting activities. The robotic system is designed to be easily improvable both in a handling and operational safety aspects.

Keywords

robotics, SCARA, 3D printing, Arduino, Python

1. Introduction

The sector of robotics is now expanding quickly. The emergence of the "future factory," or fully automated production that requires no human intervention beyond maintenance and where the end product of a production process can be more than just a product. The development of the "Internet of Things" and the practical implementation of Industry 4.0, are some of the reasons for this. For these enterprises, robots and robotic arms are necessary instruments. Although the automotive sector is a significant one, robots are also used in almost every other industry, including aerospace, healthcare, material handling, and entertainment. The demand for experienced employees to operate, maintain, and service these sorts of devices rises in direct proportion to the proliferation and expansion of robots and robotic arms. As robots may replace physical labor, there will be less need for human labor; this transformation will also have a big influence on the labor market. Pick-and-place material handling activities are one of the most frequent jobs carried out by tiny robots in industry. The control of a robotic arm that can carry out this task is the main focus of this paper. The SCARA (Selective Compliance Assembly Robot Arm), a robot arm (RTRR) with three rotary axes (rotating joint) and one linear axis (slide joint), is a good option among the ones already in use. Hiroshi Makino created this kind of robot in 1979 at Yamanashi University. (Gergely, 2009) (Miller, 1989)

2. Materials and methods

The used materials and methods will be discussed in this section.

Robotic arm selection and printing

At the beginning of the project, after defining the objective, the search for existing robotic arm design that could solve the problem had started. The most suitable robotic arm type was selected based on the following decision matrix shown in Table 1. The matrix resulted the SCARA type of robotic arm. The mechanical design of the robotic arm was not part of the set task, so already existing solutions were considered. Several solutions suitable for the task were found and the robot from howtomechatronics.com was chosen based on its ease of use. (Miller, 1989)

Table 1. Robot type selection matrix

	Articulate d robot	Spherical coordinate robot	Cylindrical coordinate robot	Delta robot	SCARA robot
Simple structure	1	4	4	2	4
Effector orientation management	1	1	5	5	5
Multifunctionalities	5	4	4	4	4
Simplicity of control	1	2	5	2	5
Industrial spread	5	2	2	4	5
Summary:	13	13	20	17	23

The 3D files downloaded from howtomechatronics.com were printed using FDM technology. This process is excellent for custom manufacturing, prototyping, and modelling. The printer that was used is a Creality Ender 3 Pro. For printing, PLA (PolyLactic Acid) and PLA+ materials were used, as they provide the best printing quality and are not prone to warping. They also have enough strength for this application. When printing PLA, all parts were made with a similar setup. The nozzle temperature was 210°C and the printing plate temperature was 60°C; the wall line count of these parts was 8, with a 20% cubic fill. A 0.4mm nozzle was used for printing. These settings were set in the program that generates the G-code, Ultimaker Cura (Figure 1.), and considered the need to generate the G-code with as little support as possible after placing the models on the table to avoid material waste. The robot base could not fit on the printing plate due to its dimensions. This difficulty was solved by a program called Netfabb (Figure 2.). In this program, 3D models can be sliced along the x, y, and z axes, and after slicing, it does not leave the model open, returning a solid body.

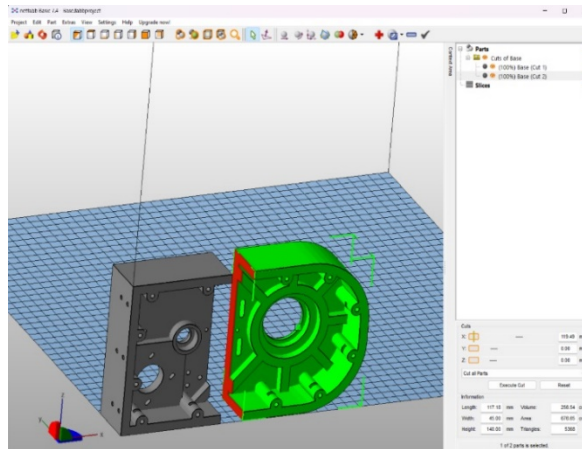


Figure 1. Ultimaker Cura Screenshot

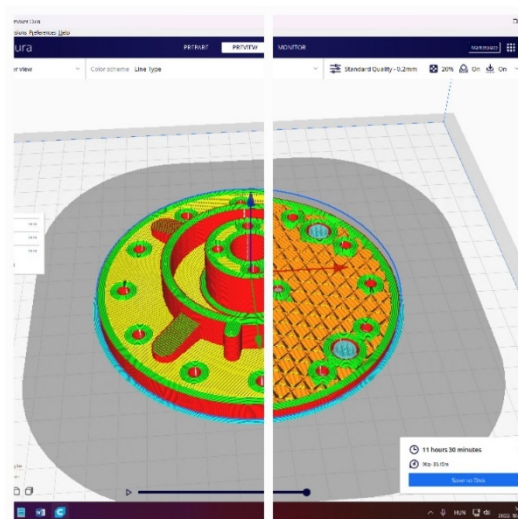


Figure 2. Netfabb Screenshot

Selection of electronic components

Stepper motors were used to move the robotic arm, as they do not require an external encoder, are easy to control, and can be used for positioning. The use of NEMA 17 bipolar stepper motors was decided due to their characteristics. These units are also widely used devices in 3D printers, small DIY CNC machines and drawing machines. This is also a great advantage because it can be obtained easily. These motors are compatible with the Arduino development platform, so they meet the requirement set in the objective. Motor controllers are essential to controlling the stepper motors precisely and properly. For the best results, three types of motor controllers were tested from existing solutions:

- DRV8825,
- TMC2208,
- A4988.

The stepper motor controller that was chosen is the A4988. These controllers operate between 5-35V with a maximum output current of 2A. The advantage is that only 2 pins are needed to control the motor. These two pins are responsible for the step and the direction of rotation (Dir). The remaining 14 pins are used to connect the 3-5.5V logic signal level, the 8-25V required to power the motor, the motor windings, and the MS1 MS2 MS3 pins to activate the microstepping. The controller requires a heat sink.

12V was used to power the motors, and the current limit was set to 0.48 A according to the following formula:

$$I_l = \frac{V_{ref}}{8 \cdot R_{CS}} \quad (1)$$

where:

I_l – the current limit, A

V_{ref} – the reference voltage between the potentiometer and the earth potential, V

R_{CS} – is the current sense resistance, Ω

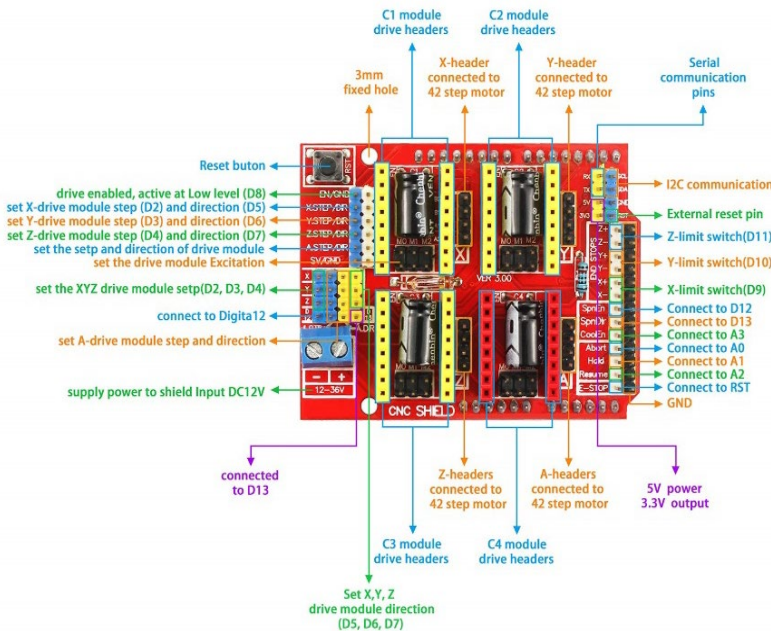


Figure 3. CNC Shield V3 Pinout

An Arduino UNO controller card was used to move the robot arm. During testing of the robot, this proved to be sufficient, but by including communication with Python code as part of the tasks to be performed, the workflow failed. For this reason, an Arduino Mega control card replaced the Arduino UNO. This device was able to handle the data communication with Python code without any issues. An Arduino Nano was used to move the motor of the conveyor belt. To handle one motor and one sensor, its computational capacity is more than adequate.

The A4988 controllers were used to control stepper motors require multiple connections from both the logic and power sides. There would not have been enough pins on an Arduino to control three motors. To overcome this problem, so-called expansion panels or shields, have been created for Arduino panels. To implement the task that was set, the CNC Shield V3.0 4-axis shield was chosen (Figure 3.). This expansion board is capable of controlling four A4988 or similar 16-pin motor controllers. The power supply for the motors must be connected to this panel; the allowed voltage is 12-36V. This shield is originally made for the Arduino UNO panel, but it can be connected to its bigger counterpart, the Arduino Mega. The expansion panel is also suitable for additional functions. Limit switches can be connected to separately defined pins, and on a CNC panel, a dedicated pin is included to start the milling tool. This leg was used to turn the electromagnet on and off.

Three of the four axes of the robot arm were used, so it needed three limit switches. For the first rotary axis marked X, the second rotary axis marked Y, and the linear axis marked Z. The roller switches that were used had 3 outputs; the user can choose to use them in NO (Normally Open) or NC (Normally Closed) mode. The NO binding mode was chosen, but the NC solution could have been used as well, since the switch state change carries the information.

To switch the electromagnet on and off, a relay of type FL-3FF-S-Z mounted on a printed circuit board was used. A red LED indicates the on-state of the magnet. On one side of the relay is the power supply for the logic unit and the corresponding input (5 V), and on the other side is the power circuit. As with the limit switch, there are three connections. The middle one is the common connection; the two end ones can be selected by the user (NO/NC).

The main criteria for the choice of the electromagnet could have been the load capacity, but the weight of the Styrofoam workpieces is negligible, so the one with the lowest power among the magnets available in practice was chosen. The magnet has a diameter of 20 mm, a power of 2.4 W, a supply voltage of 12 V, and a load capacity of 3 kg.

To use the magnet as an actuator, some way to attach the magnet to the end of the robot arm had to be found. The circular holes were placed on the flange at the end of the robot arm, which were designed to make the actuator easy to replace. It was relevant to design an electromagnet support bracket that could be fixed here. For the design, the version of the Solid Edge CAD software was used. The design was based on the principles used in precision mechanics, where the product is determined by dimensions, environmental, and manufacturing conditions and

not by the stresses. The support bracket was manufactured using 3D printing technology, and its model is shown in Figure 4.

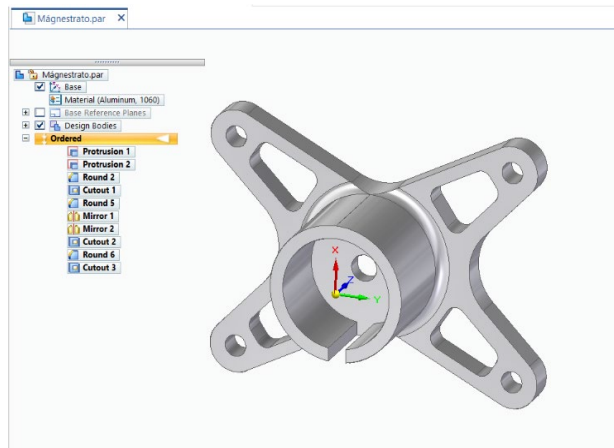


Figure 4. Mounting bracket for the magnet

The arrival of the workpiece on the conveyor at the pickup position must be detected, and the movement of the conveyor must be stopped while the workpiece is there. For this task, an infrared obstacle detection module was chosen. The sensor that was used is a type KY-032 (AD-032), which consists of two potentiometers, two feedback LEDs, one IR LED, and an HS0038B infrared sensor. The principle of operation is that the infrared light emitted by the IR LED is detected by the infrared sensor by reflection from the object (object reflection). Its advantage is that the viewing distance of the sensor can be adjusted and varied very precisely by means of two potentiometers. The Pled (Power LED) provides information on the power supply of the sensor, and the Sled (Sense LED) on the presence of an obstacle.

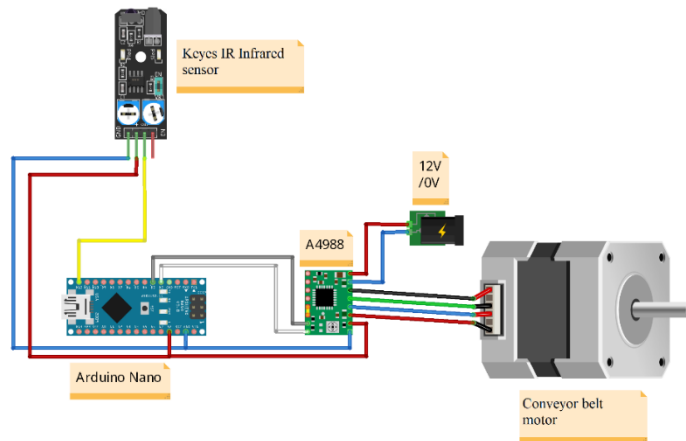


Figure 5. Wiring of the conveyor belt

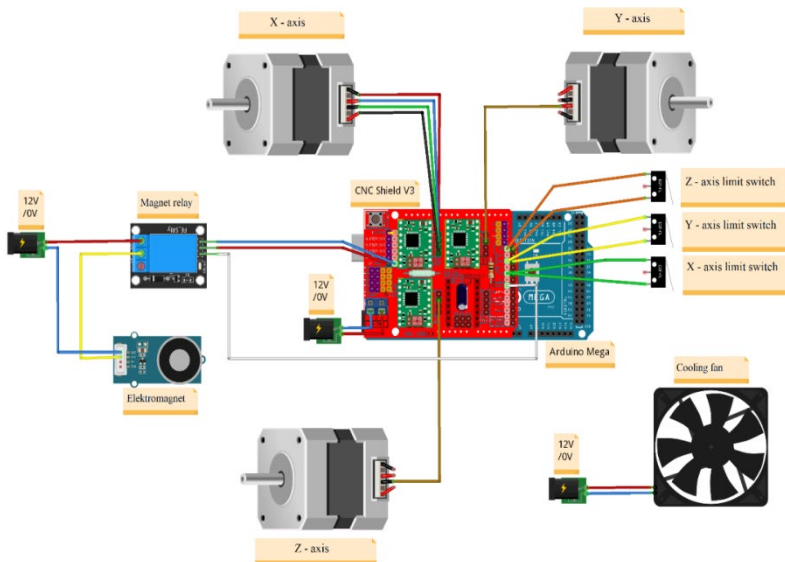


Figure 6. Wiring of the robotic arm

The operating software

The Arduino Mega controls the motors of the robot arm, switches the electromagnets, and manages the limit switches. For easy management of the stepper motors, a library called AccelStepper was used, and the MultiStepper library was also imported, which allows simultaneous movement of multiple stepper motors. After importing the libraries, the connection pins for the limit switches and the electromagnet were defined. The CNC Shield V3 pinout diagram

was used to help declare the motors. To define the motors, I needed the library name (AccelStepper), the motor name, and then, the motor control type, the step number, and the rotation direction pin. In this case, the motor control type is a motor control with two control pins. The value of this type is 1.

After defining the motors, a variable called `steppers` was created, which is used to move motors 1 and 2 simultaneously (MultiStepper steppers). Before the setup part of the program, the variables to be used were declared. Because the data sent to the serial port is also a String type, the `msg`, `x`, and `y` variables were created as String data types to save the data coming in on the serial port. However, the commands in the AccelStepper library require a number type, so it was necessary to create the variables `a` and `b` with the `int` (integer) data type. The `x` and `y` String values were converted into these variables.

In the setup part of the program, the way to control the limit switches and the magnet control pin were specified. The limit switch signal as input and the magnet control pin as output were defined. For the limit switches, the pull-up resistors were activated to avoid the signal floating. To ensure the safety of the robot, the maximum allowable speed and acceleration for each motor were set so that the motors could not exceed these values. Finally, the variable stepper motors `stepper1` and `stepper2` were added and the homing part of the program was called.

The homing part of the program runs once at the end of the setup part. Its task is to move each arm individually to the limit switch after the robot is switched on, and then zeros its position. After this operation, the positions can be interpreted. The end condition of the homing cycle is that the lever activates the limiting switch. When the switch is activated, the motor is set from 0 to the default position value. After the homing part of the program has run, the serial port displays "OK," which is required to communicate with the Python code.

In the main cycle, the motion program and communication for the selection run infinitely. At the beginning of the loop, a two-element `int` type array called `positions` was created, so they can be referred to as two positions at once to move two motors simultaneously.

An "if" statement was used to handle data coming from Python on a serial port. If the serial port is available, the data is written to the `msg` variable. Then the `substring` command was used to split the 8 characters into 4-4 characters, which are stored in the `x` and `y` variables. The character type was converted to an integer with the `toInt()` function. The integer values are stored in the variables `a` and `b`.

When the data is received, the robot arm approaches the workpiece, the electromagnet is switched on, and it then returns to its home position on the Z axis after a delay of 1 second. The two rotary axes then move the workpiece simultaneously to the position determined by color. On arrival, the magnet is released, the axes return to their home position, and the serial port displays "OK." To move the motor of the translation axis, the `stepper.runToNewPosition(0)` function was called, and for the rotation axes the `steppers.runSpeedToPosition()` was used. The disadvantage of the latter function is that acceleration is not included. The `digitalWrite()` function was used to turn the magnet on and off.

The Arduino Nano is responsible for moving the conveyor belt. The belt is driven by a NEMA 17 stepper motor with a GT2 ribbed belt. To move the motor in this case, the AccelStepper library was used. The motor was created as a stepper, moving it with a controller on pins D3 and D2 (AccelStepper stepper (1, 3, 2)). The IR obstacle detection sensor was defined on pin D12 and created a variable called sensorState. This variable will store the state of the sensor. In the setup part of the program, the sensorPin was interpreted as an input and specified the maximum speed and acceleration of the motor. In the main loop, the sensor state from sensorPin D12 was read, and then in an "if" branch, the sensor state was queried (HIGH/LOW). If the value is high, there is no workpiece in front of the sensor. In this case, the conveyor is moving, transporting the workpiece. Otherwise, if the sensor detects an obstacle, the motor speed decreases to zero and the robot stops until the robot arm removes the workpiece from in front of the sensor. (Madura et. al., 2000)

The Python code uses a camera to detect the color of the workpieces and outputs the position values corresponding to the colors to the Arduino. To detect the colors, the Open Computer Vision (OpenCV) library was used. The camera image was put into a variable called cap using the VideoCapture(0) function. Then the resolution of the camera image was set to 640x480 pixels, and a boolean logical variable called send with an initial value of True was defined, which will be used for communication.

In the main cycle, a frame in which the camera image can be displayed was captured. Following that, a new frame was created to convert the primary BGR (blue, green, and red) format color space to the secondary HSV (hue, saturation, value) color space. Each pixel in BGR or RGB format can be described by three values (Jähne, Hausßcker, 2000). The three values define the different colors by mixing the three colors to different degrees. In this case, using this format would make the task much more difficult. The problem with BGR color space is as follows: When a given color is detected, three values are returned: blue, green, and red. If the illumination of the body to be detected changes, the degree of mixing of the three colors will also change very significantly. So, in the case of BGR, three values would need to be tested within relatively large intervals to determine the color of an object. In contrast, for the HSV secondary color space, it is sufficient to examine the change in one value to identify simple colors, and the intervals are easily defined. The HSV color space was created to be similar to human color perception. To identify a color, it is sufficient to look at the first value, hue, which contains the colors red, orange, lemon, green, blue, and purple on a scale. After converting the color space, a pixel whose value could be examined was needed. The center of the frame was chosen as the pixel of interest, which is half the height and width of the frame. The H value of the center pixel was saved in the variable hue_value, and then the data for the different H values was specified in a branch. The flow chart shows which H values are associated with each color and position.

The result of the following position selection based on color was sent to the Arduino controlling the robot arm. A separate communication code with two functions, write and read, was used for this. The write function is responsible for sending the data to the serial port, and the read function is responsible for reading the data from the serial port. The first time the program is run, the send variable is set to True, so no data is output from the Python code to the serial port, but an "OK" is returned after the robot arm homing operation. The KomScript read function reads this and changes the value of the send variable to False. Subsequent program runs no longer ignore the KomScript.write(cmd) function in the "if" statement, and the desired position is communicated to the Arduino. The end of the Arduino's cycles is indicated by "OK." At the end of the program, there is a circle indicating the center of the frame and a command in the upper left corner to display the caption that changes according to the currently detected color. This is followed by a command to close the frame by pressing Esc key.

3. Results and discussion

The robotic arm and the actuator have successfully fulfilled the expected task, but there are a number of possible directions for improvement. If the actuator magnet was to be replaced by a gripper, it would have the possibility to grip non-magnetic workpieces, color detection could be more accurate if it was considered that not only a pixel but also the values of its surroundings were considered, and the use of forward or inverse kinematics for easier position capture would be a relevant direction of improvement.

Conclusions



Figure 7. The assembled robot

The project included the control design of a robotic arm that sorts objects by color. The SCARA robot arm from howtomechanics.com was used to construct the robot arm. After 3D printing the arm, some minor modifications had to be made for a more reliable operation, and accessories to perform the task that was defined were made (magnet holder bracket, conveyor belt, IR holder bracket). Next, the components for the actuator electronics of the robot arm and the conveyor belt were selected. NEMA 17 stepper motors were used to operate the robot arm as defined in the objective. To adapt to the drive, the A4988 motor controller was selected after exploring several options. For easier operation, a CNC Shield V3 was used, an expansion board for Arduino. After the motors and their controllers, other necessary elements were determined, such as limit switches, electromagnet, switch relay and IR sensor. After the robot arm was constructed mechanically, the electronics were assembled next, and lastly, the selection process was done with two separate switching circuits. One circuit belongs to the robot arm, the other to the workpiece conveyor. The two circuits operate from separate control cards, but their power supplies are common on the logic and power sides. After the hardware assembly of the robot arm (Figure 7.), the operating programs were coded. According to the objective - to move the robotic arm - the motors are powered by an Arduino Mega controller card, the conveyor belt by an Arduino Nano, and the color detection by Python code running on a computer.

References

- [1] P. Gergely (2009). *Felderítő Robotok*, Thesis
- [2] H. Madura, Z. Sikorski, H. Polakowski, M. Kastek (2000). Long-range passive IR sensor. <http://dx.doi.org/10.21611/qirt.2000.057>
- [3] B. Jähne, H. Haußecker (2000). *Computer Vision and Application*. USA: Academic Press ISBN 0-12-379777-2.
- [4] R. K. Miller (1989). *Industrial Robot Handbook*. New York: Springer Science+Business Media ISBN 978-1-4684-6608-9.

Implementation of an educational PID controller

János TÓTH

Department of Mechatronics, Institute of Technology, MATE, Gödöllő

Abstract

The process and goals of design and implementation of an educational proportional-integral-derivative (PID) controller will be discussed in this paper. The differences of an ideal and practical PID controller will be shown alongside the technical limitations that must be obeyed. The main purpose of the system is to show the students how a PID controller works and to provide an interactive example that can be used to demonstrate various aspects of the controlling process. The project is open hardware and open-source, meaning the schematic diagram and the source code of the firmware is freely available to anyone.

Keywords

Arduino, discrete control, anti-windup, interactive

1. Introduction

The control theory is an essential part of the mechanical/mechatronics engineering curriculum. The students are introduced to various controlling algorithms and methods, and the PID is the most widely used amongst these. A PID controllers are used in position control of pneumatic drives (Sárközi, Földi, 2017), temperature control of greenhouses (Bíró, Farkas, 1997), temperature control of solar thermal systems (Tóth et.al, 2019) and various other engineering tasks. The theoretical background of PID controllers is taught using computer simulation with the help of MATLAB+Simulink and FluidSim software packages, that gives the necessary background knowledge of the topic. Most of these simulations uses an ideal PID controller that is free of environmental and technical errors, therefore the implementation of a practical, real-world PID controller is beneficial. It shows the students how can an ideal system be implemented and what are the usual technical limitations of a control system. This control system can be used alongside the computer simulations creating a Hardware-in-the-Loop (HIL) model (Isermann et.al. 1998). Furthermore, a system like this could be used to demonstrate various manual PID tuning methods interactively like the Ziegler-Nichols method (Zigler, Nichols, 1942).

2. Matherial and methods

The controlled system, the controlling algorithms, hardware components and the firmware will be discussed in this chapter.

The controlled system

The controlled system is shown in Figure 1. It consists of a table tennis ball, a distance sensor, a servo motor, and a mechanism that constrains the movement of the ball and allows the motor to impact the position on the ball.

The table tennis ball was chosen because of its mass, cost, replaceability and beneficial optical properties.

The goal of the controller is to set the x position of the ball to a desired value via the φ rotation of the stepper motor, where the position can vary between 0 and L and the φ rotation must be between -90° and 90° .

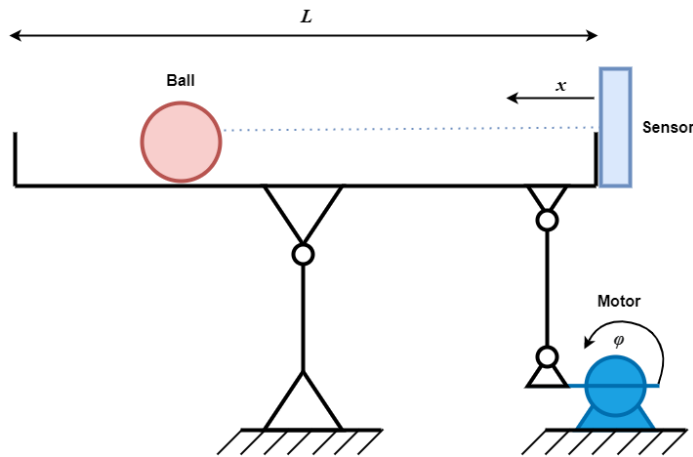


Figure 1. Schematic of the controlled system

The ideal PID controller

The PID controller is a closed loop controller, so the control signal depends on the output of the controlled system. This dependence is considered using the error:

$$e(t) = r(t) - y(t), \quad (1)$$

where e is the error, r is the setpoint and y the output of the controlled system, the process value. The error describes the difference between the desired and the actual value of the system. The governing equation of an ideal PID controller can be given using this relationship (Baltieri, Buckley, 2019):

$$u(t) = Pe(t) + I \int_0^t e(\tau) d\tau + D \frac{de}{dt} \quad (2)$$

where u is the output of the controller, P , I and D are the coefficients of the proportional, integral, and derivative members. The usual way to represent a PIC controller is through a block-diagram that can be seen in Figure 2.

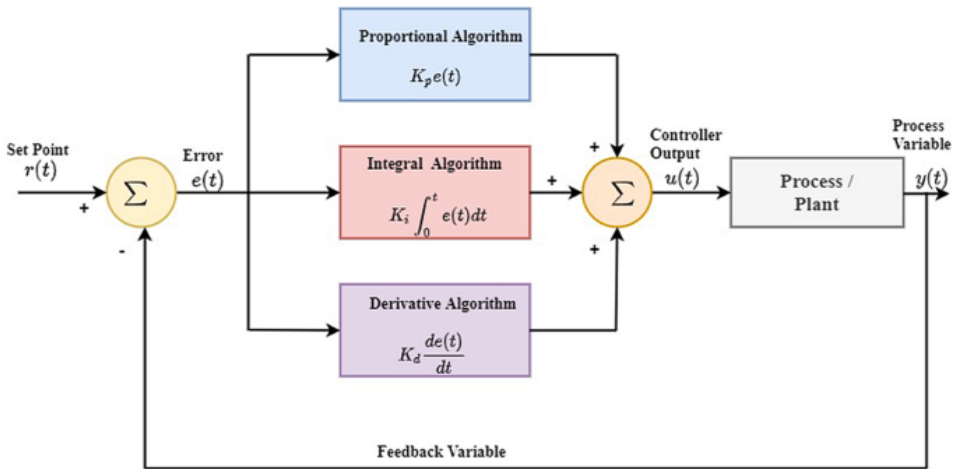


Figure 2. Block diagram of process control using PID (Borase et.al., 2021)

Some key observations can be made:

- u is a continuous function of t .
- The output of the controller is unbounded.
- If the steady state error is nonzero the contribution of the integrator will dominate the output.
- The noise of the error signal significantly effects the derivative member.

The set task is to show a real-world implementation of a PID controller using a digital control system. This means the controlling algorithm cannot be a continuous algorithm it must be a discrete one.

The unboundedness means that the magnitude of the output of the controller can be arbitrarily large, which is unachievable from a technical standpoint.

The nonzero steady state error causes the value of the integrator to grow infinitely, this phenomenon is called wind-up (Rundqwist, 1990). This can be avoided in case of a simulated system, but in the practice, it is nearly unavoidable, and it increases the response time of the whole system.

The derivative member is proportional to the change of the error, so if the “speed” of the error is high, e.g., the output of the system has noise (which is the typical case), it negatively effects the stability of the controller.

These are the key reasons this controller is called the “ideal PID controller” because it works in an ideal environment (no noise, no limitations, no uncontrolled errors), and therefore showing the implementation of a real/practical PID controller necessary.

The practical PID controller

To implement the PID controller, the above listed observations must be addressed.

Discretization

The discretized version of (2) can be written as:

$$u_i = P e_i + I \sum_{n=0}^i e_i \Delta t + D \frac{\Delta e_i}{\Delta t}, \quad (3)$$

where Δt is the fixed time step of the controlling algorithm, which is 50 ms.

Saturation

The saturation, or output limits can be applied to the output of the controller:

$$u_{is} = \max(u_{min}, \min(u_i, u_{max})), \quad (4)$$

where u_{min} and u_{max} are the technical limitations of the controlling system, in this case the minimum and maximum values of the allowed rotation of the motor: -90° and 90° .

Anti-windup #1

Two anti-windup methods were implemented, to show the different effects of them.

The first neglects the contribution of the integrator if the output signal would cause the controller to saturate. The algorithm can be described by the following pseudocode:

```
if control_signal > u_max or control_signal < u_min
    control_signal = control_signal - integrator_contribution
end
```

This method allows the integrator to keep its internal value in case of a steady state system.

Anti-windup #2

The integrator can be viewed as an accumulator, that accumulates the error. The second method uses this viewpoint to reset the internal value of the accumulator if the error of the control is below a predefined threshold:

```
if error < aw_treshold and error > -aw_treshold
    integrator = 0
end
```

This method allows the controller to be more responsive to the change of the setpoint.

Low-pass filter

The high frequency changes in the error signal would cause the derivative member of the controller to make the system unstable so a low-pass filter is required. The simplest low-pass filter one could implement is:

$$e = \frac{1}{N} \sum_{i=0}^N e_i, \quad (5)$$

where N is the number of samples, which is 50. The low-pass filter is implicit in this system because it is built-in to the data gathering process. The number of the samples was determined to keep the controller responsive.

Electronic components

The main goal of this project was to create an easy-to-understand, easy-to-build PID controlled system, the electrical design reflects that: it uses easy-to-obtain components that are compatible with the Arduino framework. This allows the students to modify or extend the system.

The main components used are:

- Arduino Mega,
- Sharp 2y0a21 Infrared Proximity Sensor,
- SG90 Servo Motor,
- 1602A LCD Display,
- Push buttons,
- Potentiometers.

The system is interactive, meaning the setpoint and the numerical values of the P, I and D can be changed in real-time using potentiometers. These values and the error of the control can be viewed with the help of an LCD screen.

Push buttons were used to add start/stop, display mode switching, and control mode switching functionalities.

The wiring diagram can be obtained from https://github.com/g0mb4/PID_demo/tree/main/schematics.

Firmware

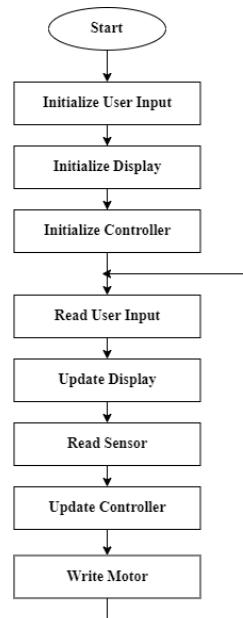


Figure 3. Block diagram of the firmware

The firmware of the Arduino Mega was created using the Arduino IDE. It is written in a procedural style to help the understanding of the source code. Figure 3 shows the block diagram of the firmware:

The source code of the project can be found at https://github.com/g0mb4/PID_demo.

3. Results and discussion

The resulting control system can fulfill its purpose. It is capable of the position of the table tennis ball in real-time. It can handle the change of the setpoint and display the parameters of the PID controller. It can show the effect of the different parameters of the PID control system, and it let the students to do various experiments with the controlling algorithms.

The push buttons and the potentiometers allow the switching of different operational modes that contains a manual mode, where the rotation of the stepper motor is directly mapped to the value of the potentiometer, so one can “compete” with the controlling algorithms.

The other operating modes includes the PID, PID with Anti-Windup #1 and PID with Anti-Windup #2.

Using the potentiometers, a P, I, D, PI, PD or even an ID controlling algorithm can be achieved.

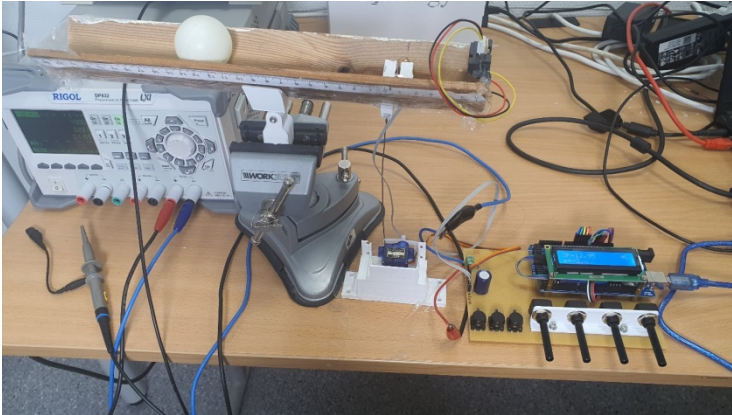


Figure 4. The realized control system

Conclusions

The aim of the project was to create a control system that uses the PID control algorithm and operates in a transparent way. The PID controller is a real-world implementation that show the differences between an ideal and a practical control system.

The hardware components were chosen to be easily obtainable, this way the replication or modification of the system is more achievable. The Arduino platform was used to aid this design decision. The source code of the firmware was written in a procedural C style that helps the reading and understanding the code without overwhelming the reader with the implementation details. This abstraction allows the reader to understand the underlying mechanisms and control-flow of the program and only seek the technical parts if desired.

The system is capable of the PID controlling process, it can demonstrate two anti-windup methods and it implements a low-pass filter to increase the stability of the control.

The control system was built and used as a teaching aid in various subjects and the general feed-back of the students were overwhelmingly positive due its interactive capability and easy-to-grasp concepts.

The interactive capability of the system means that the operating parameters can be changed during the operation and the result of these changes can be seen immediately. This fast feed-back helps the students to understand the meaning of these parameters.

The open-source nature of the project allows the students to extend this system, it can be used alongside a simulation as a HIL component. The Arduino platform makes it easy because no further hardware component is needed for this modification.

Acknowledgements

The author thanks his colleague, Viktor Erdélyi, the help he provided during the design and build of the electrical and mechanical aspects of the system.

References

- [1] M. Baltieri, C. L. Buckley (2019): PID Control as a Process of Active Inference with Linear Generative Models, *Entropy* 2019, Volume 21, Issue 3, p. 257; <https://doi.org/10.3390/e21030257>
- [2] A. Biró, I. Farkas I (1997): Theoretical and empirical approaches to the use of PID control for climate environment, *Hungarian Agricultural Engineering*, Vol. 10, pp. 64-67, ISSN: 0864-7410
- [3] R.P. Borase, D.K. Maghade, S.Y. Sondkar (2021): A review of PID control, tuning methods and applications. *Int. J. Dynam. Control* 9, pp. 818–827, <https://doi.org/10.1007/s40435-020-00665-4>
- [4] R. Isermann, J. Schaffnit, S. Sinsel (1998): Hardware-in-the-Loop Simulation for the Design and Testing of Engine-Control Systems, *IFAC Proceedings Volumes*, Volume 31, Issue 4, pp. 1-10, [https://doi.org/10.1016/S1474-6670\(17\)42125-2](https://doi.org/10.1016/S1474-6670(17)42125-2).
- [5] L. Rundqwist (1990): Anti-reset Windup for PID Controllers, *IFAC Proceedings Volumes*, Volume 23, Issue 8, Part 4, pp. 453-458, [https://doi.org/10.1016/S1474-6670\(17\)51865-0](https://doi.org/10.1016/S1474-6670(17)51865-0)
- [6] E. Sárközi, L. Földi (2017): Evaluation of PID-P cascade control algorithm used in positioned pneumatic drives, *Mechanical Engineering Letters*, Volume 15, pp 148-157, ISSN: 2060-3789
- [7] J. Tóth, V. Erdélyi, L. Jánosi, I. Farkas (2019): On-off and PID control of a small-scale solar system, *25th Workshop on Energy and Environment, Book of Abstracts*, p. 21, ISBN: 9789639483958
- [8] J.G. Ziegler, N. B. Nichols (1942): Optimum settings for automatic controllers, *Transactions of the ASME*, Vol. 64, pp. 759–768.

Variation of drone rotor operating parameters as a function of pitch angle

László BENSE, Attila LÁGYMÁNYOSI, István NAGY,
István OLDAL, István SZABÓ
Institute of Technology,
MATE, Gödöllő

Abstract

Drone rotors generally have a constant pitch angle. Thus, designers need to choose an angle that is optimal in several viewpoints and that gives good operating parameters in most situations during use. The primary consideration is the highest value of lift force with the lowest mechanical power, so it is expected that if only one consideration is chosen by the designer, this will be it. However, if other aspects are taken into account, e.g. noise emission, maximum lifting force, different results may be obtained. In the present work, we investigate the variation of lifting power and power demand of a commercially available rotor as a function of pitch angle. As a result, we obtain the relationships that are suitable to validate several optimization criteria for the selection of the rotor pitch angle.

Keywords

Drone, rotor, pitch angle, lifting force, optimization

1. Introduction

Drones have grown by leaps and bounds in the last decade. Not only for hobby purposes, but also as professional load-carrying devices. In parallel, the electronics, control, guidance and robotics used have evolved to meet specific needs (Bai et al. 2020) and (Darvishpoor et al. 2020) and (Karimi, Pourtakdoust, 2013). The development of drones for both civilian (industrial, agricultural, hobby) and military applications is continuing (Vergouw et al. 2016) and (Karaca et al. 2018) and (Shahmoradi et al. 2020). The size, load capacity and design of drones vary widely, from fixed-wing to multirotor solutions (Luca et al. 2017) and (Hassanalilian et al. 2019). The more frequent needs are covered by the market.

Noise emissions from the use of drones is a parameter that can cause problems in the application due to excessive noise exposure. There is research on noise emission that investigates noise generation theoretically (Chen et al. 2022) and experimentally (Ma et al. 2021).

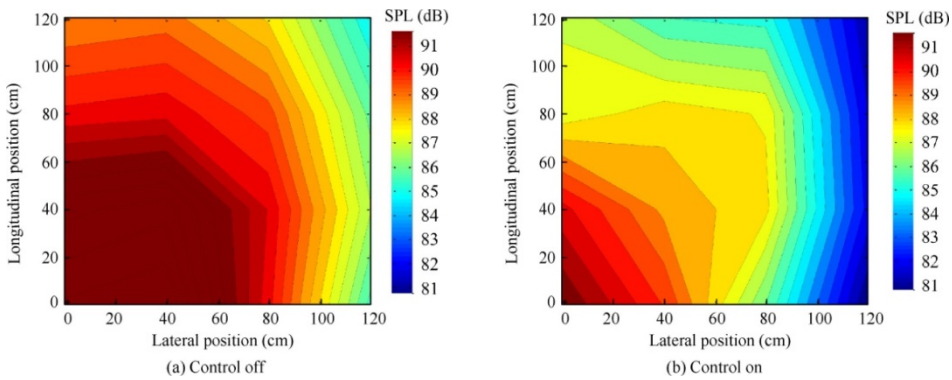


Figure 1. Noise SPL distribution variation beneath ECR advancing side during wind tunnel test (Ma et al. 2021)

Noise emissions increase with rotor speed. If you want to reduce noise for a given design, a good way to do this is to reduce the speed. The rotor pitch is a parameter that can be used to vary the lifting force, and can therefore be used to reduce noise. However, optimal noise and optimal energy consumption are not necessarily the same for the same pitch angle. If we want to find the optimum from several points of view, we need a precise knowledge of the relationship between lifting force and pitch angle. Determining this is our aim in the present work.

2. Materials and methods

Our studies use 3D modelling and numerical simulation. We investigate a real rotor, for which we first generate the 3D geometry by scanning. Then, the original pitch angle is modified on the geometric model and the lifting force and torque are determined. The power required is the product of the torque and the angular velocity. In our case, the angular velocity is held constant, so the change in torque is directly a change in power demand.

Geometric model

To perform the 3D scanning of the rotor, a Z Corporation ZScanner 700 3D laser scanner was used. We started the measurement by calibrating the instrument using our own dedicated calibration table. Then, the scanner was configured to suit the specific measurement environment. Parameters for background light intensity, laser intensity, shutter speed were set, which depend on the surface texture and colour of the piece to be measured, as well as on the ambient light intensity. The scanning was performed in two separate sessions on the measuring table with the measuring points glued on the rotor from above and from below. Afterwards, the two halves of the rotor were joined together in software and a solid body model was created. The 3D scanning was performed on one half of the symmetrical rotor,

from which the complete geometry was produced in post-processing. Based on the back measurements, an offset of 0.1 mm was measured between the scanned stock and the rotor.

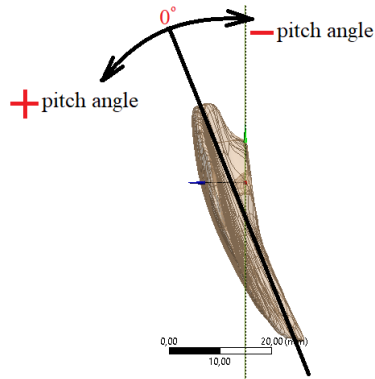


Figure 2. Scanned rotor geometry

The model in its factory condition is the starting point, in this position the angle of pitch is considered to be zero degrees. The other positions are considered to be positive or negative angles of attack in relation to this, as shown in Figure 2. The rotor angle is varied between -3 and +8 degrees during the tests. The scanned model is mirrored to produce the full rotor model, which is shown in Figure 3.

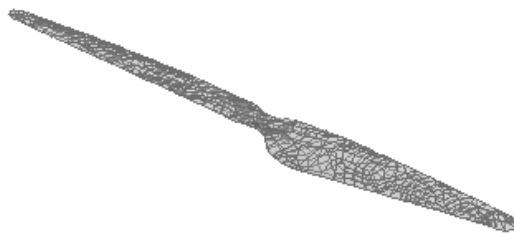


Figure 3. Complete rotor geometry

Finite element model

Given the 3D model, the lifting force data is generated using finite element method. As a geometric model, we have to model the flowing air instead of the scanned rotational geometry. Figure 4 shows the model used in the simulation. Therefore, it has been built a two mechanical model to cover the two situations the first situation the mechanism without the fins and the second model is the mechanism after adding the cooling fins.

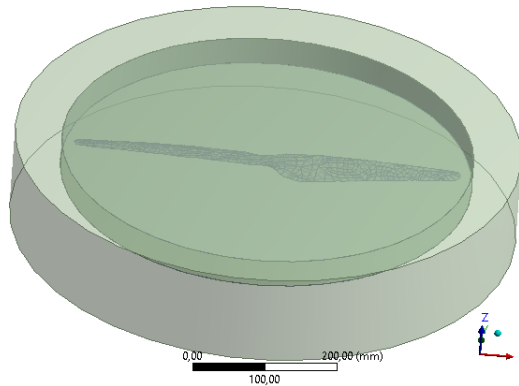


Figure 4. Flow geometric model

The complete model is made up of three parts: rotor, air around the rotor and external air. The flow model does not need a model of the rotor, but only its contour on the air model. The flow model thus consists of two parts, the rotor air and the external air model, which are in contact with each other. The rotating rotor is modelled using the inner geometry and the outer resting air boundary conditions are modelled using the outer geometry. In the second step of the modelling, the solid body model is required, at which point the air models will not be used.

The modelling consists of two linked parts. ANSYS CFX flow model is used to calculate the pressures acting on the rotor. The calculated results are imported into ANSYS Static Structural module and lifting force and torque are calculated. To model the flow, the first step is to construct the finite element mesh.

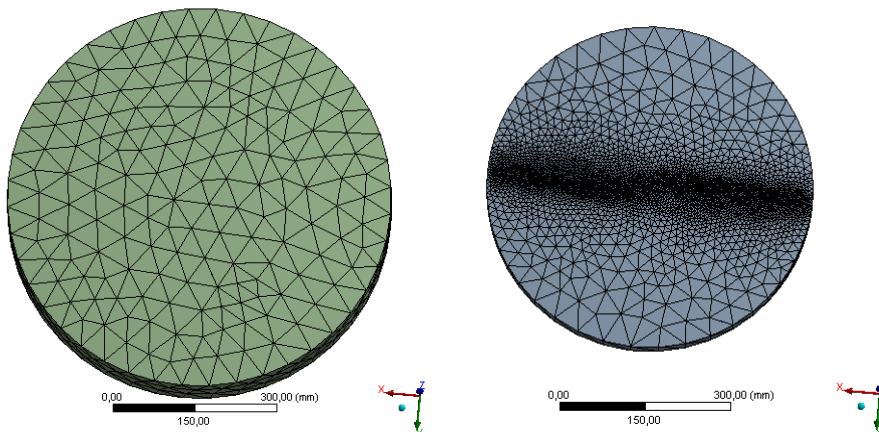


Figure 5. Mesh of outer domain (left) and internal domain (right)

The critical part from a flow point of view is the flow around the rotor surface, so around the edges we use tenths of a millimetre elements, while as you move away from the rotor we use increasingly larger elements. Our model thus consists of 2 156 479 elements (in case of zero pitch) the number of elements varies slightly for other angles.

The model is then used to define the boundary conditions. Normal state air properties are set, a "shear stress transport" turbulence model is used. The internal air is defined as a rotating domain with rotational speed of 6000 rpm. An open boundary with a pressure difference of 0Pa is specified on the outer surfaces of the outer air, a wall boundary is set on the rotor surfaces of the inner air. A fluid-fluid interface between the two air domain is defined, with a special "frozen rotor" option that can treat the model to model only the rotor geometry as a moving element.

3. Results and discussion

The microstructure of the syntactic foams

With flow modeling, we obtain the velocities and pressures in the entire model space. For further calculations, we need the pressures arising on the surface of the rotor. The pressure distribution on the rotor surface is not yet the data we want, because we want to determine the lifting force of the rotor. For this we need to do structural modelling. To model the solid body, we need the rotor from the original three-body geometry. We import the pressures obtained from the flow modeling into the rotor surface (Figure 6.).

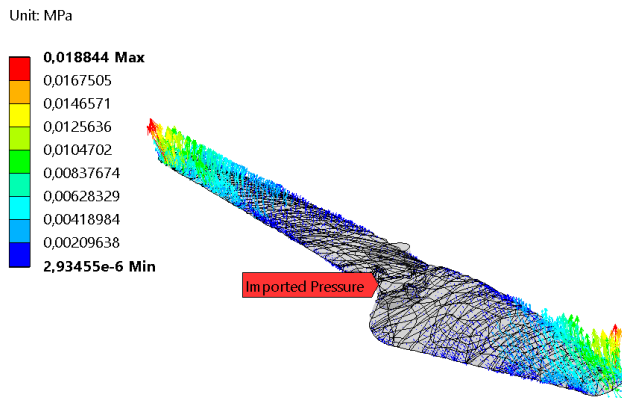


Figure 6. Imported pressures on rotor

The flow and strength modelling is carried out at all set angles of pitch. As a result of the tests, the rotor pitch-lift and pitch-torque curves are obtained. The calculated results are summarized in the following table.

Table 1. Calculated forces and torques

Pitch change (°)	Lifting force (N)	Torque (Nmm)	Pitch change (°)	Lifting force (N)	Torque (Nmm)
-3	30,968	1695,7	2	45,702	2508,3
-2	33,992	1834,2	3	48,768	2690,9
-1	36,676	1986,6	4	51,561	2898,8
-0,5	38,354	2059,1	5	54,785	3121,9
0	39,9	2135,8	6	57,774	3372,3
0,5	41,412	2231,9	7	60,73	3607,7
1	43,343	2332,1	8	63,687	3864,9

Clearly, increasing the angle of pitch causes an increase in lifting force and an increase in torque. The efficiency of the rotor is defined as the power demand for a given lifting force. Considering that the speed is constant in our tests, the efficiency can be derived directly from the ratio of force to torque. In our case, this ratio is the basis for the original angle of attack, and its ratio is examined for the other angles of attack. If we define the efficiency in this way, we obtain 100% for the original geometry, and it is visible how different angles of pitch compare to this (Figure 7.).

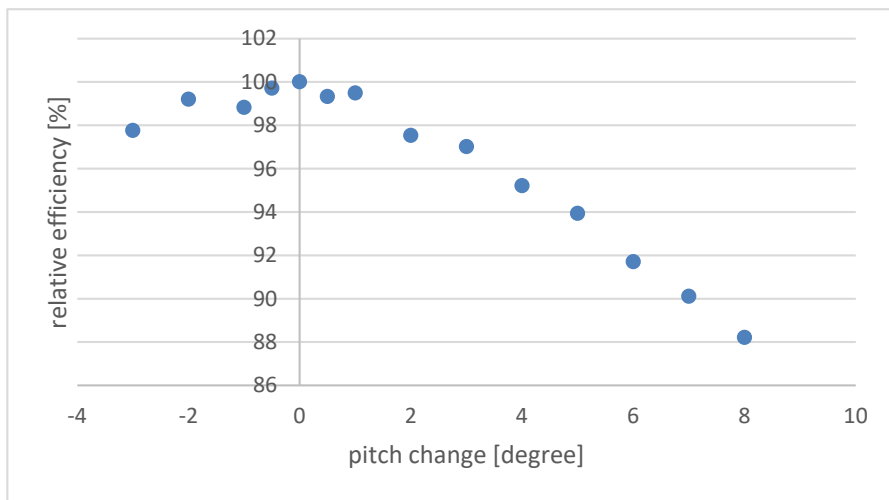


Figure 7. Relative efficiency of rotor with different pitch

The results show that the manufacturers have set the original angle of pitch where the rotor has the highest efficiency. However, this is only the optimum when approaching the problem from the energy side only. Based on this result, it

can be concluded that reducing the pitch angle is not worthwhile, because the efficiency and the lifting power are lower. However, if the angle of attack is increased, the lifting force is increased to a large extent with a small decrease in efficiency. For example, as shown in Figure 8, a 7 degree increase in pitch reduces the efficiency to 90%, but increases the lifting force by 52%. If noise reduction or higher lifting power with a small rotor size are among the objectives, the optimum may be shifted by a few degrees.

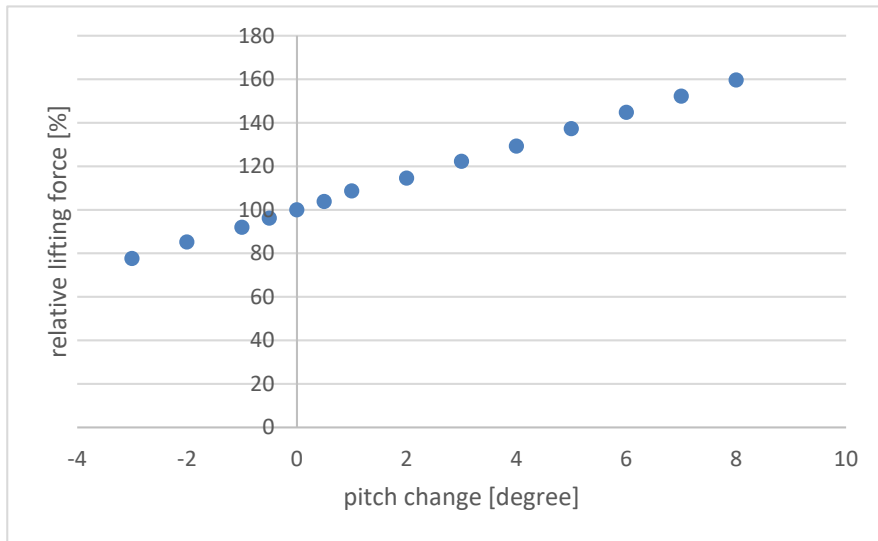


Figure 8. Relative lifting force of rotor with different pitch

In our work, we determined the effect of the angle of attack on the lifting force and torque for a given rotor. As a result, we obtain a database that allows for a multi-objective optimization. One possible aspect is the noise emission, in which case noise measurements have to be added to the data.

Conclusions

After reviewed the results we can summarize it by these conclusions:

- The rotor is factory set to the energy optimum, which is a bit noisy based on practical experience.
- With a small change of pitch angle, there is a few percent efficiency reduction on the energy side.
- Reducing the pitch angle is not worthwhile, because everything mutates deteriorates.

- Even a small increase in pitch angle causes a large increase in lifting power.
- From a noise point of view or from a lifting power increase point of view, the optimum angle of attack is expected to be larger than the optimum from an energy point of view only.

Acknowledgements

"This research was supported by the Ministry of Innovation and Technology within the framework of the Thematic Excellence Programme 2020, National Challenges Subprogramme (TKP2020-NKA-16)."

References

- [1] G. Bai, Y. Li, Y. Fang, Y.-A. Zhang, J.J.R.E. Tao, S. Safety, Network approach for resilience evaluation of a UAV swarm by considering communication limits, *Reliab. Eng. Syst. Saf.* 193 (2020) 106602.
- [2] Xi Chen, Kai Zhang, Qijun Zhao, Weiqi Wang, Numerical analysis of rotor aeroacoustic characteristics during collective pitch aperiodic variation in hover, *Aerospace Science and Technology*, Volume 124, (2022)
- [3] S. Darvishpoor, J. Roshanian, A. Raissi, M. Hassanalian, Configurations, flight mechanisms, and applications of unmanned aerial systems: a review, *Prog. Aero. Sci.* 121 (2020) 100694.
- [4] M. Hassanalian, R. Salazar, A. Abdelkefi, Conceptual design and optimization of a tilt-rotor micro air vehicle, *Chin. J. Aeronaut.* 32 (2) (2019) 369–381.
- [5] Y. Karaca, M. Cicek, O. Tatli, A. Sahin, S. Pasli, M.F. Beser, S. Turedi, The potential use of unmanned aircraft systems (drones) in mountain search and rescue operations, *Am. J. Emerg. Med.* 36 (4) (2018) 583–588.
- [6] J. Karimi, S.H. Pourtakdoust, Optimal maneuver-based motion planning over terrain and threats using a dynamic hybrid PSO algorithm, *Aerosp. Sci. Technol.* 26 (2013) 60–71
- [7] M. Di Luca, S. Mintchev, G. Heitz, F. Noca, D. Floreano, Bioinspired morphing wings for extended flight envelope and roll control of small drones, *Interface focus* 7 (1) (2017) 20160092.
- [8] Jinchao MA, Yang LU, Taoyong SU, Shujun GUAN, Experimental research of active vibration and noise control of electrically controlled rotor, *Chinese Journal of Aeronautics*, Volume 34, Issue 11, (2021) pp 106-118.
- [9] J. Shahmoradi, E. Talebi, P. Roghanchi, M. Hassanalian, A comprehensive review of applications of drone technology in the mining industry, *Drones* 4 (3) (2020) 34.

- [10] B. Vergouw, H. Nagel, G. Bondt, B. Custers, Drone technology: types, payloads, applications, frequency spectrum issues and future developments, in: *The Future of Drone Use*, TMC Asser Press, The Hague, 2016, pp. 21–45.

Comparing pressure hysteresis of DPF filters

Norbert BÍRÓ^{1,2}, Péter KISS³

¹IBIDEN Hungary Kft. Technical Center, Exhaust System Evaluation

² Doctoral School of Mechanical Engineering, MATE, Gödöllő

³Department of Vehicle Technology, Institute of Technology, MATE, Gödöllő

Abstract

Passenger and commercial transportation significantly contribute to hazardous air pollution. Exhaust gas aftertreatment technology advances closely to the emission regulations throughout the world. The upcoming legislation will be the Euro 7 in European Union, which requirements are not set yet, but in many aspect it is expected to be more severe, compared to the Euro 6. To satisfy the regulation, new DPF technology is required. This paper will present a pressure hysteresis comparison between the current and the proposed new generation DPF substrates. By this, a conclusion can be derived in order to determine the compliance of the upcoming Euro 7 legislation in terms of pressure hysteresis.

Keywords

DPF, Pressure Hysteresis, Euro 7, EATS

1. Introduction

The reduction of harmful emissions is a great interest in both scientific and public circles. The average of the Euro 27 countries attributes 14% of emissions to transport [Eurostat, 2022], therefore the further emission reduction possibilities have to be pursued. The total electricity produced in the world in 2016 was about 25 PWh, two-thirds of which came from fossil energy carriers. Numerous well to wheel analysis determines lower overall emission for the diesel powered ICE drivetrains than the BEVs [Gupta et al, 2017]. Keeping in mind these statements, the internal combustion engines still and going to play an important role in the commercial vehicles segment, economy wise and from environmental considerations as well. As mentioned the next regulation is expected to be more severe in terms of particle number emission and regeneration frequency as well. The latter can be reach with higher soot capacity of the DPF or more surface for catalytic coat. The higher soot capacity is unfavorable cost wise, therefore the only development path is to create more surface area for additional coating. This can be achieved by increasing the porosity of the DPF. Although it is important to not to weaken other properties of the filter, such as the pressure drop. As it is directly proportional with the engine efficiency and the emission formation, it must be

taken account as a key aspect with any development endeavor. In this paper, the pressure hysteresis of a conventional and the new HP (High Porosity) filter will be compared.

2. Experimental

Test layout

All the tests were carried out in engine dynamometer laboratory environment. The unit under test was a Euro VI-d compliant six cylinder, heavy-duty diesel engine. The engine conditions of the chosen test cycles have been de-normalized [Peng et al. 2017] to this specific test engine by the emission automation software called AVL PUMA Open™. The overview of the test layout can be seen below [Dieselnet, 2022]:

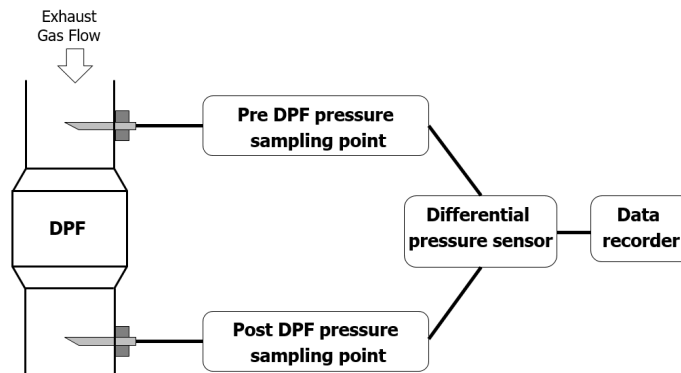


Figure 1. Schematic sketch of the test layout

The advantage of using an engine bench with fully equipped conditioner is ensuring the very same starting condition. Over numerous repetition, this gives a better comparison and much less uncertainty due to all the input variables are same.



Figure 2. Dynamometer mounted test engine connected to test cell conditioner system

Test schedule

Before every test, in order to ensure the repeatability, all DPF samples are dewaxed. The samples are heated to 700 °C for 10 hours [Bíró et al. 2020]. To compare soot accumulation status, after every test step, which has the probability to accumulate or burn off soot a weight measurement of the DPF is undertaken as it can be seen at Table 1.

Table 1. Test schedule

#	Test flow	Lead time[hr]
1	DPF preparation for test	10
2	DPF weight measurement	0.5
3	Precondition	1
4	DPF weight measurement	0.5
5	Full load curve	0.5
6	DPF weight measurement	0.5
7	Soot loading 1 g/l	2
8	DPF weight measurement	0.5
9	Full load curve	0.5
10	DPF weight measurement	0.5
11	Repeat #7 - #10, with 4 and 8 g/l	-

This measurement ought to be done at 150 °C, therefore the ambient room air humidity does not effect the results. The precondition creates a so-called soot cake, which allows particle filter to reach it's peak filtration efficiency [Bíró et al. 2022]]. During full load curve, the maximum engine speed is reached 8 rpm per second from idle speed, while the load is 100 %. By this a very extensive dataset can be drawn in terms of exhaust volume flow and pressure drop of the DPF. In order to simulate different saturation of the DPF filter, 3 levels of soot loading is included in the test schedule. 1 g/l corresponds to scarcely, 4 g/l to moderately and 8 g/l to heavily loaded sample.

3. Results and discussion*Evaluation of full load curves*

Two samples were tested, the original specification standard substrate and the improved high porosity new substrate. Four FLC were conducted with each

sample. With no prior soot accumulation, scarcely, moderately and heavily soot loaded condition, in order to simulate differentiated real life scenarios. These conditions are fixed, therefore each sample's corresponding tests are comparable to each other. During the experiments numerous output data has been created, most of it parameters like engine speed, engine torque, which helps to determine the comparability of the test. For evaluation, in this particular test 2 datasets are required, differential pressure over DPF (dP_DPF) and Exhaust gas volume flow (EVF). The pressure hysteresis can be extrapolated to the whole engine map, if the two parameters relation is defined by a descriptive equation. For this equation and to showcase the relation between dP_DPF and EVF, the values have been converted to a scatter point diagram. The equation calculated automatically by the diagram editor of the Microsoft Office excel.

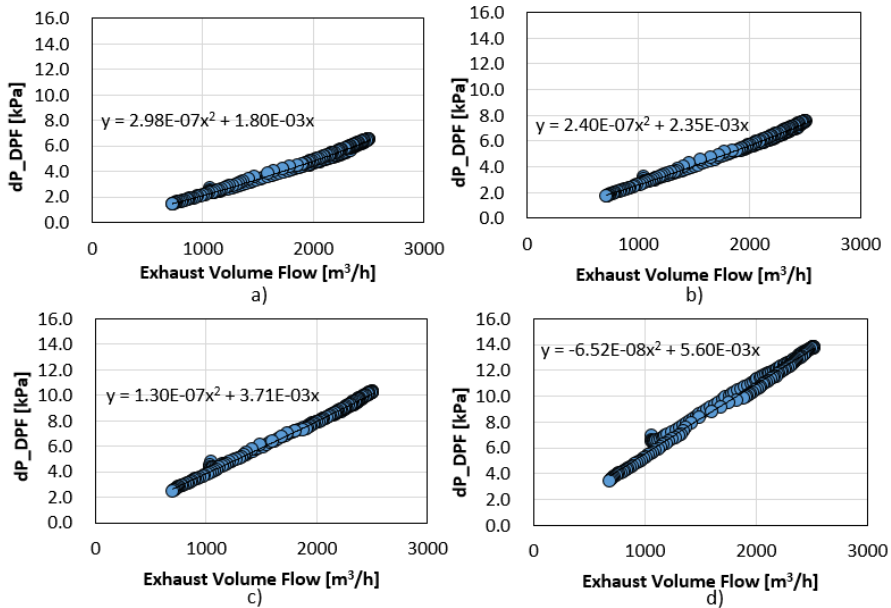


Figure 3. Pressure and flow data of Standard substrate FLC with 0 g/l (a), 1 g/l (b), 4 g/l (c), 8g/l (d) soot amount

As shown in Figure 3. The full load curves with different soot accumulation returns unique differential pressure and exhaust gas volume flow pairs. Therefore during the Standard substrate test procedure 4 descriptive equation could be drawn from the data. By examining the 4 diagrams it can be seen that the accumulated soot is directly proportional to the differential pressure.

Regarding the new substrate filter the diagrams and equations were created with the same methodical approach. Comparing the diagrams (Figure 4.) of standard and new (Figure 3.) substrates, it became apparent that at same soot accumulation levels the new substrates pressure drop is lower than the standard one.

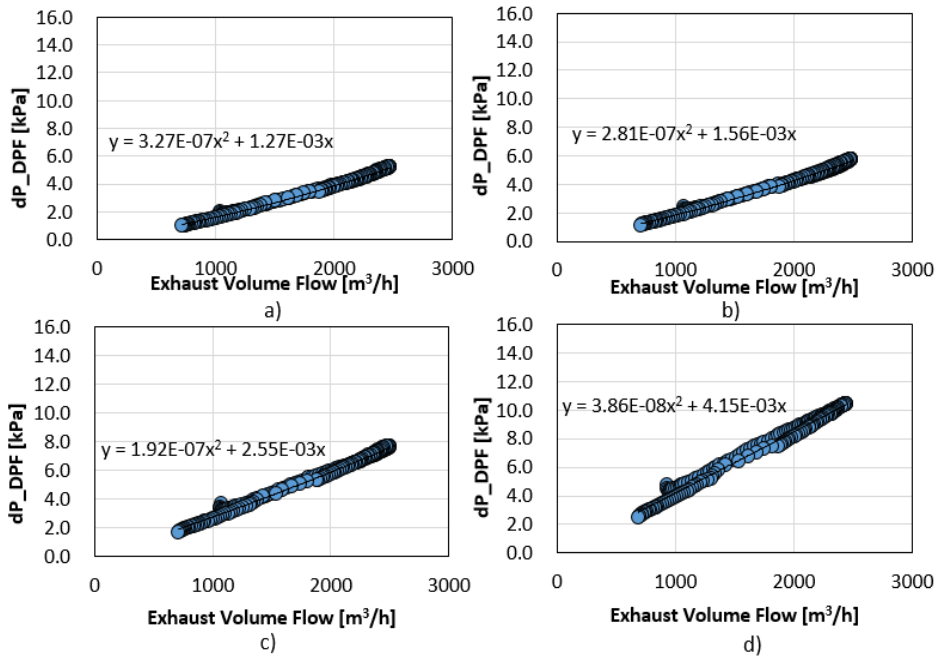


Figure 4. Pressure and flow data of New substrate FLC with 0 g/l (a), 1 g/l (b), 4 g/l (c), 8 g/l (d) soot amount

Comparing standard and new substrates

Applying the equations shown in Figure 3. and 4. the pressure drop became easily calculable at any given exhaust volume flow point. For comparability 1000, 1500, 2000 and 2500 m³/h has been chosen (Table 2.). Although for the final comparison only 2000 m³/h exhaust volume flow data has been used.

Table 2. Summarized test data of all FLC cycles of standard and new substrates

New substrate	dP_DPF [kPa]		Exhaust Volume Flow Rate [m ³ /h]			
			1000	1500	2000	2500
Soot mass [g/l]	0.0	1.6	2.6	3.8	5.2	
	0.8	1.8	3.0	4.2	5.7	
	4.0	2.7	4.3	5.9	7.6	
	8.0	4.2	6.3	8.5	10.6	
Standard substrate	dP_DPF [kPa]		Exhaust Volume Flow Rate [m ³ /h]			
			1000	1500	2000	2500
Soot mass [g/l]	0.0	2.1	3.4	4.8	6.4	
	1.0	2.6	4.1	5.7	7.4	
	3.9	3.8	5.9	7.9	10.1	
	7.9	5.5	8.3	10.9	13.6	

Figure 5. displaying the pressure drop values of each test at 2000 m³/h EVF in relation to the corresponding soot accumulation. As it could be seen from preliminary results, the new substrate pressure loss is much lower compared to the standard one.

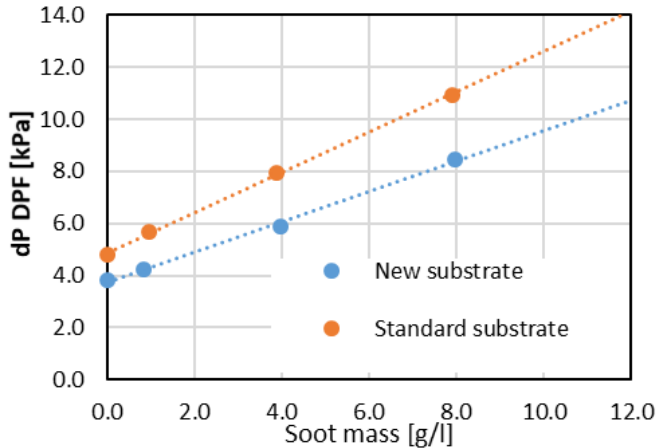


Figure 5. Comparing new and standard substrate on 2000 m³/h exhaust volume flow

Even if the heavily soot accumulated simulation is considered at 8 g/l soot amount, the new substrate is not exceeding the 10 kPa pressure drop limit. Which showing the new high porosity technology advances over standard. In order to satisfy the Euro 7 legislation [European Commission, 2022] limit, a catalytic coating layer is required, to decrease the NO₂ content and to enable higher efficiency passive regeneration. This coating technology already preexisted even at Euro 5 [EUR-Lex, 2007] legislation, however the applicable coating quantity is greatly influenced by the DPF filter's pressure drop. The new substrate's considerably lower pressure drop implies that probably with higher quantity of applied coating, the passive regeneration and the NO₂ reduction efficiency would be much higher. Although further experiments are required to prove these hypotheses.

References

- [1] Eurostat. Available online: https://ec.europa.eu/eurostat/statistics-explained/index.php?title=Quarterly_greenhouse_gas_emissions_in_the_EU (accessed on 21 December 2022).
- [2] Gupta, M., Rafat, Y., and Alam, M., "Well to Wheel Cum Tailpipe Emission Analysis: ICE vs xEV," SAE Technical Paper, 2017, 2017-26-0107, 2-4, <https://doi.org/10.4271/2017-26-0107>.

- [3] Peng, Y.; Nix, A.; Li, H.; Johnson, D.; Heltzel, R. Derivation of a Representative Engine Duty Cycle from On-Road Heavy-Duty Vehicle Driving Data. *J. Transp. Technol.* 2017, 7, 376–389. <https://doi.org/10.4236/jtts.2017.74025>.
- [4] Dieselnet. Available online: <https://dieselnet.com/standards/cycles/whsc.php> (accessed on 4 December 2022).
- [5] Bíró, N.; Pillinger, Gy.; Kiss, P.; Szöllösi, D.; Ohira, A. Experimental SCR system for engine dynamometer applications. *Hun. Agri. Eng.* 2020, 38, 56–62. <http://doi.org/10.17676/HAE.2020.38.56>.
- [6] Bíró, N.; Kiss, P. Euro VI-d Compliant Diesel Engine's Sub-23 nm Particle Emission. *Sensors* 2023, 23, 590. <https://doi.org/10.3390/s23020590>
- [7] European Commission. Available online: https://ec.europa.eu/commission/presscorner/detail/en/ip_22_6495 (accessed on 2 December 2022).
- [8] EUR-Lex. Available online: <https://eur-lex.europa.eu/legal-content/EN/TXT/?uri=celex%3A32007R0715> (accessed on 2 December 2022).

Approaches to the performance evaluation of semi-transparent photovoltaic modules

Nuha Desi ANGGRAENI¹, István SERES², István FARKAS³

¹Doctoral School of Mechanical Engineering, MATE, Gödöllő,

²Institute of Mathematics and Basic Science, MATE, Gödöllő,

³Institute of Technology, MATE, Gödöllő

Abstract

In this paper, several studies to evaluate the performance of semi-transparent photovoltaics are presented. A combination of actual measurement and simulation results is needed to evaluate semi-transparent photovoltaic performance. The performance can be calculated by assessing the optical, thermal, and electrical characteristics. These characteristics can be calculated by measuring the effect of outdoor temperatures, irradiance gain, generation level, and characteristics of the photovoltaic materials. The results show that the photovoltaic module produced relatively more electricity related to their lower temperature conditions, and the photovoltaic module with clear glass outperformed bronze glass.

Keywords

performance, photovoltaic, semi-transparent, energy, efficiency

1. Introduction

Photovoltaic systems use the photovoltaic effect to turn solar power into electric power directly. Photovoltaic modules are categorised as conventional or semi-transparent; most standard modules are constructed of monocrystalline and polycrystalline silicon. The layer structure of photovoltaics is shown in Fig. 1. Kafui studied the efficiency comparison of different photovoltaic modules, that is, amorphous silicon (a-Si), monocrystalline silicon (mc-Si), polycrystalline silicon (pc-Si), and transparent monocrystalline silicon module (PV-T, mc-Si) (Kafui et al., 2019). Kafui studied five different modules exposed to an average irradiation of 935 W.m^{-2} and an average ambient temperature of $35 \text{ }^\circ\text{C}$. Energy conversion rates of the modules were determined as 9.4 %, 4.4 %, 10.3 %, 8.3 %, and 10.4 % for the mc-Si glass module, a-Si glass module, pc-Si module (two types) and PV-T, respectively.

Manufacturers provide photovoltaic module characteristics after being tested indoors under standard test conditions, and these parameters may alter due to the weather. As a result, determining the amount of energy produced by photovoltaic modules under real-world operating conditions is essential so that the use of photovoltaic modules following natural conditions and climate change is urgently

needed (climate characteristics of selected locations shown in Table 2). Determining the amount of energy produced by photovoltaics will help us to enhance our knowledge about photovoltaics in every climate condition.

Table 1. Technical specification of photovoltaic modules under STC

Parameters	a-Si (Glass) (DUNA SOLAR)	mc-Si (Glass) (SOLARWATT)	pc-Si (60Wp) (SOLAREX SM2160)	pc-Si (105Wp) (RWE SCHOTT SOLAR)	PV-T glazed (mc-Si) (SOLIMPEKS)
V_{oc} (V)	62.5	23.4	21.3	29.5	43.39
I_{sc} (A)	1.15	9.02	3.8	4.92	5.55
V_{mpp} (V)	44.0	19.2	17.1	23.5	35.15
I_{mpp} (A)	0.90	8.71	3.5	4.47	5.12
P_{mpp} (Wp)	40	165	60	105	180
Module area (m ²)	0.791	1.62	0.564	0.826	1.427
Temp. coeff. of power	-0.47	-0.40%/°C	-0.47	-0.47%/°C	-0.45%/°C
Temp. coeff. of V_{oc}	-0.36%/	-0.32%/°C	-0.073%/°C	-0.38%/°C	-0.34%/°C
Temp. coeff. of I_{sc}	+0.04%/	0.05%/°C	0.003%/°C	+0.10%/°C	+0.06%/°C
Efficiency	5%	10.3%	10.6%	12.7%	12.6%

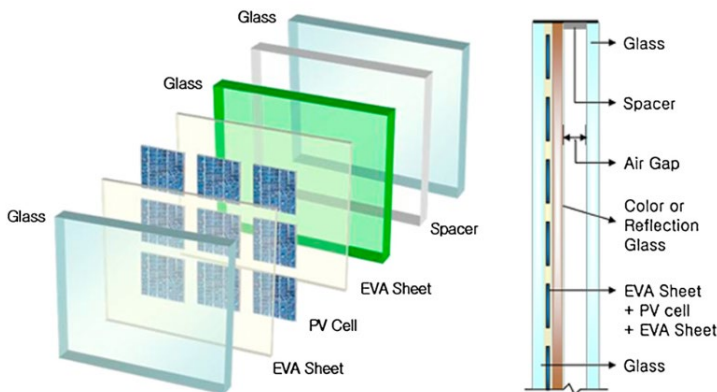


Figure 12. Photovoltaic layer's structure (Park et al., 2010)

Table 2. Selected global locations and their climate characteristics (Setyantho et al., 2021)

Location	Latitude	Longitude	Climate	HDD (18.3 °C)	CDD (10 °C)	Monthly Solar Radiation (Average ± std.Deviation)	Electricity Price (US\$/kWh)
Chengdu, China (baseline)	30.667	104.017	Cfa	1422	2662	3588.33 ± 1186.61	0.081
Abu Dhabi, UAE	24.417	54.65	BWh	24	6254	6037.67 ± 1352.89	0.02
Buenos Aires, Argentina	34.817	58.517	Csa	1189	2524	4520.33 ± 1797.41	0.095
Beijing, China	39.783	116.467	Dwa	2906	2199	4142.08 ± 1448.84	0.081
Cairo, Egypt	30.1167	31.383	BSh	390	4276	5253.08 ± 1777.24	0.036
Incheon, South Korea	37.467	126.55	Dfa	1920	2782	3222.5 ± 1028.68	0.11
Reykjavik, Iceland	64.117	21.883	Dfc	4917	65	2129.5 ± 1775.32	0.16
Singapore	1.367	103.967	Af	0	6374	4582.5 ± 261.03	0.182
Wellington, New Zealand	41.283	174.767	Csb	1849	1218	3968.58 ± 1987.73	0.23

Apart from conventional photovoltaic made of monocrystalline and polycrystalline silicon, semi-transparent photovoltaic modules are built of organic solar cells, dye-sensitised solar cells, or other developing technologies. Semi-transparent photovoltaic can deliver high power consumption energy, maximise irradiation capture, and reduce the adverse effect on the photovoltaic cells because it can influence electrical generation (Park et al., 2010) and recycle the heat produced in the age of solar power for another purpose (Khalifeeh et al., 2021). The solar cell layer characteristics influence optical qualities and thermal behaviour (Chae et al., 2014). Another research also studied the one-dimensional transient heat-transfer model, the semi-transparent photovoltaic module heat gain model. It evaluated the heat gain at semi-transparent photovoltaic modules for building-integration applications (Fung and Yang, 2008). These are critical if a sustainable energy future is to be realised.

Table 3. Performance ratio of the photovoltaic module (Kafui et al., 2019)

Performance ratio (PR) of modules	mc-Si (glass) (165 Wp) [%]	a-Si (glass) (40 Wp) [%]	pc-Si (105 Wp) [%]	Pc-Si (60 Wp) [%]	PV-T glazed mc-Si (180 Wp) [%]
Minimum	83	79	74	69	75
Maximum	91	89	81	77	83
Average	85.2	82.6	76.7	71.8	77.5

According to Fung and Yang, solar energy efficiency and photovoltaic module thickness have little effect on total heat gain, and solar heat gain is the dominant component of total heat gain. Performance metrics like efficiency, performance ratio and electrical performance (shown in Table 3 and Fig. 2) are provided, and specific parameters like yield and performance ratio efficiency were calculated. The performance ratio is the ratio of the efficiency of the photovoltaic module/system during operation to its efficiency at STC, given by Eq. (1).

$$PR = \frac{\eta_{Syst}}{\eta_{STC}}. \tag{1}$$

Specific module yield (Y_a) is defined as the ratio of the module’s energy output over a given period to its rated power, described by Eq. (2):

$$Y_a = \frac{E_{DC}}{P_{PV_{rated}}}. \tag{2}$$

Solar module temperature (T_c) can be calculated using the following model, described by Eq. (3):

$$T_c = T_a + \frac{G}{G_{STC}} \times (T_{NOCT} - 20), \quad (3)$$

where:

T_a : ambient temperature (°C)

T_{NOCT} : nominal operating cell temperature is given by the manufacturer (°C)

G : measured solar irradiation over the surface of the module ($W.m^{-2}$)

The model calculates solar module output power while taking into account the linear dependence of output power on solar irradiance and cell temperature, explained in Eq. (4):

$$P_m = P_{mSTC} \times \frac{G}{G_{STC}} \times (1 - \gamma(T_c - 25)), \quad (4)$$

where:

P_m : calculated output power (W)

P_{mSTC} : maximum rated capacity at STC given by the manufacturer (W)

G : solar irradiation intensity on the plane of the module ($W.m^{-2}$)

G_{STC} : solar radiation intensity of $1000 W.m^{-2}$

γ : maximum power correction factor for temperature

T_c : module temperature (°C)

The module's instantaneous efficiency is defined as follows:

$$\eta = \frac{P}{(G \times A)}, \quad (5)$$

where:

η : efficiency (%)

P : measured power output (W)

G : measured solar irradiation ($W.m^{-2}$)

A : surface area of the module (m^2)

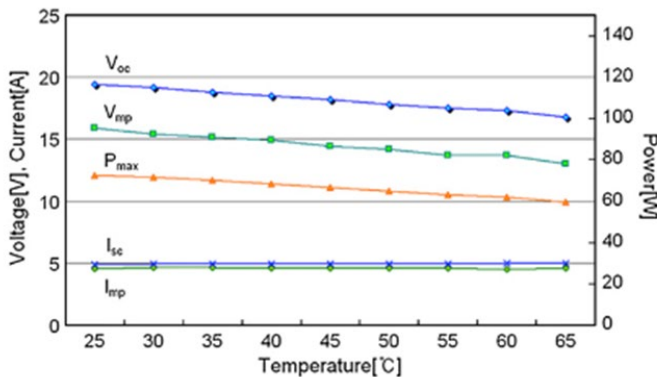


Figure 13. Electrical performance of photovoltaic module with temperature variation (Park et al., 2010)

The semi-permanent photovoltaic study includes developing solar technology to deliver higher PCEs and maximise irradiation capture. Reduce the negative effect of heat on photovoltaic cells and recycle the heat produced throughout solar power generation for other purposes. These are essential if a sustainable energy future is to be realised. Semi-transparent photovoltaic has the potential for energy conservation, lowering the amount used to provide “thermal comfort” as well as delivering aesthetically stunning lighting effects (Khalifeeh et al., 2021). The recent study aims to analyse the performance and efficiency of semi-transparent photovoltaics and provide knowledge for future research related to their applications.

2. Applied methodologies

Theoretically, energy conversion from semi-transparent photovoltaic modules is not as high as from the standard modules. The module parameters that play a critical role in determining the current-voltage (I-V) and power-voltage (P-V) characteristics of a solar PV module are considered in this study, including the conversion efficiency, irradiance level, transmissivity, and back layer temperature (Talib et al., 2019). A thorough understanding of photovoltaic characteristics helps in utilising photovoltaic as a renewable energy source.

When semi-transparent PV modules with multiple layers of materials are installed as a facade element, they are exposed to the ever-changing environment, including fluctuating air temperature and incident solar radiation levels. As a result, unsteady state heat transfer analysis accounts for transient conditions and non-homogeneous elements (Fung and Yang, 2008). The optical characteristic is identified as the transmittance of visible light (VLT). The thermal transmittance coefficient (U-value) and solar heat gain coefficient represent thermal characteristics (SHGC). Finally, electrical characteristics are quantified using maximum power output and STPV efficiency (Setyantho et al., 2021). Selected commercial semi-transparent photovoltaic characteristics are shown in Table 4.

Table 4. Semi-transparent photovoltaic characteristics (Setyantho et al., 2021)

Module	Thermo-Optical Parameters			Electrical Parameters		Price
	VLT (%)	U-Value (W/m ² K)	SHGC	Max. Power (Wp/m ²)	η_{STPV} (%)	
Baseline	20.0	2.281	0.380	86.06	10	-
Module A	9.17	5.076	0.289	77.42	8.02	US\$ 591
Module B	5.19	4.795	0.413	55.94	5.90	US\$ 232.245
Module C	6.91	1.674	0.154	47.92	4.75	US\$ 1215.74
Module D	28.4	5.7	0.41	28	2.8	US\$ 107.51
Module E	26.7	5.2	0.37	28	2.8	US\$ 121.75
Module F	10.8	5.7	0.29	40	2.8	US\$ 105.63
Module G	80	5.5	0.8	39.56	11	US\$ 59.40

For this study, semi-transparent modules are installed in front of the Aula building of the Hungarian University of Agrivulture and Life Sciences, Gödöllő, Hungary, at latitude 47.5946° N, 19.3619° E. The systems consist of 2x10 pieces 165 Wp Solarwatt Vision with 3,3 kWp, and the modules are shown in Fig. 3 (Kafui et al., 2019). Semi-transparent photovoltaic modules were oriented south with an inclination that matched the site and angled to a fixed physical support outside the Aula building.

Table 5. Geographical site parameters for Gödöllő (PVsyst 6.7.0) (Kafui et al., 2019)

Period	Global Irradiation (kWh.m ⁻² .d ⁻¹)	Diffuse Irradiation (kWh.m ⁻² .d ⁻¹)	Temperature (°C)	Wind speed (m.s ⁻¹)
January	0.97	0.69	-0.6	2.78
February	1.84	0.94	1.1	3.00
March	2.93	1.46	5.6	3.41
April	4.41	2.08	11.7	3.10
May	5.53	2.44	17.1	2.99
June	5.99	3.00	19.6	2.89
July	5.98	2.85	21.8	3.09
August	5.00	2.22	21.3	2.71
September	3.60	1.81	15.6	2.61
October	2.31	1.19	11.3	2.6
November	1.14	0.73	5.7	3.00
December	0.81	0.51	0.2	2.49
Year Average	3.38	1.66	10.9	2.49



Figure 14. Installed system (Kafui et al., 2019)

The following factors should be considered while analysing photovoltaic performance, such as module yield; solar module temperature; solar module output power; solar module efficiency; and performance ratio. Module output power, voltage, and current were measured automatically using Geräte

Naturwissenschaft Technik equipment. The solar radiation was measured with an LSL 200 solarimeter at the modules' level and inclination. Semi-transparent photovoltaic module temperature, photovoltaic ambient temperature, and the real ambient temperature were measured with HT-9815 Xintest Pt-100 sensors.

In previous research, the geographical site parameter for the research study shows in Table 5.

3. Results and discussion

A combination of actual measurement and simulation results is needed to evaluate semi-transparent photovoltaic performance. Three essential things that can be used to assess the performance of semi-transparent photovoltaic are:

1. Optical characteristic is defined as the visible light transmittance (VLT).
2. Thermal characteristics are represented by the thermal transmission coefficient (U-value) and solar heat gain coefficient (SHGC).
3. Electrical characteristics are quantified through the maximum power output and efficiency of STPV (η_{STPV}).

Several variables, such as outdoor temperature, irradiance gain, generation level, and material characteristics, are used to assess the performance of semi-transparent photovoltaics. Different materials can improve the absorbing selectivity, improving the optical aspects of semi-transparent photovoltaics. The surface temperature of the photovoltaic cell supporting glass is regarded as the temperature of the photovoltaic module, which affects the photovoltaic module's electrical generation. As the air gap did not come into direct contact with the photovoltaic cell, the glass layer that kept the air gap from the photovoltaic laminate appeared to be influenced more by the indoor environment, such as the indoor air temperature and heating or cooling sources.

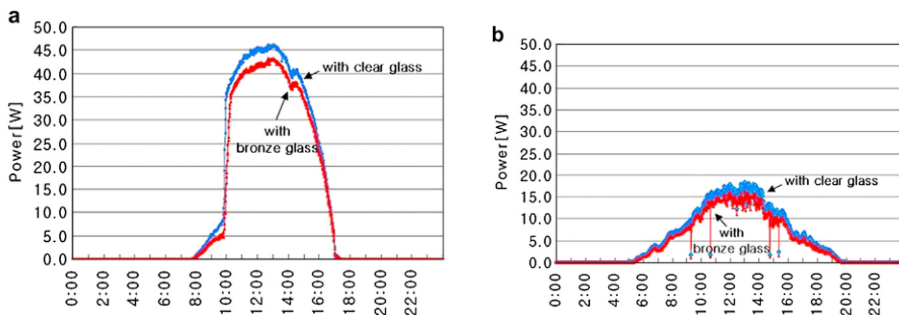


Figure 15. Comparison of the output of photovoltaic modules: a) Summer (June 2008), b) winter (December 2007)

The fact suggests that the electrical performance of photovoltaic modules is affected by temperature variations, as a photovoltaic module with a higher

temperature can reduce its electricity generation. The photovoltaic module with bronze glass appeared to have a higher temperature than the module with clear glass in their study. Consequently, the photovoltaic module with clear glass outperformed bronze glass (Park et al., 2010). Measured results of the comparison output of the photovoltaic can be seen in Fig. 4 for both summer and winter seasons.

Conclusions

The current study found that three characteristics are needed to assess the performance of semi-transparent photovoltaics. Those characteristics are the optical, thermal, and electrical characteristics. Different conditions must be applied to the systems to evaluate the semi-transparent photovoltaic performance. These methods will give a better understanding of the performance of semi-transparent photovoltaics. A combination of actual measurement and simulation results is needed to evaluate the semi-transparent photovoltaic performance.

Acknowledgements

This research was supported by the Stipendium Hungaricum Programme and the Mechanical Engineering Doctoral School, Hungarian University of Agriculture and Life Sciences, Gödöllő, Hungary.

References

- [1] Chae, Y.T., Kim, J., Park, H., and Shin, B. (2014). Building energy performance evaluation of building integrated photovoltaic (BIPV) window with semi-transparent solar cells. *Applied Energy*, 129, 217–227. <https://doi.org/10.1016/j.apenergy.2014.04.106>
- [2] Fung, T.Y.Y., and Yang, H. (2008). Study on thermal performance of semi-transparent building-integrated photovoltaic glazings. *Energy and Buildings*, 40, 341–350. <https://doi.org/10.1016/j.enbuild.2007.03.002>
- [3] Kafui, A.D., Seres, I., and Farkas, I. (2019). Efficiency comparison of different photovoltaic modules. *Acta Technologica Agriculturae*, 22(1), 5–11. <https://doi.org/10.2478/ata-2019-0002>
- [4] Khalifeh, R., Alrashidi, H., Sellami, N., Mallick, T., and Issa, W. (2021). State-of-the-art review on the energy performance of semi-transparent building integrated photovoltaic across a range of different climatic and environmental conditions. *Energies*, 14(12). <https://doi.org/10.3390/en14123412>
- [5] Kocsány, I., Seres, I., and Farkas, I. (2018). Performance analysis of semi-transparent module pv system. 17th International Workshop for Young Scientists (BioPhys Spring 2018), Nitra, Slovakia, 33.

- [6] Li, Y., He, C., Zuo, L., Zhao, F., Zhan, L., Li, X., Xia, R., Yip, H.L., Li, C.Z., Liu, X., and Chen, H. (2021). High-performance semi-transparent organic photovoltaic devices via improving absorbing selectivity. *Advanced Energy Materials*, 11, 1–10. <https://doi.org/10.1002/aenm.202003408>
- [7] Mun, S.H., Kang, J., Kwak, Y., Jeong, Y.S., Lee, S.M., and Huh, J.H. (2020). Limitations of energypplus in analysing energy performance of semi-transparent photovoltaic modules. *Case Studies in Thermal Engineering*, 22, 1–9. <https://doi.org/10.1016/j.csite.2020.100765>
- [8] Park, K.E., Kang, G.H., Kim, H.I., Yu, G.J., and Kim, J.T. (2010). Analysis of thermal and electrical performance of semi-transparent photovoltaic (PV) module. *Energy*, 35, 2681–2687. <https://doi.org/10.1016/j.energy.2009.07.019>
- [9] Setyantho, G.R., Park, H., and Chang, S. (2021). Multi-criteria performance assessment for semi-transparent photovoltaic windows in different climate contexts. *Sustainability (Switzerland)*, 13(4), 1–22. <https://doi.org/10.3390/su13042198>
- [10] Talib, U., Abdulrahman, S.A., Kumar, V., and Bazghaleh, M. (2019). Performance evaluation of multi-layer semi-transparent photovoltaic system; Vol. 268, Issue 1). Institute of Physics Publishing. <https://doi.org/10.1088/1755-1315/268/1/012149>
- [11] Wu, J., Zhang, L., Liu, Z., Luo, Y., Wu, Z., and Wang, P. (2020). Experimental and theoretical study on the performance of semi-transparent photovoltaic glazing façade under shaded conditions. *Energy*, 207, 1–12. <https://doi.org/10.1016/j.energy.2020.118314>